

INTERFACIAL WAVES IN SHEAR FLOWS

by

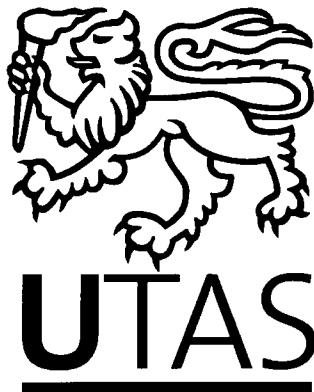
Michael J. Chen, BSc (Hons.)

Submitted in fulfilment of the requirements
for the degree of Doctor of Philosophy

School of Mathematics and Physics

University of Tasmania

August 2010



Acknowledgements

I would like to thank my supervisor Larry Forbes. His enthusiasm, wit, patience and generosity of intellect have been invaluable over the last few years.

Thanks also to Pete While, Stuart Morgan, Paul Burch, Tony Fitzpatrick, Claire Hotan, Michael Brideson and Simon Wotherspoon who each helped in their own special way.

Thanks to Caroline for the chocolate milk and for putting up with my whingeing.

Finally, I'd like to thank Mum, Dad and Holly for their love and support.

I declare that this thesis contains no material which has been accepted for a degree or diploma by the University or any other institution, except by way of background information and duly acknowledged in the thesis, and to the best of my knowledge and belief no material previously published or written by another person except where due acknowledgement is made in the text of the thesis, nor does the thesis contain any material that infringes copyright.

Signed: 

Michael J. Chen

Date: 21/9/10

This thesis may be made available for loan and limited copying in accordance with the Copyright Act 1968.

Signed: 

Michael J. Chen

Date: 21/9/10

The following people contributed to the publication of work undertaken as part of this thesis.

Steady periodic waves in a three-layer fluid with shear in the middle layer [14]

Michael Chen (75%), Larry Forbes (25%)

A study of nonlinear waves and resonance in intrusion flows [13]

Michael Chen (80%), Larry Forbes (20%)

Accurate methods for computing inviscid and viscous Kelvin-Helmholtz instability (submitted) [15]

Michael Chen (80%), Larry Forbes (20%)

Waves in two-layer shear flow for viscous and inviscid fluids (submitted) [16]

Michael Chen (80%), Larry Forbes (20%)

We the undersigned agree with the above stated proportion of work undertaken for each of the above published (or submitted) peer-reviewed manuscripts contributing to this thesis.

Signed:

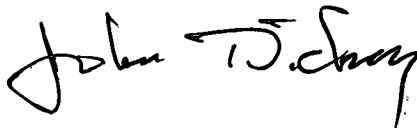


Larry Forbes
Supervisor
School of Mathematics and Physics
University of Tasmania

Date:

21 Sept 2010.

Signed:



John Dickey
Head of School
School of Mathematics and Physics
University of Tasmania

Date:

21/09/10

Abstract

Interfacial waves in fluid flow have widespread applications in meteorology, oceanography and astrophysics. Several flows are considered in detail in this thesis. A key feature of these flows is that they each possess shear and they are each studied with a view to determining the behaviour of interfacial waves in the flow.

The thesis begins with an investigation of a steady three-layer intrusion flow, in which all three layers are in motion with different speeds relative to the observer. Shear is present in the middle layer, and the lowest fluid may even move oppositely to the upper two (so giving an exchange flow). Two thin interfaces are present, above and below the moving middle layer. A linearized analysis is presented for small wave amplitudes. Non-linear periodic solutions are then obtained using a spectral method based on Fourier series, and these reveal a range of non-linear phenomena, including limiting waves, multiple solutions and resonances.

The techniques used to study the intrusion flow are then extended to allow for time-dependent behaviour, and applied to the Kelvin-Helmholtz instability for an inviscid fluid. The viscous version of this problem is also considered. Here, two bounded fluid layers flow parallel to each other with the interface between them growing in an unstable fashion when subjected to a small perturbation. In this problem, and the related problem of the vortex sheet, there are several phenomena associated with the evolution of the interface, notably the formation of a finite time curvature singularity for inviscid fluids and the 'roll-up' of the interface when viscosity is included. Two contrasting computational schemes will be presented. A spectral method is used to follow the evolution of the interface in the inviscid version of the problem. This allows the interface shape to be computed up to the time that

a curvature singularity forms, with several computational difficulties overcome to reach that point. A weakly compressible viscous version of the problem is studied using finite difference techniques and a vorticity-streamfunction formulation. The two versions have comparable, but not identical, initial conditions and so the results exhibit some differences in timing. By including a small amount of viscosity the interface may be followed to the point that it rolls up into a classic 'cat's-eye' shape. Particular attention is given to computing a consistent initial condition and solving the continuity equation both accurately and efficiently.

The final problem studied in this thesis is a two-layer shear flow for inviscid and viscous fluids. Here, the layers flow between two horizontal walls and are buoyantly stable. Each layer contains a finite amount of shear and the horizontal velocity is specified such that it is continuous when unperturbed. The interface between the two layers is given a small sinusoidal perturbation and the subsequent response of the system is studied. Different solution techniques are employed for the inviscid and viscous flow. These both rely on linearizing the governing equations for each of these flows. As a consequence, several restrictions are placed on how the viscous flow may evolve; namely that as it develops the flow will not differ too greatly from the unperturbed flow. These assumptions are justified since standing wave behaviour is expected in the inviscid case. Solutions are presented for a variety of different values of the shear parameters and the way these parameter choices affect the interaction between vorticity and density in the viscous case is investigated in detail.

Contents

| | |
|---|----|
| Acknowledgements | 0 |
| Abstract | 3 |
| List of Figures | 7 |
| Chapter 1. Introduction | 12 |
| Chapter 2. Steady periodic waves in a 3-layer fluid with shear in the middle layer | 17 |
| 2.1. Introduction | 17 |
| 2.2. Model and governing equations | 21 |
| 2.3. Linearized solution | 24 |
| 2.4. Nonlinear solutions and numerical scheme | 29 |
| 2.5. Results | 36 |
| 2.6. Discussion and conclusion | 61 |
| Chapter 3. Accurate methods for computing inviscid and viscous Kelvin- Helmholtz instability | 64 |
| 3.1. Introduction | 64 |
| 3.2. Inviscid model: governing equations | 67 |
| 3.3. Linearized solution for inviscid problem | 69 |
| 3.4. Non-linear solution for inviscid problem | 71 |
| 3.5. Weakly compressible viscous model: Governing Equations | 79 |
| 3.6. Choice of initial conditions for viscous model | 85 |
| 3.7. Results | 89 |

| | |
|--|-----|
| 3.8. Conclusion | 101 |
| Chapter 4. Waves in two-layer shear flow for viscous and inviscid fluids | 104 |
| 4.1. Introduction | 104 |
| 4.2. Model formulation | 106 |
| 4.3. Linearized solution to the inviscid problem | 112 |
| 4.4. First-order perturbation series approach to the viscous problem | 115 |
| 4.5. Results | 129 |
| 4.6. Conclusion | 149 |
| Chapter 5. Conclusion | 151 |
| Bibliography | 153 |

List of Figures

- 2.1 Diagram of the flow configuration showing the three fluid layers moving horizontally with waves propagating at the two interfaces $y = \eta_U$ and $y = \eta_L$ above and below the middle layer. 22
- 2.2 Plot of the linearized dispersion relation (3.12) to give the relationship between wavenumber k and lower layer Froude number F_3 . The parameter values chosen are upper layer Froude number $F_1 = 0.1$ and density ratios $D_1 = 0.99$ and $D_3 = 1/0.99$. 28
- 2.3 Plot of the ratio of wavenumbers when two linearized solutions exist for the same lower layer Froude number. The lower-layer Froude number F_3 is shown on the horizontal axis. Linear resonance is possible where the ratio is integer valued. 30
- 2.4 Dependence of Froude number F_3 on lower wave amplitude \mathcal{A}_L for $k = 0.5$, the in-phase case with positive Froude number. 37
- 2.5 Four interfacial profiles for the in-phase case with positive Froude number at $k = 0.5$. The solutions shown are $(\mathcal{A}_L, F_3) = (0.601, 0.167)$ (solid lines), $(\mathcal{A}_L, F_3) = (0.0844, 0.232)$ (dashed lines), $(\mathcal{A}_L, F_3) = (0.133, 0.243)$ (dotted lines) and $(\mathcal{A}_L, F_3) = (0.0547, 0.371)$ (dash-dot lines). 39
- 2.6 Dependence of Froude number F_3 on upper wave amplitude \mathcal{A}_U for $k = 0.5$, the out-of-phase case with positive Froude number. 40
- 2.7 Two interfacial profiles for the 1:9 resonance at equal lower layer Froude number. The short wavelength mode is out of phase with the primary wave for the solution at $(\mathcal{A}_U, F_3) = (0.0644, 0.310)$ (solid lines) and in phase for the solution at $(\mathcal{A}_U, F_3) = (0.0629, 0.310)$ (dashed lines) 42

- 2.8 Two interfacial profiles for the 1:10 resonance at equal lower layer Froude number. The short wavelength mode is in phase with the primary wave for the solution at $(\mathcal{A}_U, F_3) = (0.104, 0.303)$ (solid lines) and out of phase for the solution at $(\mathcal{A}_U, F_3) = (0.0946, 0.303)$ (dashed lines); 43
- 2.9 Two interfacial profiles for the 1:11 resonance at equal Froude number. The short wavelength mode is out of phase with the primary wave for the solution at $(\mathcal{A}_U, F_3) = (0.109, 0.300)$ (solid lines) and in phase for the solution at $(\mathcal{A}_U, F_3) = (0.0980, 0.300)$ (dashed lines). 44
- 2.10 Dependence of Froude number F_3 on lower wave amplitude \mathcal{A}_L for $k = 0.5$, the in-phase case with negative Froude number. 46
- 2.11 Four interfacial profiles for $\mathcal{A}_L = 0.32$ with a 1:4 resonance in phase with the primary solution mode. The profiles shown are for $(\mathcal{A}_L, F_3) = (0.32, -0.1614)$ (solid lines), $(\mathcal{A}_L, F_3) = (0.32, -0.1620)$ (dashed lines), $(\mathcal{A}_L, F_3) = (0.32, -0.1612)$ (dash-dot lines) and $(\mathcal{A}_L, F_3) = (0.32, -0.1662)$ (dotted lines). 47
- 2.12 Three interfacial profiles for $\mathcal{A}_L = 0.32$ with a 1:4 resonance out of phase with the primary solution mode. The profiles shown are for $(\mathcal{A}_L, F_3) = (0.32, -0.1643)$ (solid lines), $(\mathcal{A}_L, F_3) = (0.32, -0.1617)$ (dashed lines) and $(\mathcal{A}_L, F_3) = (0.32, -0.1613)$ (dash-dot lines). 48
- 2.13 Dependence of lower layer Froude number F_3 on upper wave amplitude \mathcal{A}_U for the slower speed case at $k = 1$. 50
- 2.14 Three interfacial profiles for the slower speed case. The red lines are wave profiles for $\mathcal{A}_U \approx 0.21$. The solid and dashed black lines display a 1:5 resonance and are for $\mathcal{A}_U \approx 0.025$. 52
- 2.15 Dependence of lower layer Froude number F_3 on upper wave amplitude \mathcal{A}_U for the faster speed case at $k = 1$. 53
- 2.16 Four interfacial profiles for the faster speed case. The black, red and green wave profiles are all at an upper wave amplitude of $\mathcal{A}_U \approx 0.17$.

- The blue profiles are for $\mathcal{A}_U \approx 0.25$. All except the black profiles display a 1:2 resonance. 54
- 2.17 Dependence of Froude number F_3 on lower wave amplitude \mathcal{A}_L for $k = 2.5$, the in-phase case with positive Froude number. 55
- 2.18 Four interfacial profiles for the in-phase case with positive Froude number at $k = 2.5$. The profiles shown are for $(\mathcal{A}_L, F_3) = (0.188, 0.0421)$ (solid lines), $(\mathcal{A}_L, F_3) = (0.0693, 0.0594)$ (dashed lines), $(\mathcal{A}_L, F_3) = (0.0986, 0.0447)$ (dash-dot lines) and $(\mathcal{A}_L, F_3) = (0.138, 0.0537)$ (dotted lines). 56
- 2.19 Dependence of Froude number F_3 on upper wave amplitude \mathcal{A}_U for $k = 2.5$, both the out-of-phase cases with negative Froude number. 58
- 2.20 Four interfacial profiles originating from out-of-phase case with large negative Froude number at $k = 2.5$. The profiles shown are for $(\mathcal{A}_U, F_3) = (0.1388, -0.2591)$ (solid lines), $(\mathcal{A}_U, F_3) = (0.05704, -0.07093)$ (dashed lines), $(\mathcal{A}_U, F_3) = (0.6327, -0.1267)$ (dash-dot lines) and $(\mathcal{A}_U, F_3) = (0.1053, -0.2154)$ (dotted lines). 59
- 2.21 Four interfacial profiles originating from out-of-phase case with small negative Froude number at $k = 2.5$. The profiles shown are for $(\mathcal{A}_U, F_3) = (0.01951, -0.06958)$ (solid lines), $(\mathcal{A}_U, F_3) = (0.03172, -0.1562)$ (dashed lines), $(\mathcal{A}_U, F_3) = (0.01534, -0.07866)$ (dash-dot lines) and $(\mathcal{A}_U, F_3) = (0.07627, -0.1875)$ (dotted lines). 60
- 3.1 A schematic diagram showing the flow configuration for the inviscid model. 68
- 3.2 Evolution of the inviscid interface for the case $F_1 = 0.2$, $F_2 = -0.2$, for both the linearized (dashed line) and fully nonlinear (solid line) solutions. Figures 3.2(a)–(f) show the times $t = 0, 2, 4, 6, 7$ and 7.35 , respectively. 93
- 3.3 Comparison of interface shape and curvature for the case $F_1 = 0.2$, $F_2 = -0.2$, where interfacial profiles are shown at selected times in figures

- 3.3(a)-(e) and the corresponding curvature for the same times is shown in figures 3.3(f)-(j). The heavy crosses in figures 3.3(a)-(e) mark the maximum and minimum points of curvature. 94
- 3.4 Evolution of vorticity in the viscous model for the case $F_1 = 0.2$, $F_2 = -0.2$ displayed as contours for a selection of times between $t = 0$ and $t = 30$. 97
- 3.5 Evolution of density in the viscous model for the case $F_1 = 0.2$, $F_2 = -0.2$ displayed as contours for a selection of times between $t = 0$ and $t = 30$. 98
- 3.6 Contour plots of streamfunction and velocity components from the viscous model at $t = 15$ for the case $F_1 = 0.2$, $F_2 = -0.2$. 99
- 3.7 Plots of a single contour of density $D = 0.995$ for the case $F_1 = 0.2$, $F_2 = -0.2$. The four time steps shown here, $t = 13, 14, 15$ and 16 , illustrate the crucial point at which the density profile overturns. 100
- 3.8 Evolution of vorticity in the viscous model for the case $F_1 = 0.1$, $F_2 = 0.5$ displayed as contours for a selection of times between $t = 0$ and $t = 30$. Here the solution evolves in a similar fashion to the case shown in figure 3.3, with the added feature that this wave travels to the right as it grows. 102
- 4.1 Schematic of the two-layer shear flow. The heavy dashed line shows the continuous horizontal velocity profile $U_{01}(y)$ used in the viscous formulation, while the thin solid line is the horizontal profile for the inviscid case. 107
- 4.2 Contours of vorticity against a single contour of density (with the value $\rho = 0.995$ and shown as a dashed line) at the times $t = 0, 15.8, 23.2, 34.4, 40.5, 45.8, 49.9$ and 52.56 for the case of $\gamma_1 = \gamma_2 = 0$. 133
- 4.3 a) The amplitude of the interfacial wave \mathcal{A}_ρ and b) the minimum and maximum of vorticity are shown for the case of $\gamma_1 = \gamma_2 = 0$ between $t = 0$ and 2000 . 135

- 4.4 The values of vorticity for the case of $\gamma_1 = \gamma_2 = 0$ at the points $(x, y) = (0, 0)$ (solid line) and $(x, y) = (0, \pi)$ (dashed line). 137
- 4.5 Contours of vorticity against a single contour of density at $t = 1972.3$ for the case of $\gamma_1 = \gamma_2 = 0$. 138
- 4.6 Contours of vorticity against a single contour of density at $t = 50.2$ for the case of $\gamma_1 = \gamma_2 = 0.1$. 139
- 4.7 Figures 7(a) and (b) show the wave amplitude and the minimum/maximum of vorticity for $\gamma_1 = \gamma_2 = 0.1$. Similarly, figures 7(c) and (d) show these variables for the case of $\gamma_1 = \gamma_2 = 0.2$ and figures 7(e) and (f) are for $\gamma_1 = \gamma_2 = 0.3$. 141
- 4.8 Figures 8(a) and (b) show the wave amplitude and the minimum/maximum of vorticity for $\gamma_1 = \gamma_2 = 0.4$. Similarly, figures 8(c) and (d) show these variables for the case of $\gamma_1 = \gamma_2 = 0.5$ and figures 8(e) and (f) are for $\gamma_1 = \gamma_2 = 0.6$. 142
- 4.9 For the case of $\gamma_1 = \gamma_2 = 20$ between $t = 0$ and 25 a) the amplitude of the interfacial wave \mathcal{A}_p and b) the minimum and maximum of vorticity. 144
- 4.10 Figures 10(a) and (b) show the wave amplitude and the minimum/maximum of vorticity for $\gamma_1 = 0$ and $\gamma_2 = 0.01$. Similarly, figures 10(c) and (d) show these variables for the case of $\gamma_1 = 0$ and $\gamma_2 = 0.02$. 145
- 4.11 Figures 11(a) and (b) show the wave amplitude and the minimum/maximum of vorticity for $\gamma_1 = 0$ and $\gamma_2 = 0.03$. Similarly, figures 11(c) and (d) show these variables for the case of $\gamma_1 = 0$ and $\gamma_2 = 0.04$. and figures 11(e) and (f) are for $\gamma_1 = 0$ and $\gamma_2 = 0.05$. 147
- 4.12 Comparison of wave amplitude for the case of $\gamma_1 = \gamma_2 = 0$ computed with the perturbation series technique (solid line) and a finite difference method (dashed line). 148

CHAPTER 1

Introduction

The study of interfacial waves in fluid flow is a rich field of research with numerous applications in areas such as meteorology, oceanography and astrophysics. Historically much of the interest in this type of problem has focussed on the question of the stability of an interface under certain flow conditions. Numerous examples are presented in Lamb [35] and Taylor [56] where the stability of interfacial flows in inviscid fluid under the effects of shear and buoyancy, among others, are investigated in detail. Of particular interest in the context of this thesis are the discussions of Kelvin-Helmholtz instability, see Lamb [35, article 232], and the stability of a shear layer, which is discussed at some length by Taylor [56].

This discussion of stability has been extended to take into account more complex effects. Numerous flows that include the effects of viscosity and compressibility are outlined, for instance, in Drazin and Reid [19]. In particular, compressible flow is important in modelling geophysical situations, such as the dynamics of oceans and atmospheres. Hydromagnetic effects are similarly important in modelling astrophysical situations and in the study of plasmas, and a number of flows of this types are detailed by Chandrasekhar [11]. The focus of this thesis, however, will be on the effect of shear on the behaviour of fluid interfaces. Various effects such as viscosity will also feature in some of the flows under consideration, but they are typically included so that interesting properties of shear flows may be highlighted.

A common linearization approach to this type of problem in inviscid fluids is to study the behaviour of the flow when it is subject to a small interfacial perturbation. In such an approach the governing equations and interfacial boundary conditions are approximated with a linearized system under the assumption that

the solution only differs from a steady base flow by a small (first-order) perturbation. By further assuming that the solution components have wave-like forms it is possible to obtain a dispersion relation between the various parameters of the flow. For steady problems (where it has been assumed that the behaviour is not time dependent) this is effectively a criterion on the parameters that must be satisfied for a steady wave to exist. A simple case may indicate the wavelength of a wave permitted at a certain speed, for example. It is possible that the dispersion relation is relatively complicated for certain flows, an example being the three-layer shear flow of chapter 2 where quite a deal of information can be gleaned from the linearized analysis. It is occasionally the case that a dispersion relation will predict a solitary wave, namely where a steady wave exists as the wavenumber tends to zero. An example of this can be found in the investigation of solitary waves on an intrusion flow by Forbes and Hocking [26].

For unsteady flow a dispersion relation may be used as a stability criterion to determine how an interfacial disturbance will evolve through time. For example a small perturbation may grow exponentially; a case in point being the Kelvin-Helmholtz instability, detailed in chapter 3, as well as numerous other fluid instabilities. A stability criterion may predict that a small wave is stable, namely that when given a perturbation the fluid system will maintain a behaviour such as a travelling or standing wave for certain parameter values. Where the configuration of the flow is complicated it may to be possible to obtain some hybrid of these behaviours, as in the study of the Holmboe instability of Umurhan and Heifetz [61] where a complex variety of solution modes are possible. The chief use of this kind of linearized analysis in the work presented in this thesis is as an aid in choosing parameter values judiciously for use in the corresponding non-linear problems.

In this thesis non-linear interfacial flow problems are typically treated computationally. In particular, for the inviscid flows of chapters 2 and 3 spectral methods are employed to model the shape of the interface and the behaviour of the associated flow region. This approach involves choosing a Fourier series representation

for the solution components and then recasting the problem so that it is the coefficients of the series that are solved for rather than the solution directly. This type of technique has been successfully applied to a variety of problems. The inviscid Rayleigh-Taylor instability was modelled by Forbes, Chen and Trenham [25] where the interface of that buoyancy driven flow was tracked up until just after the point it tips over. A particular advantage to using the spectral technique here was that it allowed for the effects of surface tension and artificial viscosity to be included in a straightforward manner. More generally, an advantage in using a spectral method for problems such as this is that the shape (and even the curvature) of an interfacial wave may be computed to high degree of accuracy for a moderate computational cost. Similar techniques have been employed by Forbes, Hocking and Farrow [27] to study steady waves on an intrusion layer.

It is also possible to apply these techniques to viscous flow, where the solution over an entire computational domain is given a series representation, rather than just the interface. The viscous version of the Rayleigh-Taylor instability was presented by Forbes [24], and here the evolution of the flow at the interface was followed much further than the inviscid version of the problem would allow. A similar approach is used in chapter 4 for a two-layer shear flow. Some disadvantages to these types of methods are that they are occasionally unable to resolve sharp features, such as singularities in curvature, and are prone to the blow-up of higher order modes at later times. Both of these issues will be discussed in detail in chapter 3.

An alternate approach that may be employed in modelling interfacial waves in fluid flow are the more computationally intensive finite difference methods. This approach is adopted in chapter 3 for the viscous version of the Kelvin-Helmholtz instability. In that analysis a rectangular flow domain is discretized with a grid of points and a set of governing equations (namely a Boussinesq version of the Navier-Stokes equation and a mass conservation equation) are solved on this grid. Finite difference methods are a rich field of research and a great variety of techniques

have been developed around this area. Some well known examples are the SIMPLE method, as outlined in Anderson [3] for instance, and alternating difference implicit (ADI) methods, as presented by Tannehill et al. [55]. This former method was used by Farrow and Hocking [21] to model a viscous two-layer withdrawal flow for example. The method used in chapter 3 is an ADI approach and although it is able to compute features of the flow not available to the inviscid spectral method, and do so very accurately, it is nonetheless computationally expensive.

Several flows are considered in detail in this thesis. A key feature of these flows is that they each possess shear and they will each be studied with a view to determining the behaviour of interfacial waves in each flow. Chapter 2 of this thesis presents an investigation of a steady three-layer intrusion flow, in which all three layers are in motion with different speeds relative to the observer. Shear is present in the middle layer, and the lowest fluid may even move oppositely to the upper two (so giving an exchange flow). Two thin interfaces are present, above and below the moving middle layer. A linearized analysis is presented for small wave amplitudes. Non-linear periodic solutions are then obtained using a spectral method based on Fourier series, and these reveal a range of non-linear phenomena, including limiting waves, multiple solutions and resonances. This chapter makes use of and extends some ideas established by Forbes et al. [27] in the study of steady waves on an intrusion layer. The material has perviously appeared in Chen and Forbes [14] and Chen and Forbes [13].

The techniques used to study the intrusion flow are then extended to allow for time-dependent behaviour, and applied to the Kelvin-Helmholtz instability for an inviscid fluid in chapter 3. The viscous version of this problem is also considered. Here, two bounded fluid layers flow parallel to each other with the interface between them growing in an unstable fashion when subjected to a small perturbation. In this problem, and the related problem of the vortex sheet, there are several phenomena associated with the evolution of the interface, notably the formation of a finite time curvature singularity for inviscid fluids and the ‘roll-up’ of the interface when

viscosity is included. Two contrasting computational schemes will be presented. A spectral method is used to follow the evolution of the interface in the inviscid version of the problem. A similar method has previously been used by Forbes, Chen and Trenham [25] to model the inviscid Rayleigh-Taylor instability. This allows the interface shape to be computed up to the time that a curvature singularity forms, with several computational difficulties overcome to reach that point. A weakly compressible viscous version of the Kelvin-Helmholtz problem is studied using finite difference techniques and a vorticity-streamfunction formulation. The two versions have comparable, but not identical, initial conditions and so the results exhibit some differences in timing. By including a small amount of viscosity the interface may be followed to the point that it rolls up into a classic ‘cat’s-eye’ shape. Particular attention is given to computing a consistent initial condition and solving the continuity equation both accurately and efficiently. The material in this chapter has been submitted to the Journal of Computational Physics [15].

The final problem studied in this thesis is a two-layer shear flow for inviscid and viscous fluids. Here, the layers flow between two horizontal walls and are buoyantly stable. Each layer contains a finite amount of shear and the horizontal velocity is specified such that it is continuous when unperturbed. The interface between the two layers is given a small sinusoidal perturbation and the subsequent response of the system is studied. Different solution techniques are employed for the inviscid and viscous flow. These both rely on linearizing the governing equations for each of these flows. As a consequence, several restrictions are placed on how the viscous flow may evolve; namely that as it develops the flow will not differ too greatly from the unperturbed flow. These assumptions are justified since standing wave behaviour is expected in the inviscid case. Solutions are presented for a variety of different values of the shear parameters and the way these parameter choices affect the interaction between vorticity and density in the viscous case is investigated in detail. A paper based on the material in this chapter has been submitted to the European Journal of Mechanics - B/Fluids [16].

CHAPTER 2

Steady periodic waves in a 3-layer fluid with shear in the middle layer

2.1. Introduction

The propagation of steady periodic waves in layered fluids is a well documented phenomenon. Such a situation may arise when the continuous density profile of an ocean or atmosphere has been approximated to one made up of multiple horizontal layers of constant density. Typically systems of two or three layers are considered, usually under the influence of gravity, with interest lying principally in the shape of the interfacial wave profile(s).

Previous models have varied in complexity with the inclusion of a range of effects and approximations. A simple case is that of Saffman and Yuen [51] who considered steady finite amplitude periodic waves on a vortex sheet. Their work proposes the existence of limiting cases (such as Stokes' corners and overhanging waves as later computed by Meiron and Saffman [40] and Turner and Vanden-Broeck [60]) as well as making a distinction between the existence of steady solutions and their stability. Another two-layer flow is that considered by Pullin and Grimshaw [48] which included constant vorticity and a rigid lid in the upper layer. This Boussinesq flow displays an impressive range of geometrically limiting cases, which alter markedly as a physical parameter such as upper layer depth is varied.

More recently some equally interesting results have been published for the case of three-layer fluids. Although this is a natural extension, it is complicated somewhat by the presence of two interfaces. Such situations have been characterised as possessing free-surface waves which may induce or interact with internal interfacial waves (Părău and Dias [43]). Michallet and Dias [41] have considered waves in

three-layer systems that contain rigid horizontal walls above the uppermost fluid and below the lowermost one. Their focus was on the interaction between long and short wavelength modes of solutions. Similar effects were studied in nearly identical situations by both Rusås and Grue [49] and Vanden-Broeck and Turner [62]. These latter authors included a middle layer of continuously varying density, and computed long waves with oscillatory tails.

The experimental work done on these types flows is instructive. Sutherland et al. [54] looked at an intrusive gravity current propagating in a two-layer fluid. This was extended to account for more complex stratification by Flynn and Sutherland [23], who included a lower layer of variable density. Further work by Mehta et al. [39] on intrusions into two and three-layer fluids of constant density emphasises the generation of solitary wave type phenomena. These studies illustrate the variety of practical contexts to which these intrusion flows apply, and confirm the relevance of the theoretical calculations of the type presented here.

The present work extends that of Forbes et al. [27] which dealt with periodic waves on an intrusion layer flowing into a stationary fluid. In that paper, the simplification of only allowing the central layer to be in motion permitted limiting waves (with sharp corners at the crests) to be computed, while resonant interactions were unavailable (or at least not found in their numerical results). Solitary wave-type solutions are also permitted for this configuration, and were obtained by Forbes and Hocking [26] using both weakly nonlinear theory and direct numerical calculation. The computation of generalized solitary waves on fluid interfaces is a rich field of research. Akylas and Grimshaw [2] obtained solitary waves with oscillatory tails, for instance, while Rusås and Grue [49] have computed extreme overhanging solitary waves in a three-layer fluid. The effect of linear density stratification in each layer on the propagation of solitary waves has been examined by Fructus and Grue [28].

The three-layer model presented here is a straightforward one. Each layer is of constant density, and is inviscid and incompressible. Shear (constant vorticity) is

present in the middle layer, with the two outer layers flowing (when unperturbed) at a constant speed, such that velocity is continuous at the two interfaces. Historically, interest in systems of this type has been with regard to their stability to small perturbations. Lamb [35, article 232] reported on the solution obtained by Rayleigh, for the stability of an intrusion ‘jet’. This linearized analysis was summarized and extended by Forbes et al [27]. A stability analysis of the present problem was first given by Taylor [56]. Chandrasekhar [11] repeated this analysis with the slight simplification of only considering small density differences between the layers. The stability of the waves will not be considered here however, with the focus instead being on computing the shape of the interfaces in steady flow. As discussed by Saffman and Yuen [51] and Turner and Vanden-Broeck [60], it is legitimate to make a distinction between the existence of finite amplitude steady periodic solutions and their stability. Techniques developed by Forbes et al. [27] to compute periodic nonlinear interface shapes for the related problem of intrusion currents will be adapted to the present situation. Problems of this type (and shear flows in particular) have previously yielded wave profiles with overhanging portions (for instance, Turner and Vanden-Broeck [60] and Pullin and Grimshaw [48]) and the numerical scheme will be extended to account for this possibility.

The flow we consider here is physically relevant to a number of geophysical situations. For instance in Williams et al. [65] the circulation generated beneath melting ice sheets and the subsequent interaction of fresh and salt water gives rise to a type of intrusive current. In a similar fashion the agricultural run-off or inflow into a stratified reservoir may produce an intrusion flow when it reaches its neutral bouyancy; see for example Forbes et al. [27]. The outflow of water from the Mediterranean sea into the North Atlantic, as outlined in Candela [9], and the associated phenomenon of ‘meddies’ is a larger scale example of this kind of flow. Here patches of circulating warm salty water contribute significantly to variations in salinity as they drift around the region.

In this chapter, the steady model is formulated in such a way that it is possible to specify that the upper and lower layers flow in opposite directions, giving a so-called exchange flow. Such flows occur in a wide range of situations, for instance in the strait of Gibraltar as discussed by Timmermans and Pratt [57]. They are also studied from a hydraulic perspective (e.g. Armi and Farmer [4]) with view to finding some maximal flow rate solution.

It has been seen in work on similar problems, such as that of Părău and Dias [43] and Rusås and Grue [49], that for a given choice of physical parameters there may be small amplitude solutions available at multiple wavelengths for the same wave speed. In such cases it may be possible, in a nonlinear regime, to obtain resonant interactions between these solution modes where their respective wavelengths are near integer multiples. Interactions of this type are not dissimilar to Wilton's ripples (Wilton [66]), which are encountered for periodic gravity waves with surface tension, or the gravity-capillary waves of Chen and Saffman [12] where various resonances (or 'combination waves') were excited as a surface tension parameter was varied. Such waves have been seen experimentally by Mehta [39] for the case of a bulbous intrusion into a stationary layered fluid. In this chapter it will be seen that superharmonic resonant interactions are readily available and coincide with complicated relationships between various physical parameters. These types of resonances are often characterised as an interaction between internal and external modes (Lewis et al. [36] and Părău and Dias [43]), although this is not necessarily an accurate interpretation here.

The model will be derived in section 2.2. A linearized solution is presented in section 2.3, hinting at the possibility of resonant effects and multiple solutions. Section 2.4 introduces a numerical solution method based on Fourier series and a simple Galerkin technique. A multitude of nonlinear solutions for moderate to large amplitude waves is shown in section 2.5. These are compared to the linearized solution and reveal a wide array of nonlinear phenomena.

2.2. Model and governing equations

We consider a system composed of three horizontal fluid layers, all of which are in motion, as illustrated in Figure 2.1. Throughout this chapter of the thesis, the top layer will be denoted as layer 1, the middle as layer 2 and the lowest as layer 3. Each fluid layer has constant density ρ_i , $i = 1, 2, 3$, with $\rho_1 < \rho_2 < \rho_3$, and there are constant horizontal background flow speeds c_1 and c_3 in the top and bottom layers, respectively. There are two free interfaces, $y = \eta_U$ and $y = \eta_L$, at the upper and lower boundaries of the middle layer. The upper and lower layers are unbounded, of infinite vertical extent. Constant vorticity (shear) is present in the middle layer, where the background speed is such that it matches the outer layer speeds in the case of flat interface profiles. All fluids are assumed to be incompressible and inviscid. The upper and lower layers are also assumed to flow irrotationally. The flow is steady and subject to the downward acceleration g of gravity. The shape of the two interfaces will be of particular interest.

Non-dimensional variables will be introduced. The height of the middle layer, h , is used as a length scale. A typical speed, \sqrt{gh} , is chosen as the velocity scale with velocity potentials scaled with $h\sqrt{gh}$. The density scale is ρ_2 , the density of the middle layer. Recasting the problem in these terms, the system is characterised by four dimensionless parameters:

$$F_1 = \frac{c_1}{\sqrt{gh}} \quad F_3 = \frac{c_3}{\sqrt{gh}} \quad (2.2.1)$$

$$D_1 = \frac{\rho_1}{\rho_2} \quad D_3 = \frac{\rho_3}{\rho_2}. \quad (2.2.2)$$

Here F_1 and F_3 are Froude numbers for the upper and lower layers respectively. These are the fluid celerities made dimensionless with respect to the characteristic speed \sqrt{gh} of a wave in the middle layer. The two remaining parameters D_1 and D_3 are density ratios relative to the density ρ_2 of the middle layer, with $D_1 < 1$ and $D_3 > 1$. The appropriate form of the background speed in the middle layer is,

$$F_2(y) = F_3 + (F_1 - F_3)y. \quad (2.2.3)$$

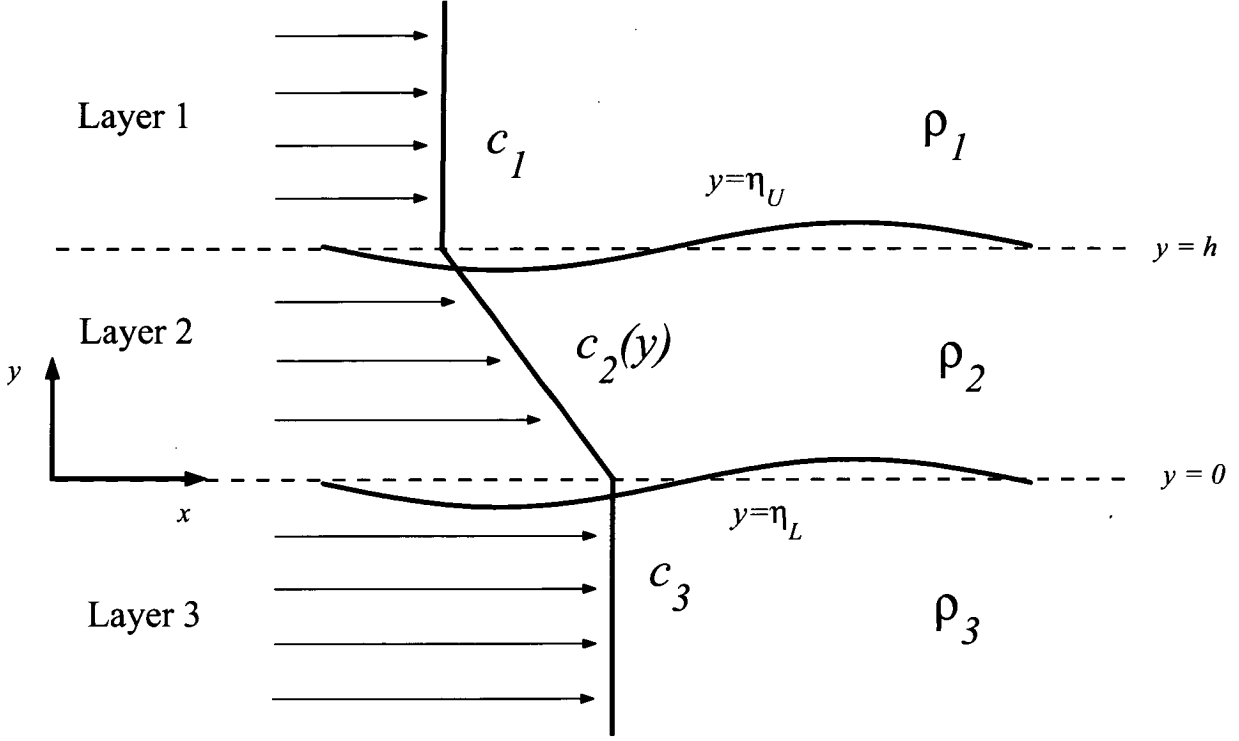


FIGURE 2.1. Diagram of the flow configuration showing the three fluid layers moving horizontally with waves propagating at the two interfaces $y = \eta_U$ and $y = \eta_L$ above and below the middle layer.

Here the linear dependence on y represents the constant shear. The fluid speed in this layer matches those of the upper and lower layers on the planes $y = 1$ and $y = 0$, respectively.

In each layer we define a velocity vector $\mathbf{q}_i = u_i \mathbf{i} + v_i \mathbf{j}$ ($i = 1, 2, 3$). For the two outer layers \mathbf{q}_i is the gradient of a velocity potential ϕ_i ,

$$\begin{aligned} \phi_i &= F_i x + \Phi_i \\ \mathbf{q}_i &= \left(F_i + \frac{\partial \Phi_i}{\partial x} \right) \mathbf{i} + \frac{\partial \Phi_i}{\partial y} \mathbf{j} \quad (i = 1, 3). \end{aligned} \quad (2.2.4)$$

The velocity vector in the middle layer, \mathbf{q}_2 , may be expressed in a similar fashion,

$$\mathbf{q}_2 = \left(F_3 + (F_1 - F_3)y + \frac{\partial \Phi_2}{\partial x} \right) \mathbf{i} + \frac{\partial \Phi_2}{\partial y} \mathbf{j}. \quad (2.2.5)$$

Here we have effectively written the velocity as the sum of a rotational part (the linear shear term) and an irrotational part (gradient of the velocity potential Φ_2). Having done this we may also determine the streamfunction in the middle layer,

$$\psi_2(x, y) = F_3 y + \frac{1}{2}(F_1 - F_3)y^2 + \Psi_2(x, y) \quad (2.2.6)$$

where the irrotational part of the streamfunction, Ψ_2 , is related to irrotational velocity potential Φ_2 by the Cauchy-Riemann equations.

Conservation of mass requires that ϕ_1 , Φ_2 and ϕ_3 satisfy Laplace's equation in each fluid layer,

$$\nabla^2 \phi_1 = 0 \quad \text{in} \quad \eta_u < y < \infty \quad (2.2.7)$$

$$\nabla^2 \Phi_2 = 0 \quad \text{in} \quad \eta_L < y < \eta_U \quad (2.2.8)$$

$$\text{and } \nabla^2 \phi_3 = 0 \quad \text{in} \quad -\infty < y < \eta_L. \quad (2.2.9)$$

It is of note that the shape of these layers is determined by the shape of the two interfaces (not known a priori) making this a highly nonlinear problem.

There are several boundary conditions which need to be defined on each interface. Two kinematic conditions on the upper interface require that neither the upper nor middle fluid layers may cross the interface,

$$v_i = u_i \frac{\partial \eta_U}{\partial x} \quad (i = 1, 2) \quad \text{on } y = \eta_U(x). \quad (2.2.10)$$

A single dynamic condition,

$$\begin{aligned} & \frac{1}{2} D_1 F_1^2 - \frac{1}{2} D_1 (u_1^2 + v_1^2) - D_1 (\eta_U - 1) \\ &= \frac{1}{2} F_3^2 - \frac{1}{2} (u_2^2 + v_2^2) + (F_1 - F_3) \psi_2 - (\eta_U - 1) \quad \text{on } y = \eta_U(x), \end{aligned} \quad (2.2.11)$$

is obtained (via Bernoulli's equation) by equating pressure in each layer at the interface.

Similarly, there are two kinematic conditions on the lower interface,

$$v_i = u_i \frac{\partial \eta_L}{\partial x} \quad (i = 2, 3) \quad \text{on } y = \eta_L(x), \quad (2.2.12)$$

for each of the lower and middle layers. The dynamic condition on the lower interface is

$$\begin{aligned} & \frac{1}{2}F_3^2 - \frac{1}{2}(u_2^2 + v_2^2) + (F_1 - F_3)\psi_2 - \eta_L \\ = & \frac{1}{2}D_3F_3^2 - \frac{1}{2}D_3(u_3^2 + v_3^2) - D_3\eta_L \quad \text{on } y = \eta_L(x). \end{aligned} \quad (2.2.13)$$

The infinite vertical extent of the upper and lower fluids requires that

$$\begin{aligned} \phi_1 &\rightarrow F_1 x \quad \text{as } y \rightarrow +\infty \\ \phi_3 &\rightarrow F_3 x \quad \text{as } y \rightarrow -\infty \end{aligned} \quad (2.2.14)$$

for a solution to be physically reasonable. Our interest lies in investigating the nature of periodic waves on the interfaces. As such we seek periodic solutions in x for $\phi_1, \Phi_2, \phi_3, \eta_U$ and η_L which satisfy equations (2.2.7) - (2.2.14). To this end we assume that the system is also dependent on some dimensionless wavenumber, k , which is thus an additional dimensionless parameter, along with the Froude numbers (2.2.1) and density ratios (2.2.2), needed to specify a solution completely.

2.3. Linearized solution

We now present a linearized solution to the governing equations (2.2.7)–(2.2.14). This corresponds to the case of the two free surface shapes being sinusoidal in x and of small amplitude. In effect we use a small perturbation about the trivial solution of flat interfaces and background flow for the velocity in each fluid layer, similar to that presented by Taylor [56] but without the time dependence. The velocity

potentials in (2.2.7)–(2.2.9) are expressed by means of the perturbed expansions,

$$\phi_1(x, y) = F_1 x + \epsilon \Phi_{11}(x, y) + \mathcal{O}(\epsilon^2) \quad (2.3.1)$$

$$\Phi_2(x, y) = \epsilon \Phi_{21}(x, y) + \mathcal{O}(\epsilon^2) \quad (2.3.2)$$

$$\phi_3(x, y) = F_3 x + \epsilon \Phi_{31}(x, y) + \mathcal{O}(\epsilon^2), \quad (2.3.3)$$

while the lower and upper interface profiles are perturbations about $y = 0$ and $y = 1$ respectively,

$$\eta_L(x) = \epsilon H_{L1}(x) + \mathcal{O}(\epsilon^2) \quad (2.3.4)$$

$$\eta_U(x) = 1 + \epsilon H_{U1}(x) + \mathcal{O}(\epsilon^2). \quad (2.3.5)$$

Here ϵ is a small parameter with magnitude in the order of the amplitude of the wave. Appropriate solutions to Laplace's equation are chosen for each velocity potential, up to a multiplicative constant,

$$\Phi_{11}(x, y) = a_{11} e^{-k(y-1)} \sin kx \quad (2.3.6)$$

$$\Phi_{31}(x, y) = a_{31} e^{ky} \sin kx \quad (2.3.7)$$

$$\Phi_{21}(x, y) = (c_2 \cosh(ky) + d_2 \sinh(ky)) \sin kx. \quad (2.3.8)$$

These have been chosen to have period $2\pi/k$ in x , to be odd with respect to x and to have the properties that Φ_{11} and Φ_{31} decay to zero as $y \rightarrow \infty$ and $y \rightarrow -\infty$, respectively. The perturbed streamfunction (2.2.6) in the middle layer, ψ_2 , takes the linearized form

$$\psi_2(x, y) = F_3 y + \frac{1}{2}(F_1 - F_3)y^2 + \epsilon \Psi_{21}(x, y) + \mathcal{O}(\epsilon^2) \quad (2.3.9)$$

in which Ψ_{21} is determined from the Cauchy-Riemann equations to be

$$\Psi_{21}(x, y) = (c_2 \sinh(ky) + d_2 \cosh(ky)) \cos kx. \quad (2.3.10)$$

The corresponding interface profiles will be periodic, even functions in x , and will have the forms

$$\begin{aligned} H_{L1}(x) &= \cos kx \\ H_{U1}(x) &= \alpha \cos kx \end{aligned} \quad (2.3.11)$$

where α is to be determined. Substituting this perturbed solution into the boundary conditions (2.2.10)–(2.2.13) and then discarding any terms of order ϵ^2 or higher we obtain a system of six algebraic equations. These may be solved to yield the dispersion relation

$$\mathcal{D}_1 k F_3^2 + \mathcal{D}_3 k F_1^2 + \mathcal{D}_1 \mathcal{D}_3 \tanh k + k^2 F_1^2 F_3^2 \tanh k = 0, \quad (2.3.12)$$

$$\text{where } \mathcal{D}_1 = D_1 k F_1^2 - F_1(F_1 - F_3) - (1 - D_1),$$

$$\text{and } \mathcal{D}_3 = D_3 k F_3^2 + F_3(F_1 - F_3) - (D_3 - 1).$$

This relation determines the co-dependency of the Froude numbers on wavenumber such that equations (2.2.7)–(2.2.14) are satisfied to first order in the parameter ϵ . Equation (2.3.12) contains cubic powers of the Froude numbers, suggesting that up to three linear solutions may exist for some fixed wavenumber. Likewise the expression involves nonlinear functions of wavenumber k which indicates that, for fixed Froude numbers (2.2.1) and density ratios (2.2.2), there may be multiple linear solutions of different wavenumber. It is impractical to try to characterize completely the effect of varying each of the five non-dimensional parameters, so the density ratios, D_1 and D_3 , will be held constant at values close to 1 (representative of stratified oceans or reservoirs), and the upper layer Froude number will be chosen as $F_1 = 0.1$, throughout the results presented here.

2.3.1. The linearized dispersion relation. Although the dispersion relation (2.3.12) must ultimately be solved numerically to determine the relationship between wavenumber k and Froude number F_3 , it is instructive to consider first a limiting case. For short wavelengths (that is large wavenumber, k) we put $\tanh k \approx 1$ to reduce (2.3.12) to a simple cubic in F_3 . This may be solved exactly to give the three approximate values

$$F_3 \approx \frac{1 - D_1 + F_1^2(1 - k - kD_1)}{F_1} \quad (2.3.13)$$

$$\text{and, } F_3 \approx \frac{-F_1 \pm \sqrt{F_1^2 + 4(1 - k - D_3 + kD_3^2)}}{2(kD_3 + k - 1)} \quad (2.3.14)$$

for the speed F_3 of the lowest fluid layer. The first of these (2.3.13) takes the opposite sign to F_1 (for large enough k), suggesting that the lower layer may flow in the opposite direction to the upper layer; this is therefore an ‘exchange flow’. The two solutions in equation (2.3.14) have slower speeds in the bottom layer, and typical parameter values give one positive and one negative value for F_3 .

A numerical solution to (2.3.12) is required for small and moderate values of k . This is obtained by holding D_1 , D_3 and F_1 constant, choosing a value for k and then solving for F_3 with Newton’s method. This was repeated over a range of initial values of F_3 that were chosen to allow for multiple solutions at the same wavenumber. Having done this we may compare the relative amplitude and phase of the two linearized interfaces in equation (2.3.11) by taking

$$\alpha = \frac{H_{U1}}{H_{L1}} = \frac{1}{(1 - D_1)kF_3} [kF_1(D_3 \cosh k + kF_3^2 \sinh k) + (D_1kF_1 - (F_1 - F_3))(kF_3^2 \cosh k + D_3 \sinh k)], \quad (2.3.15)$$

which will be negative if the interfaces are out of phase and positive if they are in phase. The ratio α goes to infinity as F_3 passes through zero, simply indicating a flat lower interface at this point.

An example solution is shown in Figure 2.2. Physically reasonable parameter values have been chosen with $D_1 = 0.99$, $D_3 = 1/D_1$ and $F_1 = 0.1$. These values

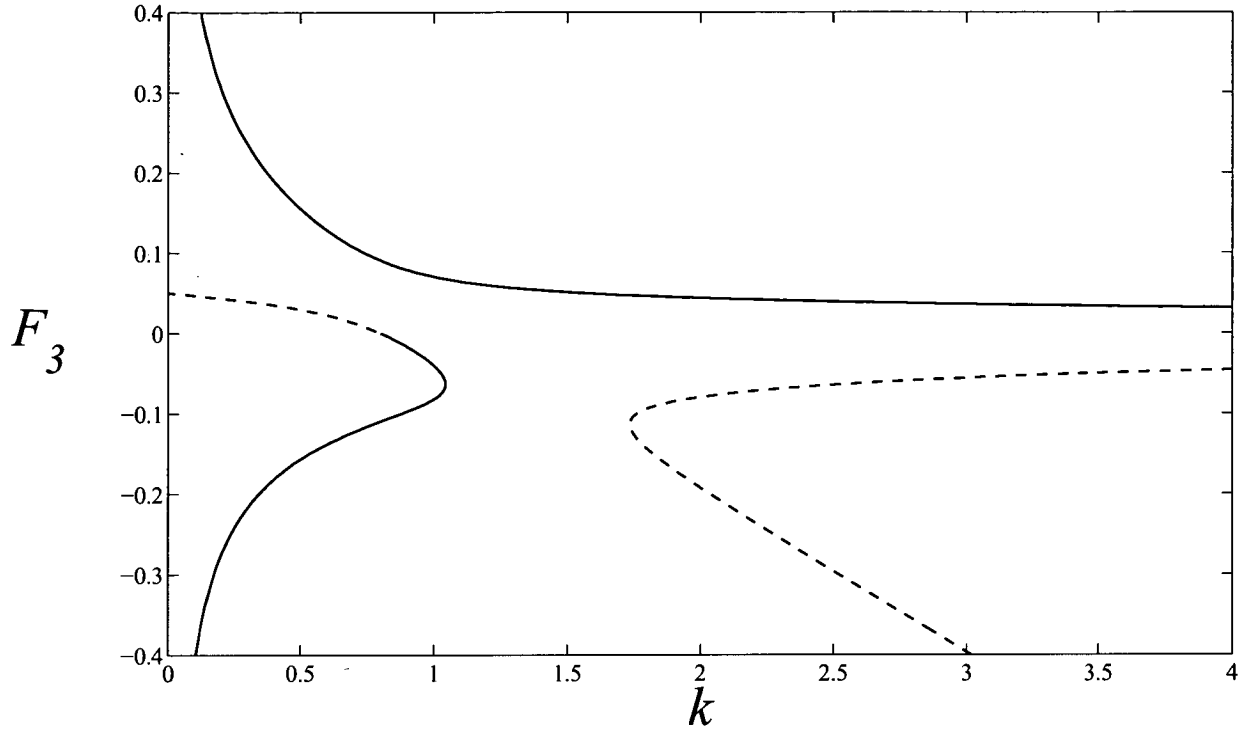


FIGURE 2.2. Plot of the linearized dispersion relation (3.12) to give the relationship between wavenumber k and lower layer Froude number F_3 . The parameter values chosen are upper layer Froude number $F_1 = 0.1$ and density ratios $D_1 = 0.99$ and $D_3 = 1/0.99$.

have been taken to be representative of typical situations encountered in oceanography; see Phillips [45]. In the diagram, in-phase solutions are represented by solid lines with out-of-phase solutions represented by dashed lines. For this example we see three distinct solution branches: an in-phase solution for all k with positive F_3 ; an out-of-phase solution available for $k > \kappa_2$ with two negative F_3 values at each wavenumber; and a solution valid for $k < \kappa_1$ that emerges, out-of-phase, from $k = 0$ with positive Froude number, switches phase as it passes through $F_3 = 0$ and then has long wavelength solutions for increasingly strongly negative F_3 . Here, the values κ_1 and κ_2 represent wavenumbers at which the linearized solution branches in Figure 2.2 have turning points, with vertical slopes. Two additional points of

interest on this final branch are the Froude number where $k = 0$,

$$F_{30} = \frac{(1 - D_1)(D_3 - 1)}{F_1(D_3 - D_1)} = 5.025 \times 10^{-2}, \quad (2.3.16)$$

possibly corresponding to a solitary wave-like solution, and the wavenumber, κ_0 , for $F_3 = 0$ which from equation (2.3.12) satisfies

$$\kappa_0 F_1^2 + [\kappa_0 F_1^2 D_1 - F_1^2 - (1 - D_1)] \tanh \kappa_0 = 0 \quad (2.3.17)$$

and may easily be found numerically (in this case $\kappa_0 = 0.8022$). Similarly we may calculate the turning points κ_1 and κ_2 by taking the derivative of equation (2.3.12) with respect to F_3 giving, in this case, $\kappa_1 = 1.044$ and $\kappa_2 = 1.735$.

It can be seen that two solutions exist (one in-phase and one out-of-phase) for lower layer Froude number less than the value F_{30} of equation (2.3.16). Where the wavenumbers of two such solutions are integer multiples of each other there is the possibility of resonant behaviour, with solutions from the two branches superposed. Previous studies (e.g. Părău and Dias [43]) have found that in a nonlinear regime such resonances are readily excited for moderate to large amplitude nonlinear waves, since at a fixed wavenumber, the Froude number may vary (from its linearized value) as amplitude increases, allowing nearby resonances to be encountered. The likelihood of a particular resonance being available for a value of F_3 may be evaluated with the aid of Figure 2.3. Here the ratio of the short and long wavenumbers has been plotted against F_3 . It can be seen that this ratio becomes large for strongly negative F_3 , as well as where $F_3 \rightarrow F_{30}$ and $F_3 \rightarrow 0$. The dotted horizontal lines indicate where the ratio is integer valued. It may be seen that, for instance, linear theory predicts 1:2 type resonances near $F_3 \approx -0.08$.

2.4. Nonlinear solutions and numerical scheme

We will now outline a numerical procedure to obtain periodic solutions to the (fully nonlinear) equations (2.2.7) - (2.2.14). This is essentially a Galerkin-type

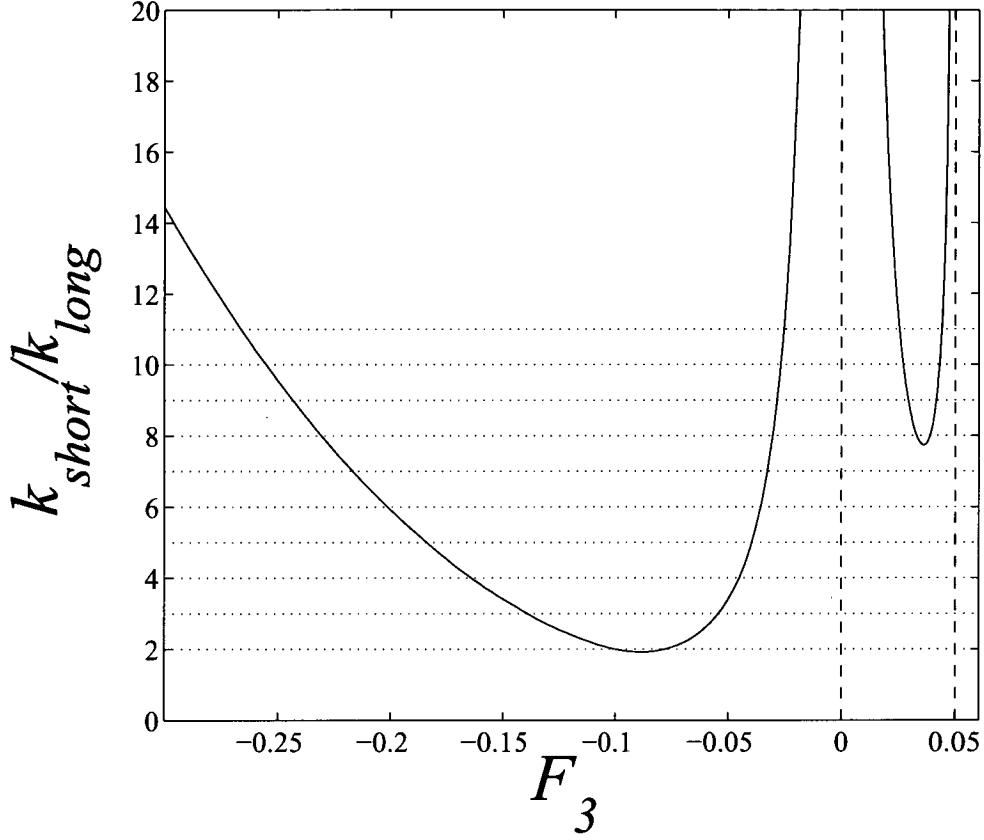


FIGURE 2.3. Plot of the ratio of wavenumbers when two linearized solutions exist for the same lower layer Froude number. The lower-layer Froude number F_3 is shown on the horizontal axis. Linear resonance is possible where the ratio is integer valued.

method used to determine the coefficients of some Fourier series. There is a possibility that the interfacial profiles may become multivalued (as in Pullin and Grimshaw [48] and Rus  s and Grue [49]) and a reparametrization of the system involving arc length will be introduced to deal with this possibility.

Appropriate solutions to Laplace's equations (2.2.7) - (2.2.9) (subject to (2.2.14)) will be Fourier series of the form

$$\Phi_1 = \sum_{n=1}^N B_n e^{-nk(y-1)} \sin nkx \quad (2.4.1)$$

$$\Phi_2 = \sum_{n=1}^N \left[C_n \cosh nk\left(y - \frac{1}{2}\right) + D_n \sinh nk\left(y - \frac{1}{2}\right) \right] \sin nkx \quad (2.4.2)$$

$$\Phi_3 = \sum_{n=1}^N F_n e^{nky} \sin nkx \quad (2.4.3)$$

with these approximate solutions becoming exact as $N \rightarrow \infty$. It is occasionally convenient numerically to replace the hyperbolic functions in Φ_2 with simple exponential functions.

It is convenient to parametrize each interface using an arc length s , so that each interface is represented in the form $(x(s), y(s))$. A change of variables will now be made with a scaled arc-length, ξ , defined as

$$\xi = \frac{2\pi s}{L}.$$

Here, L is the total arc length along one wave cycle; this is therefore a parameter which is essentially equivalent to a measure of amplitude and need not be computed explicitly. The use of an arc length leads to an extra condition which must be satisfied on each interface, namely

$$\left(\frac{dx}{d\xi}\right)_{U,L}^2 + \left(\frac{dy}{d\xi}\right)_{U,L}^2 = \frac{L_{U,L}^2}{4\pi^2}, \quad (2.4.4)$$

where the subscripts U and L refer to the upper and lower profiles, respectively. This is derived from the usual Pythagorean relationship $dx^2 + dy^2 = ds^2$. The periodic functions representing the upper interface $(x, y) = (x_U, \eta_U)$ and the lower

interface $(x, y) = (x_L, \eta_L)$ are selected to be Fourier series of the form,

$$\eta_U = 1 + P_0 + \sum_{n=1}^N P_n \cos n\xi \quad (2.4.5)$$

$$\eta_L = R_0 + \sum_{n=1}^N R_n \cos n\xi \quad (2.4.6)$$

$$x_U = \frac{\xi}{k} + \sum_{n=1}^N T_n \sin n\xi \quad (2.4.7)$$

$$x_L = \frac{\xi}{k} + \sum_{n=1}^N U_n \sin n\xi, \quad (2.4.8)$$

which, too, become exact as $N \rightarrow \infty$.

As we seek finite amplitude nonlinear wave solutions for the interface profiles, it is necessary to define some measure of wave amplitude. Half the peak-to-trough displacement of the lower interface, \mathcal{A}_L , is chosen here, and may be calculated from

$$2\mathcal{A}_L = \eta_L(0) - \eta_L(\pi). \quad (2.4.9)$$

This adds an extra parameter to this system, as well as an extra condition which must be satisfied by our solution. Where the upper interface is of much larger amplitude, its displacement may be used instead of equation (2.4.9) to define the amplitude parameter.

A nonlinear solution is characterised by the $8N+3$ coefficients from the velocity potentials (the B_n , C_n , D_n and F_n), the coefficients from the interface profile coordinates (the P_n , R_n , T_n and U_n) and the lower layer Froude number, F_3 . The numerical scheme involves forming a vector of unknowns, \mathbf{V} , from these coefficients,

$$\mathbf{V} = [\mathbf{B}; \mathbf{C}; \mathbf{D}; \mathbf{F}; \mathbf{P}; \mathbf{R}; \mathbf{T}; \mathbf{U}; P_0; R_0; F_3]^T$$

where $\mathbf{B} = [B_1, \dots, B_N]$, $\mathbf{C} = [C_1, \dots, C_N]$ and so on, and then iteratively solving for the components of this vector with a Newton's method routine in $8N+3$ dimensions, seeking to minimize an error vector \mathbf{E} . The first $8N$ components of the error are calculated by successively multiplying (2.2.10)–(2.2.13) and (2.4.4) by a

Fourier basis function (N times for each equation) and integrating over one period. The remaining three sets of components come from the two dynamic conditions (2.2.11) and (2.2.13) integrated over a period and the wave amplitude condition. Explicitly, the components of the error vector \mathbf{E} are derived from the two upper interface kinematic conditions (2.2.10) on $(x, y) = (x_U, \eta_U)$,

$$\int_{-\pi}^{\pi} \left(v_1 \frac{\partial x_U}{\partial \xi} - u_1 \frac{\partial \eta_U}{\partial \xi} \right) \sin j\xi d\xi = 0 \quad (2.4.10)$$

$$\int_{-\pi}^{\pi} \left(v_2 \frac{\partial x_U}{\partial \xi} - u_2 \frac{\partial \eta_U}{\partial \xi} \right) \sin j\xi d\xi = 0 \quad (2.4.11)$$

for $j = 1, \dots, N$, suitably decomposed and integrated. Similarly from the lower interface kinematic conditions (2.2.12), evaluated on $(x, y) = (x_L, \eta_L)$, we obtain

$$\int_{-\pi}^{\pi} \left(v_2 \frac{\partial x_L}{\partial \xi} - u_2 \frac{\partial \eta_L}{\partial \xi} \right) \sin j\xi d\xi = 0 \quad (2.4.12)$$

$$\int_{-\pi}^{\pi} \left(v_3 \frac{\partial x_L}{\partial \xi} - u_3 \frac{\partial \eta_L}{\partial \xi} \right) \sin j\xi d\xi = 0 \quad (2.4.13)$$

for $j = 1, \dots, N$. The upper dynamic condition (2.2.11) is first integrated to give one error component

$$\begin{aligned} \int_{-\pi}^{\pi} \left[\frac{1}{2} F_3^2 - \frac{1}{2} D_1 F_1^2 - \frac{1}{2} (u_2^2 + v_2^2) + \frac{1}{2} D_1 (u_1^2 + v_1^2) \right. \\ \left. + (F_1 - F_3) \psi_2 - (1 - D_1)(\eta_U - 1) \right] d\xi = 0 \end{aligned} \quad (2.4.14)$$

and then multiplied by the even basis functions $\cos j\xi$ to give a further N error components

$$\begin{aligned} \int_{-\pi}^{\pi} \left[\frac{1}{2} F_3^2 - \frac{1}{2} D_1 F_1^2 - \frac{1}{2} (u_2^2 + v_2^2) + \frac{1}{2} D_1 (u_1^2 + v_1^2) \right. \\ \left. + (F_1 - F_3) \psi_2 - (1 - D_1)(\eta_U - 1) \right] \cos j\xi d\xi = 0 \end{aligned} \quad (2.4.15)$$

for $j = 1, \dots, N$. Likewise another $N + 1$ components are obtained by applying the same procedure to the lower dynamic condition (2.2.13),

$$\int_{-\pi}^{\pi} \left[\frac{1}{2}(1 - D_3)F_3^2 - \frac{1}{2}(u_2^2 + v_2^2) + \frac{1}{2}D_3(u_3^2 + v_3^2) + (F_1 - F_3)\psi_2 - (1 - D_3)\eta_L \right] d\xi = 0 \quad (2.4.16)$$

$$\int_{-\pi}^{\pi} \left[\frac{1}{2}(1 - D_3)F_3^2 - \frac{1}{2}(u_2^2 + v_2^2) + \frac{1}{2}D_3(u_3^2 + v_3^2) + (F_1 - F_3)\psi_2 - (1 - D_3)\eta_L \right] \cos j\xi d\xi = 0 \quad (2.4.17)$$

for $j = 1, \dots, N$. Finally, multiplying the two arc length conditions (2.4.4) by the even Fourier basis functions and integrating provides a further $2N$ components of the error vector,

$$\int_{-\pi}^{\pi} \left[\left(\frac{\partial x_U}{\partial \xi} \right)^2 + \left(\frac{\partial \eta_U}{\partial \xi} \right)^2 \right] \cos j\xi d\xi = 0 \quad (2.4.18)$$

$$\int_{-\pi}^{\pi} \left[\left(\frac{\partial x_L}{\partial \xi} \right)^2 + \left(\frac{\partial \eta_L}{\partial \xi} \right)^2 \right] \cos j\xi d\xi = 0 \quad (2.4.19)$$

for $j = 1, \dots, N$. The last component of the error vector comes from the wave amplitude condition (2.4.9) on the lower interface,

$$\sum_{n=1}^N R_n [1 - \cos n\pi] - 2\mathcal{A}_L = 0 \quad (2.4.20)$$

which has been derived using the Fourier series (2.4.6).

All integrals in equations (2.4.10)–(2.4.19) are evaluated using a simple trapezoidal rule over a grid with equal point spacing, since this is exponentially accurate for periodic integrands; see Atkinson [5, page 253]. To this end the interface profiles (and then their associated derivatives) are computed at each of the grid points, and these profiles are used to compute the velocities and streamfunctions on the two free surfaces. All these are used, in turn, to calculate the components of the error vector. It is required that sufficiently many grid points are used for the integrals to be evaluated accurately; success was achieved using about $16N$ grid points. The

number of coefficients used in the series, N , was chosen to be at most 201. It was found that $N = 51$ performed well, with 801 grid points used in the integration.

This numerical scheme is sensitive to the absolute size of the velocity potential coefficients B_n , C_n , D_n and F_n . In particular, the hyperbolic functions in the middle layer potential are susceptible to becoming very large, which in turn affects the convergence of the Newton's method routine. Such ill-conditioning may be avoided by rewriting each coefficient in a new scaled form,

$$B_n = B_n^* \exp(nk(\beta - 1)) \quad (2.4.21)$$

$$\begin{bmatrix} C_n \\ D_n \end{bmatrix} = \begin{bmatrix} C_n^* \\ D_n^* \end{bmatrix} \frac{1}{\cosh nk(\delta - \frac{1}{2})} \quad (2.4.22)$$

$$F_n = F_n^* \exp(-nk\gamma) \quad (2.4.23)$$

with these replacing the original coefficients in the vector of unknowns. For small amplitude waves it is satisfactory for the scaling parameters β , γ and δ to be set to zero. As the amplitude of the waves increases these values may be increased.

To improve the rate of convergence in the Newton's method scheme the initial guess of a previously calculated solution of a smaller amplitude was used; that is, $\mathbf{V}_{i_{init}} = \mathbf{V}_{i-1_{final}}$. This was further improved (on occasion) by using a scaled linear interpolation based on two previous solutions of smaller amplitude with the initial guess,

$$\mathbf{V}_{i_{init}} = \mathbf{V}_{i-1_{final}} + (\mathbf{V}_{i-1_{final}} - \mathbf{V}_{i-2_{final}}) \frac{\mathcal{A}_i - \mathcal{A}_{i-1}}{\mathcal{A}_{i-1} - \mathcal{A}_{i-2}}$$

although this is only of use where the relationship between Froude number and amplitude varies monotonically.

The Newton's routine involves calculating a Jacobian matrix of first derivatives at each iteration, $\mathbf{J} = [\partial E_i / \partial V_j]$. For longer wavelength cases and moderate amplitudes it was sufficient to calculate this matrix using a simple forward difference routine. However shorter wavelength solutions were found to be more sensitive to the choice of scaling parameters and it was difficult to calculate limiting solutions

when the approximate Jacobian was used. In such cases the exact Jacobian was used, and this also saw a slight increase in the efficiency of the routine.

2.5. Results

The numerical scheme outlined in section 2.4 was run extensively. For each set of nonlinear solutions the wavenumber was fixed and the lower layer Froude number allowed to vary with amplitude. Throughout, the density ratios were fixed at the same values $D_1 = 0.99$ and $D_3 = 1/0.99$ illustrated in Figure 2.2, for the linearized solution of section 2.3. From Figure 2.2 it may be seen that there are two regions of wavelength where three linearized solutions of different lower Froude number exist. This was of consideration in selecting the nonlinear solutions to compute, with a wavelength from each chosen for further investigation. Firstly, a long wavelength case (with two in-phase solutions and one out-of-phase solution) at $k = 0.5$ was selected and, secondly, a shorter wavelength case at $k = 2.5$ (with two out-of-phase solutions and one in-phase solution) was also chosen. In each of these six cases the linearized solution agrees very well with the computed small amplitude nonlinear solutions. Unless otherwise stated all solutions have been computed with $N = 51$, which was found to be a sufficient number of coefficients to evaluate the interfacial profiles reliably.

It will be seen that many of the following results involve a delicate relationship between F_3 and amplitude, in which two solutions occur for nearly indistinguishable values of those parameters. These fine features were obtained by first calculating solutions using fewer coefficients (typically $N = 31$), for which such features are much coarser, and less accurate. This lower coefficient solution is then used as an initial guess in Newton's method to obtain results for solutions of successively more coefficients (up to the desired $N = 51$) which would otherwise be extremely difficult to compute from other starting guesses. As a check, results in a number of cases have been run with as many as $N = 101$ Fourier coefficients; this is computationally

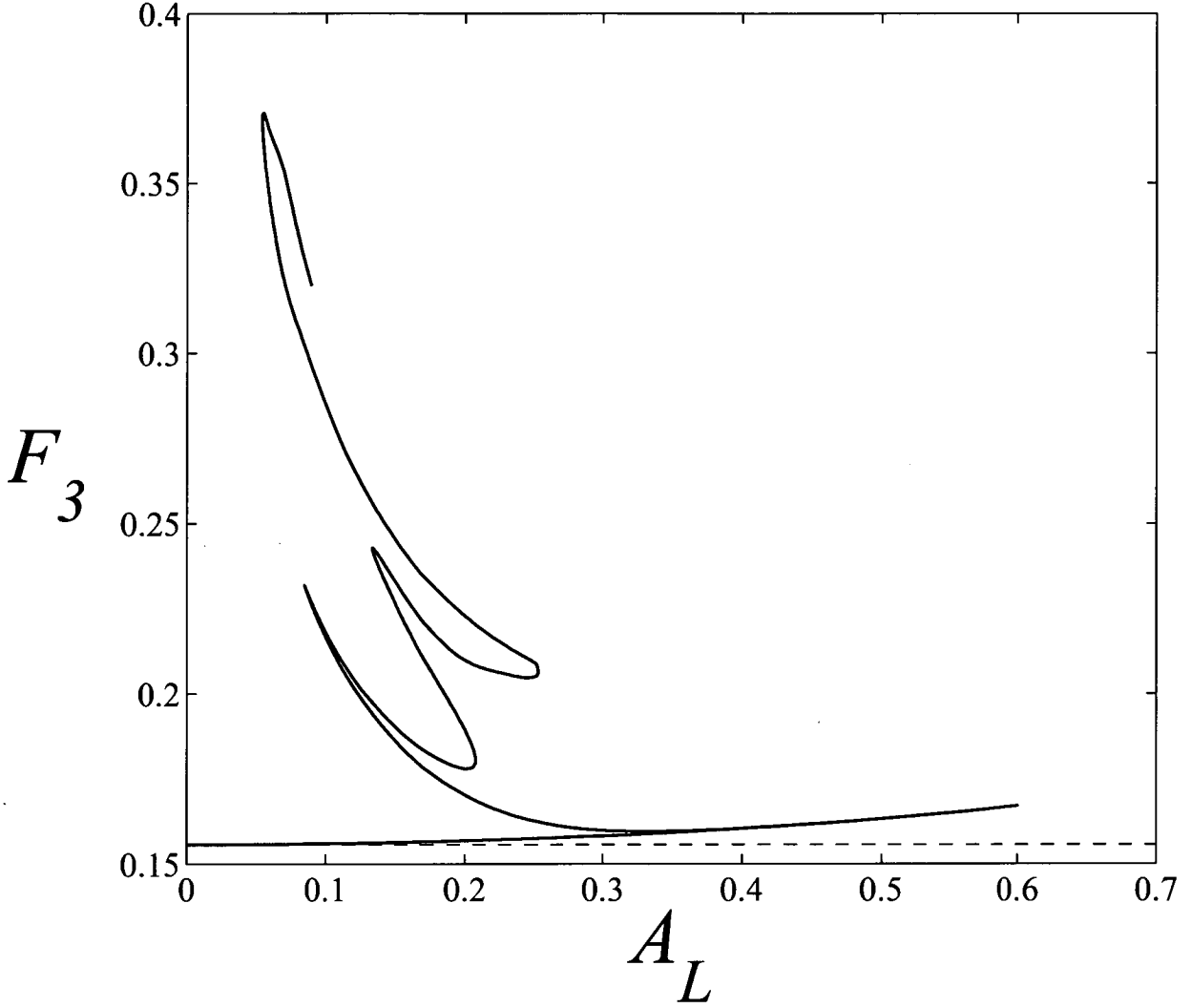


FIGURE 2.4. Dependence of Froude number F_3 on lower wave amplitude A_L for $k = 0.5$, the in-phase case with positive Froude number.

demanding, but does not significantly affect the results, confirming that the results with $N = 51$ coefficients have already converged to a good degree of accuracy.

2.5.1. Results for $k = 0.5$. The first solution we will consider is the in-phase wave with positive lower layer Froude number. The linearized solution predicts that at small amplitudes $F_3 = 0.1556$ with the amplitudes of the two interfaces in the ratio $\alpha = H_{U1}/H_{L1} = 1.3177$. The nonlinear solution is shown in figure 2.4 as

a solid curve, and the linearized result is drawn with a dashed line. The two are in very close agreement for small amplitude. However, as the nonlinear (\mathcal{A}_L, F_3) curve is followed, a more complicated situation arises.

At first, lower layer Froude number increases with amplitude up to a maximum of $\mathcal{A}_L \approx 0.6$. This maximum corresponds to a solution for which there are two slightly square sinusoids of similar amplitude on the two interfaces. From this maximum both amplitude and lower layer Froude number decrease, backtracking along the (\mathcal{A}_L, F_3) curve very closely, before diverging away from this at moderate amplitudes. The solutions along this portion of the curve appear, initially, to approach the configuration of a triangle wave on the upper interface and a moderate amplitude sinusoid on the lower interface. However, near the solution at $(\mathcal{A}_L, F_3) \approx (0.1, 0.24)$ the upper interface develops a small lump at its trough, a feature that is maintained as these solutions are followed in (\mathcal{A}_L, F_3) space.

The interfacial profiles associated with the solutions from the first four of the peak-like artifacts on the amplitude-Froude number curve are shown in figure 2.5. The largest of these, drawn with solid lines, represents a solution for $(\mathcal{A}_L, F_3) = (0.601, 0.167)$. The dashed lines are the solution for $(\mathcal{A}_L, F_3) = (0.0844, 0.232)$, the profiles for $(\mathcal{A}_L, F_3) = (0.133, 0.243)$ are illustrated with dotted lines while the dash-dot lines represent the highest Froude number solution at $(\mathcal{A}_L, F_3) = (0.0547, 0.371)$. In the last three of these solutions a dimple-like lump can be seen at the trough of the upper interface. In addition, for the highest Froude number case a steep bump at the crest of the upper interface has evolved. A bump of this type also appears in the last solutions obtained before the numerical method diverged, and may possibly indicate the incipient formation of a limiting structure such as an overhanging ‘mushroom’ near the crest.

The linearized solution for the out-of-phase branch at this wavelength predicts that $F_3 = 0.02986$, with $\alpha = -2.3013$, shown in figure 2.6 as a horizontal dotted line. Again, the nonlinear solution (the solid and dashed lines in figure 2.6, with the amplitude \mathcal{A}_U of the upper interface being used for convenience) is in close

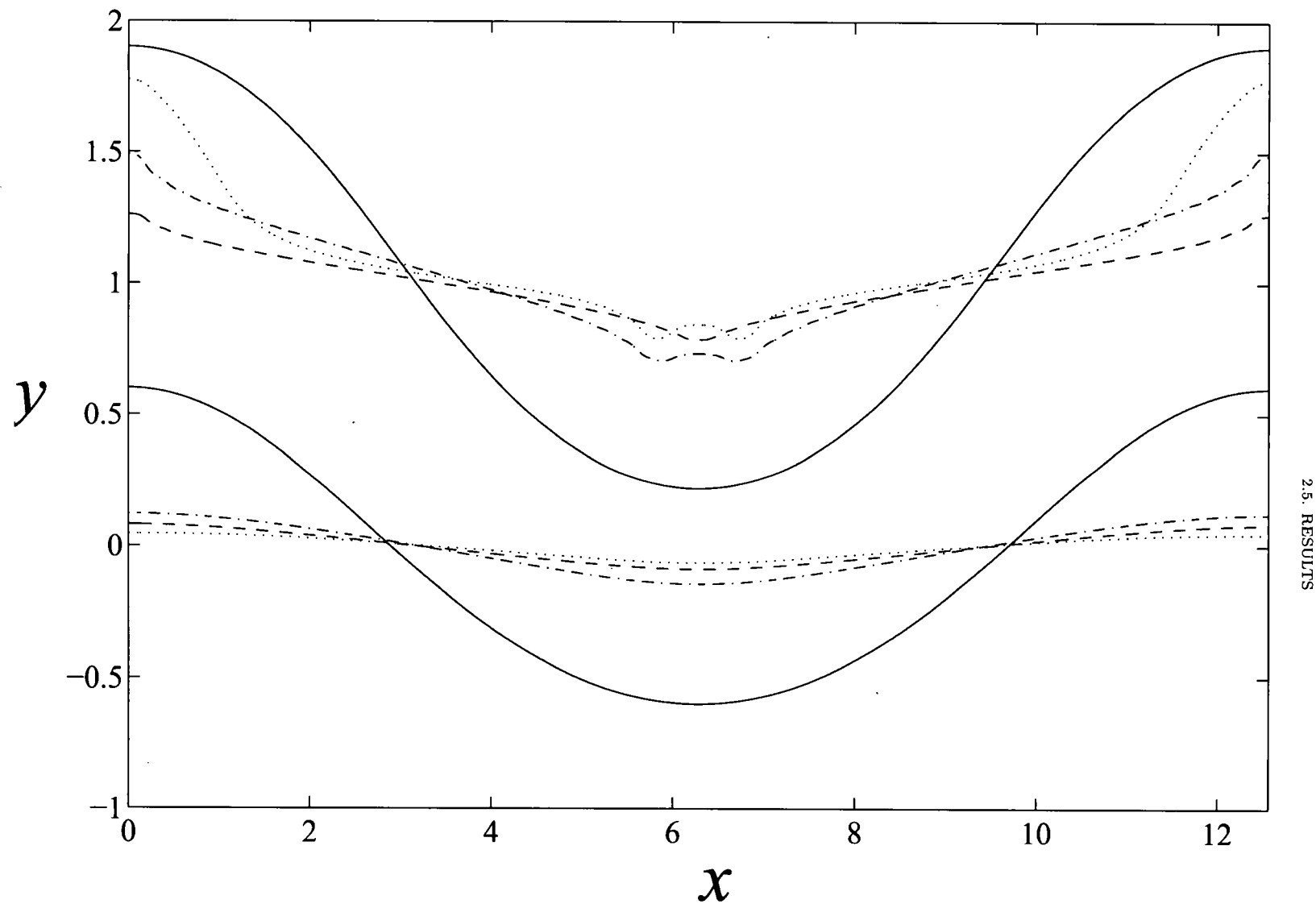


FIGURE 2.5. Four interfacial profiles for the in-phase case with positive Froude number at $k = 0.5$. The solutions shown are $(\mathcal{A}_L, F_3) = (0.601, 0.167)$ (solid lines), $(\mathcal{A}_L, F_3) = (0.0844, 0.232)$ (dashed lines), $(\mathcal{A}_L, F_3) = (0.133, 0.243)$ (dotted lines) and $(\mathcal{A}_L, F_3) = (0.0547, 0.371)$ (dash-dot lines).

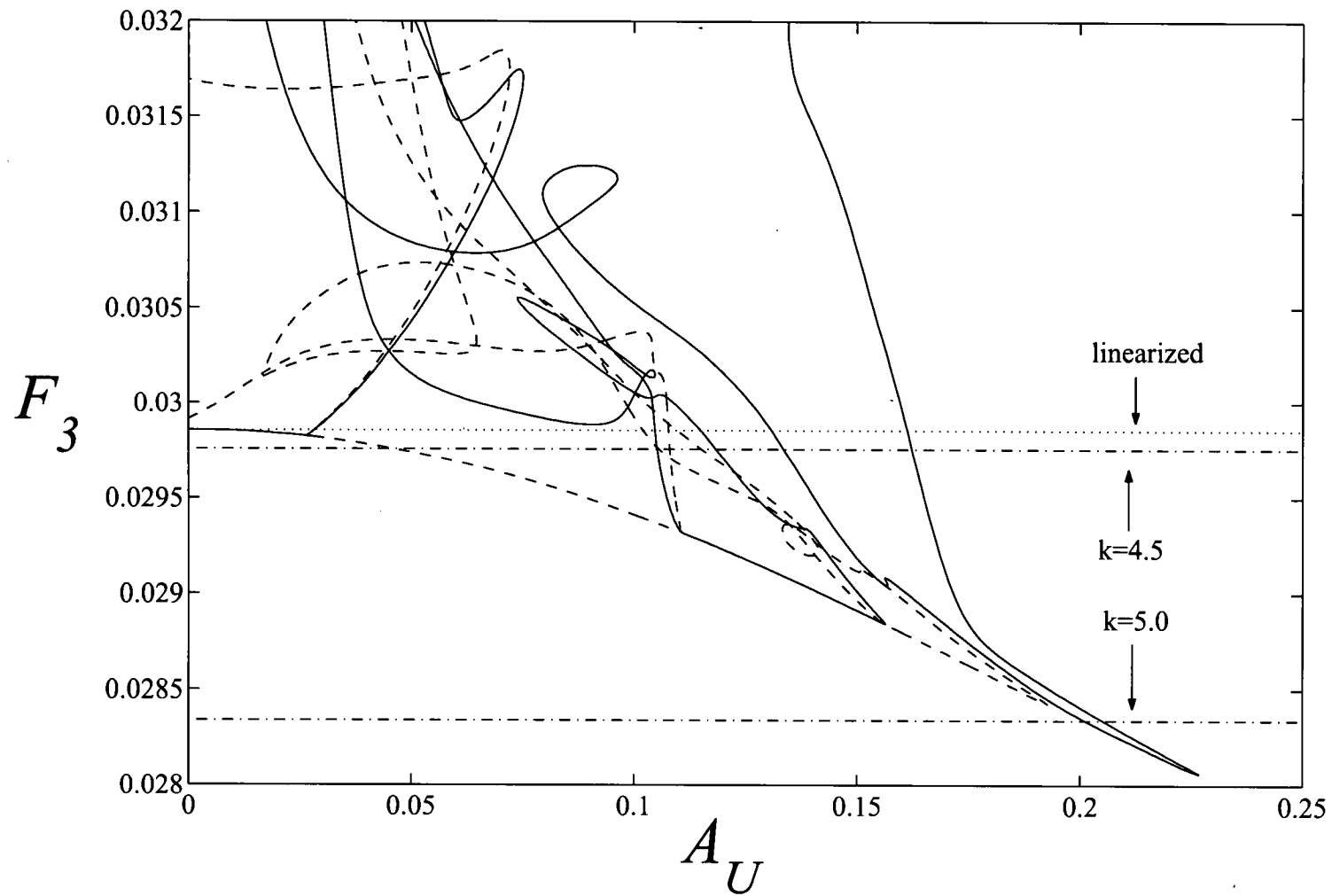


FIGURE 2.6. Dependence of Froude number F_3 on upper wave amplitude A_U for $k = 0.5$, the out-of-phase case with positive Froude number.

agreement with this for small amplitudes, but starts to decrease as amplitude is increased. Here the (\mathcal{A}_U, F_3) curve is made up of a series of disjointed sets of solutions shown alternatively in solid and dashed lines for clarity. Each of these curves contains a section that traces out part of a decrease in lower layer Froude number for increasing amplitude. This acts as a kind of lower bound in (\mathcal{A}_U, F_3) space, with the convoluted (\mathcal{A}_U, F_3) curves which bifurcate off from the branch never crossing below it. In this region both interfacial profiles are nearly sinusoidal.

Above this lower bound the various (\mathcal{A}_U, F_3) curves are quite convoluted with the two variables related in a highly nonlinear fashion. Here the lower interfacial profiles are distinguished by the presence of a superposed wave of shorter wavelength $2\pi/nk$, where n is an integer, on top of the primary wave of wavelength $2\pi/k$. These are a kind of superharmonic ($1:n$) resonance with the secondary mode of solutions which are allowed at the same Froude number. This is confirmed by the fact that the tangled nonlinear branches in Figure 2.6 bifurcate from the lower branch at four resonance values. Two of these resonant branches have been traced right back to their intersection with the $\mathcal{A}_U = 0$ axis, showing that there are at least three solutions of infinitesimal upper interface amplitude, only one of which is a linearized solution. At both these points the lower interface is of moderate amplitude.

Three of these superharmonic type solutions have been tracked exhaustively (the 1:9, 1:10 and 1:11 cases) and some example wave profiles are shown in figures 2.7–2.9. Two 1:9 resonance solutions of identical Froude number are plotted in figure 2.7; here the solid lines are interfacial profiles for $(\mathcal{A}_U, F_3) = (0.0644, 0.310)$ while the dashed lines are solutions for $(\mathcal{A}_U, F_3) = (0.0629, 0.310)$. Figure 2.8 shows two 1:10 resonance solutions, again of similar Froude number, with the solid lines being the solutions for $(\mathcal{A}_U, F_3) = (0.104, 0.303)$ and the dashed lines the profiles for $(\mathcal{A}_U, F_3) = (0.0946, 0.303)$. The final class of superharmonic solutions which were able to be computed accurately were 1:11 resonances. The solid lines in figure 2.9 are the waves profiles for $(\mathcal{A}_U, F_3) = (0.109, 0.300)$, while the dashed lines are profiles for $(\mathcal{A}_U, F_3) = (0.0980, 0.300)$. In each of these cases the shorter

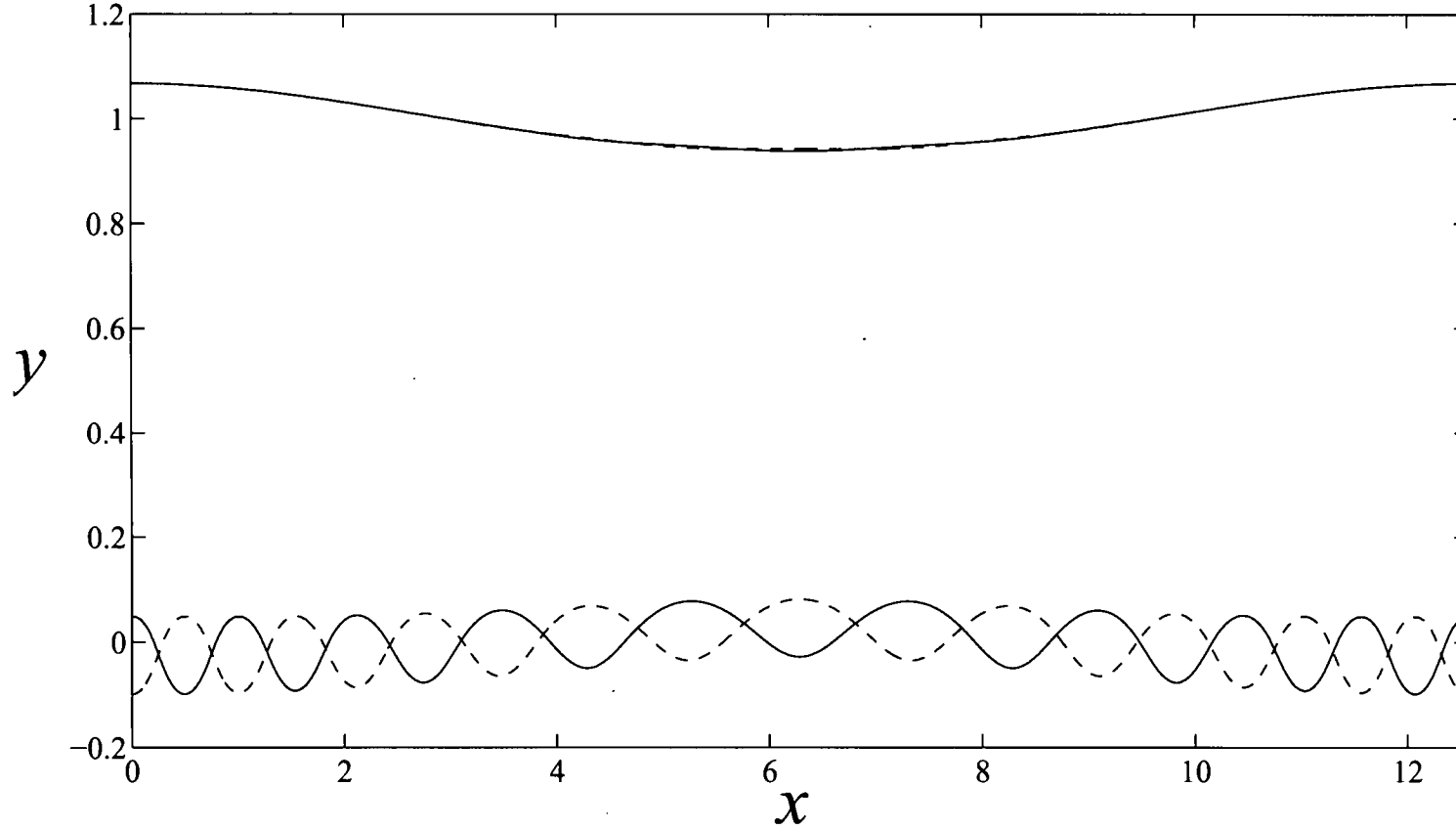


FIGURE 2.7. Two interfacial profiles for the 1:9 resonance at equal lower layer Froude number. The short wavelength mode is out of phase with the primary wave for the solution at $(\mathcal{A}_U, F_3) = (0.0644, 0.310)$ (solid lines) and in phase for the solution at $(\mathcal{A}_U, F_3) = (0.0629, 0.310)$ (dashed lines)

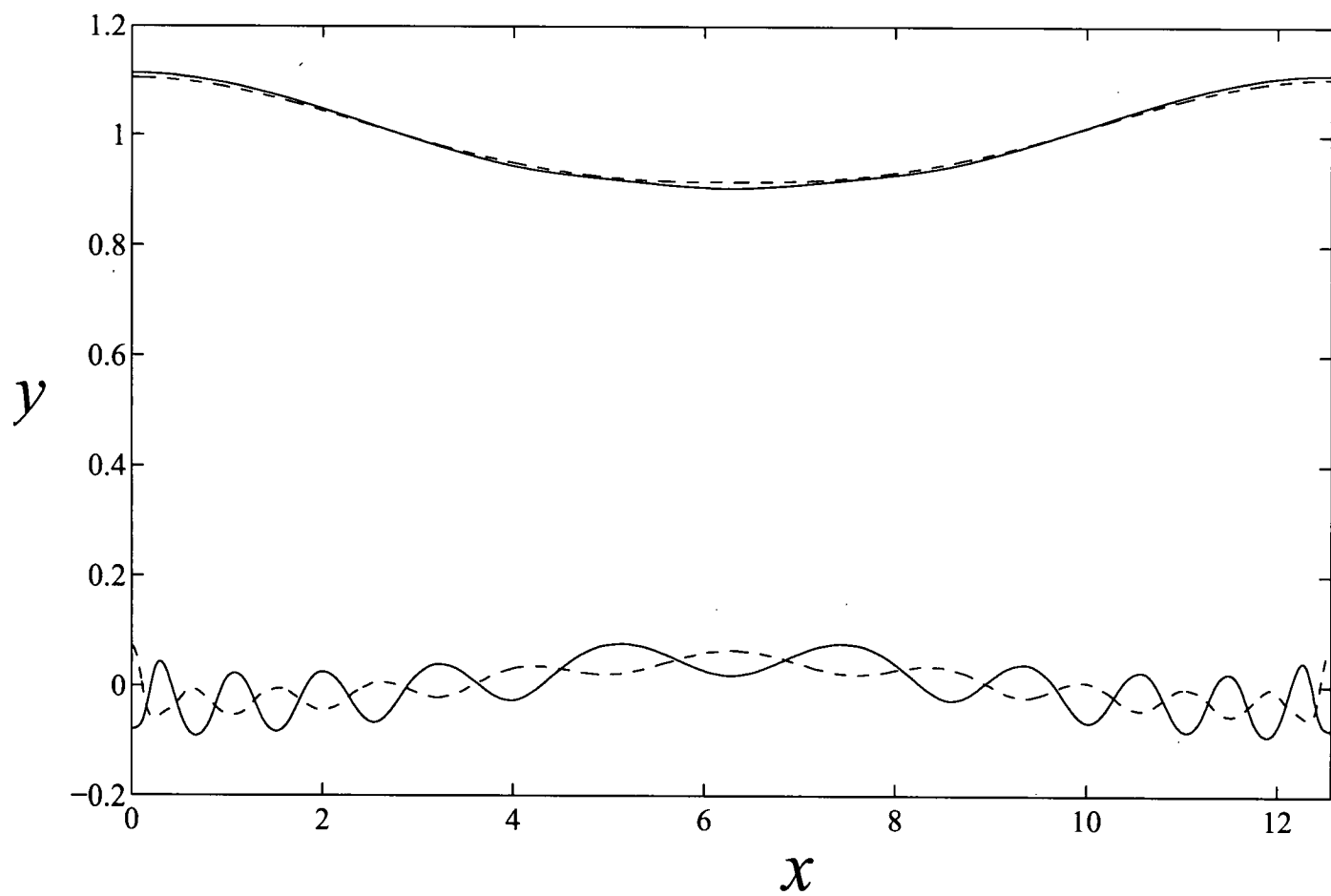


FIGURE 2.8. Two interfacial profiles for the 1:10 resonance at equal lower layer Froude number. The short wavelength mode is in phase with the primary wave for the solution at $(\mathcal{A}_U, F_3) = (0.104, 0.303)$ (solid lines) and out of phase for the solution at $(\mathcal{A}_U, F_3) = (0.0946, 0.303)$ (dashed lines);

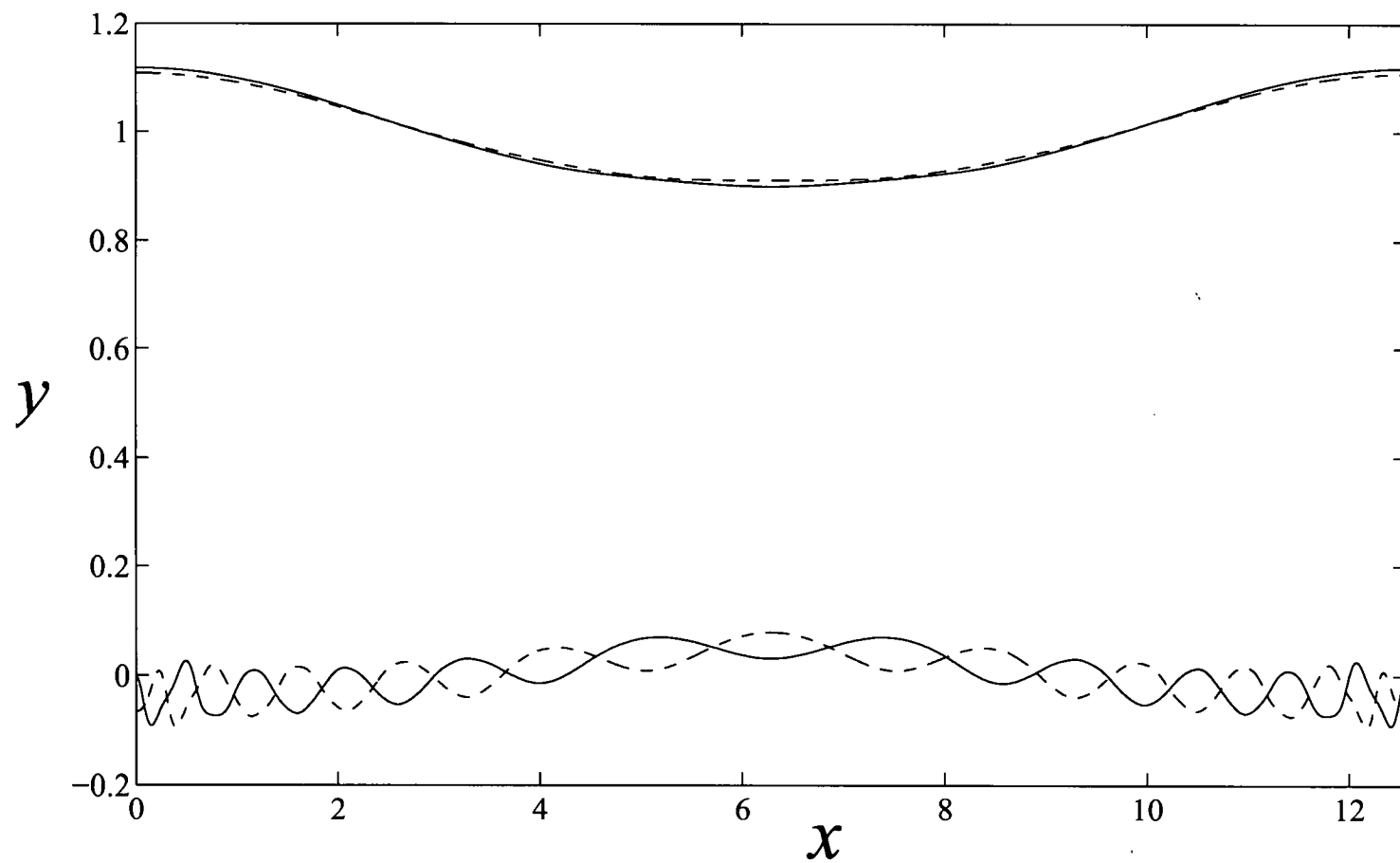


FIGURE 2.9. Two interfacial profiles for the 1:11 resonance at equal Froude number. The short wavelength mode is out of phase with the primary wave for the solution at $(\mathcal{A}_U, F_3) = (0.109, 0.300)$ (solid lines) and in phase for the solution at $(\mathcal{A}_U, F_3) = (0.0980, 0.300)$ (dashed lines).

wavelength component may be superposed either in or out of phase with the primary wave. This corresponds to the two curves which leave the main branch in Figure 2.6 at each of the superharmonic resonance bifurcations. As a consequence each of the disjoint curves in the (\mathcal{A}_U, F_3) -space may contain two types of superharmonic solution. For instance, the first dotted line in figure 2.6 begins with an out-of-phase 1:9 type solution, progresses until the short wavelength component disappears with an in-phase 1:10 resonance being excited at a slightly larger amplitude.

The linearized solutions for $9k = 4.5$ and $10k = 5$ near the appropriate Froude number are shown in Figure 2.6 as horizontal dashed lines. It may be seen that in each case the superharmonic is excited at a larger Froude number than linear theory suggests is possible. Indeed it appears that the larger the amplitude of the primary wave, the further from the linearized solution a superharmonic is first available.

The third linearized solution at this wavelength is an in-phase exchange flow with $F_3 = -0.1567$ and $\alpha = 0.7555$, shown with the horizontal dotted line in figure 2.10. Again the nonlinear solution (the solid and dashed lines in figure 2.10) is found to be in strong agreement for small amplitudes. As amplitude is increased, Froude number F_3 becomes more strongly negative, with the two interfaces taking a slightly pointed nonlinear wave shape, the lower profile having a larger amplitude than the upper.

At a moderate amplitude, about $\mathcal{A}_L = 0.3$, a 1:4 resonant interaction is excited and Froude number begins to increase. Here the secondary wave is larger on the upper interface and out of phase with the primary wave. As the (\mathcal{A}_L, F_3) curve (the solid line in Figure 2.10) is followed, the secondary wave becomes of moderate amplitude itself. Some solutions of this type are shown in figure 2.11, with the superposed wave itself clearly having a nonlinear shape with sharp troughs. The four wave profiles in Figure 2.11 are all of amplitude $\mathcal{A}_L = 0.32$ with the solid lines corresponding to the profiles at $(\mathcal{A}_L, F_3) = (0.32, -0.1614)$, the dashed lines are the profiles for $(\mathcal{A}_L, F_3) = (0.32, -0.1620)$, the solution at $(\mathcal{A}_L, F_3) = (0.32, -0.1612)$

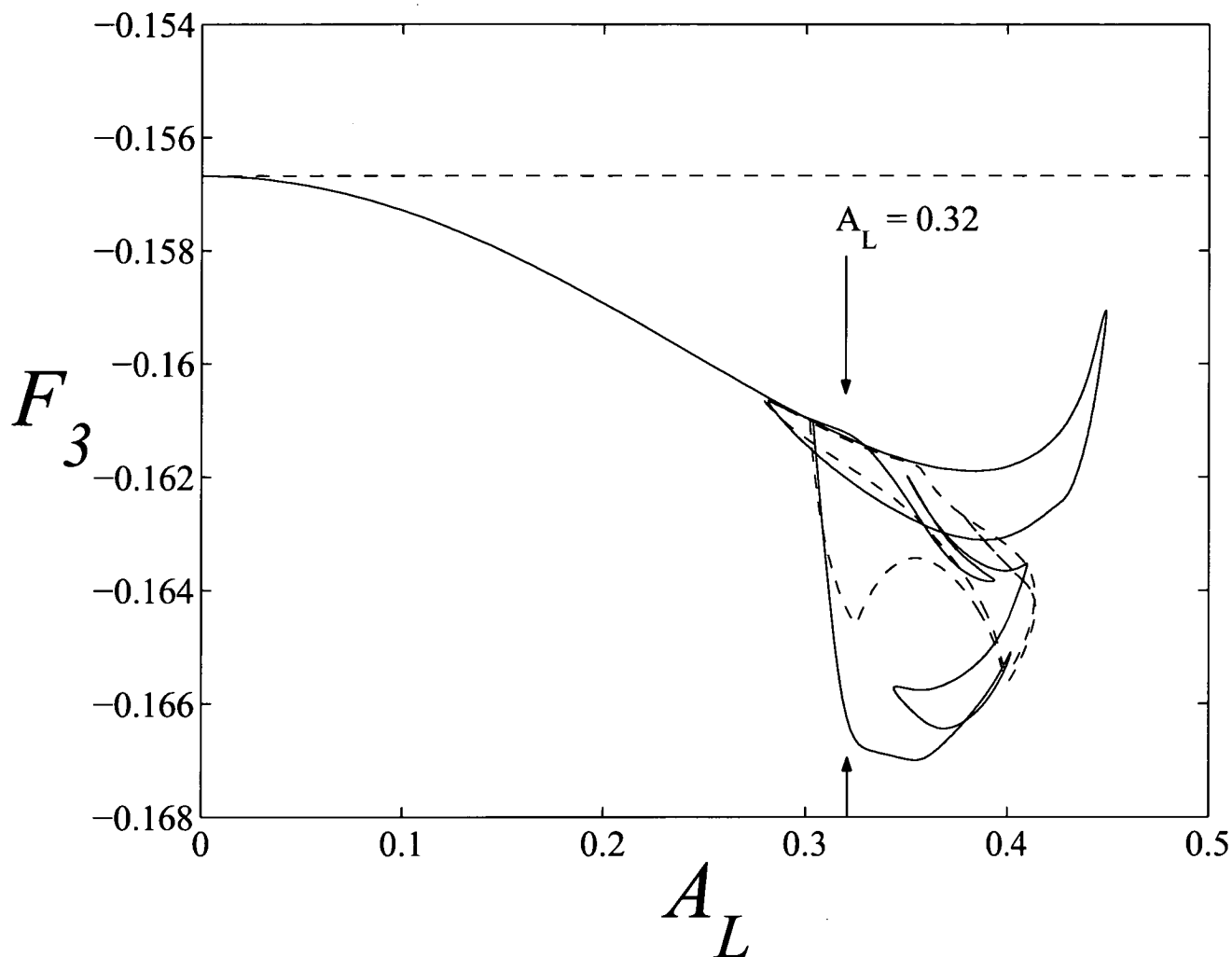


FIGURE 2.10. Dependence of Froude number F_3 on lower wave amplitude A_L for $k = 0.5$, the in-phase case with negative Froude number.

is represented by the dash-dot lines and the dotted lines are the waves profiles for $(A_L, F_3) = (0.32, -0.1662)$.

The class of solution with an in-phase secondary wave is not as readily available here as in the previous case. For these to be computed an initial guess in Newton's method was created, somewhat artificially, by taking an out-of-phase solution and multiplying the coefficients B_4, C_4, D_4, \dots by -1 . Having done this the solutions of the type shown in figure 2.12 were obtained, with the secondary wave of opposite

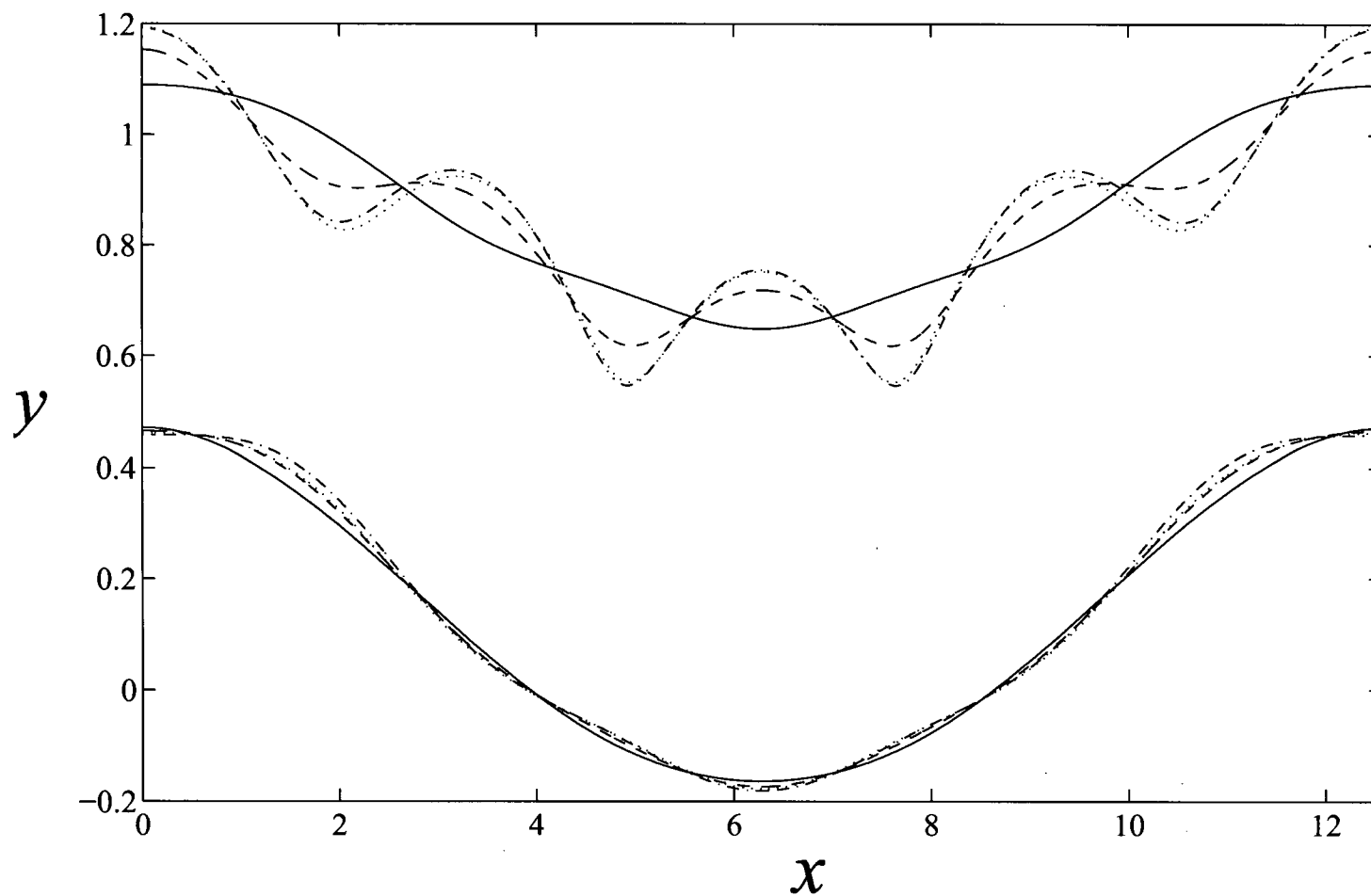


FIGURE 2.11. Four interfacial profiles for $\mathcal{A}_L = 0.32$ with a 1:4 resonance in phase with the primary solution mode. The profiles shown are for $(\mathcal{A}_L, F_3) = (0.32, -0.1614)$ (solid lines), $(\mathcal{A}_L, F_3) = (0.32, -0.1620)$ (dashed lines), $(\mathcal{A}_L, F_3) = (0.32, -0.1612)$ (dash-dot lines) and $(\mathcal{A}_L, F_3) = (0.32, -0.1662)$ (dotted lines).

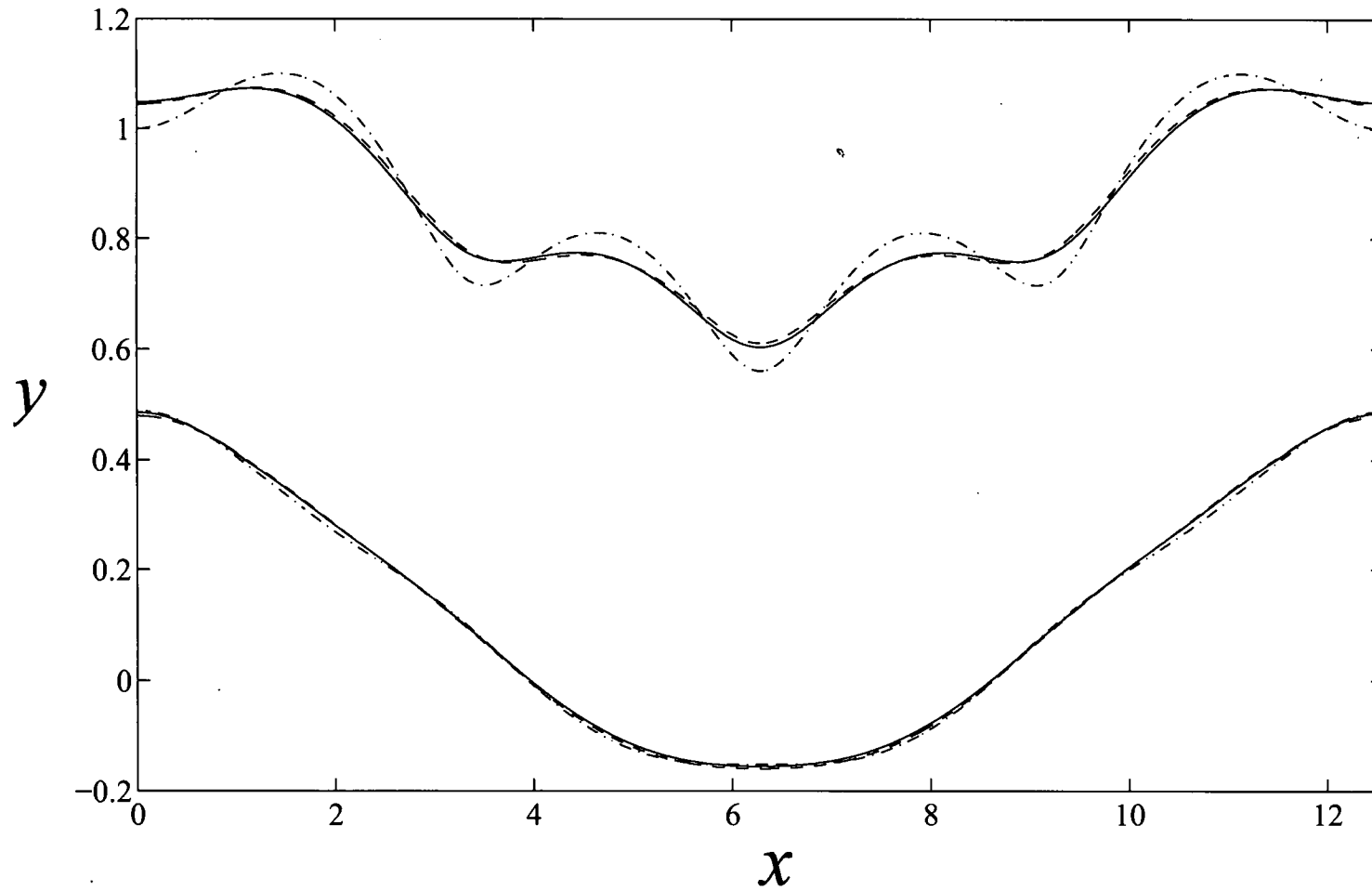


FIGURE 2.12. Three interfacial profiles for $\mathcal{A}_L = 0.32$ with a 1:4 resonance out of phase with the primary solution mode. The profiles shown are for $(\mathcal{A}_L, F_3) = (0.32, -0.1643)$ (solid lines), $(\mathcal{A}_L, F_3) = (0.32, -0.1617)$ (dashed lines) and $(\mathcal{A}_L, F_3) = (0.32, -0.1613)$ (dash-dot lines).

phase to the solutions of figure 2.11. These were tracked for some distance in the parameter space, as seen in the dotted line on the (\mathcal{A}_L, F_3) diagram in Figure 2.10. Three interfacial profiles are shown in Figure 2.12 with solid lines corresponding to the solution at $(\mathcal{A}_L, F_3) = (0.32, -0.1643)$, the dashed lines are the solutions for $(\mathcal{A}_L, F_3) = (0.32, -0.1617)$ and the dash-dot lines represent the profiles for $(\mathcal{A}_L, F_3) = (0.32, -0.1613)$.

It may be seen that up to 12 distinct solutions may be obtained for some values of \mathcal{A}_L , such as in the highly tangled region near $\mathcal{A}_L = 0.375$. A slightly simpler situation is represented by the seven simultaneous solutions available at the same value $\mathcal{A}_L = 0.32$ of the amplitude, as shown in figures 2.11 and 2.12. The complexity of the solution space is further emphasised by noting that the proximity of two solutions on the (\mathcal{A}_L, F_3) diagram is not an indication that their interfacial profiles are qualitatively similar. Yet another feature of these cases is the many sections of the Froude number-amplitude diagram in Figure 2.10 which run nearly parallel to each other. In terms of the interfacial profiles these correspond to a situation where the primary wave's amplitude decreases as the secondary wave's increases, or vice versa. The situation for the in-phase solutions near $\mathcal{A}_L = 0.4$ is an example of this. Such an occurrence seems in line with conventional thinking about the role of energy transfer between solution modes in these sorts of resonant interactions (Phillips [46]). Both classes of solutions terminate by crossing back onto a previously calculated solution (in both cases at $\mathcal{A}_L \approx 0.3$), thus forming a complicated kind of loop structure.

2.5.2. Results for $k = 1$. Wavenumber will now be fixed at $k = 1$, a value chosen with a view to obtaining further nonlinear resonance effects. The linearized solution (as shown in figure 2.2) indicates that such effects may be possible for two speeds at this wavenumber, namely the exchange flows at $F_3 \approx -0.08$ and $F_3 \approx -0.04$.

The first set of results to be discussed in this section is for the slower exchange flow, emerging from the linearized solution at $F_3 \approx -0.04$. For small amplitudes

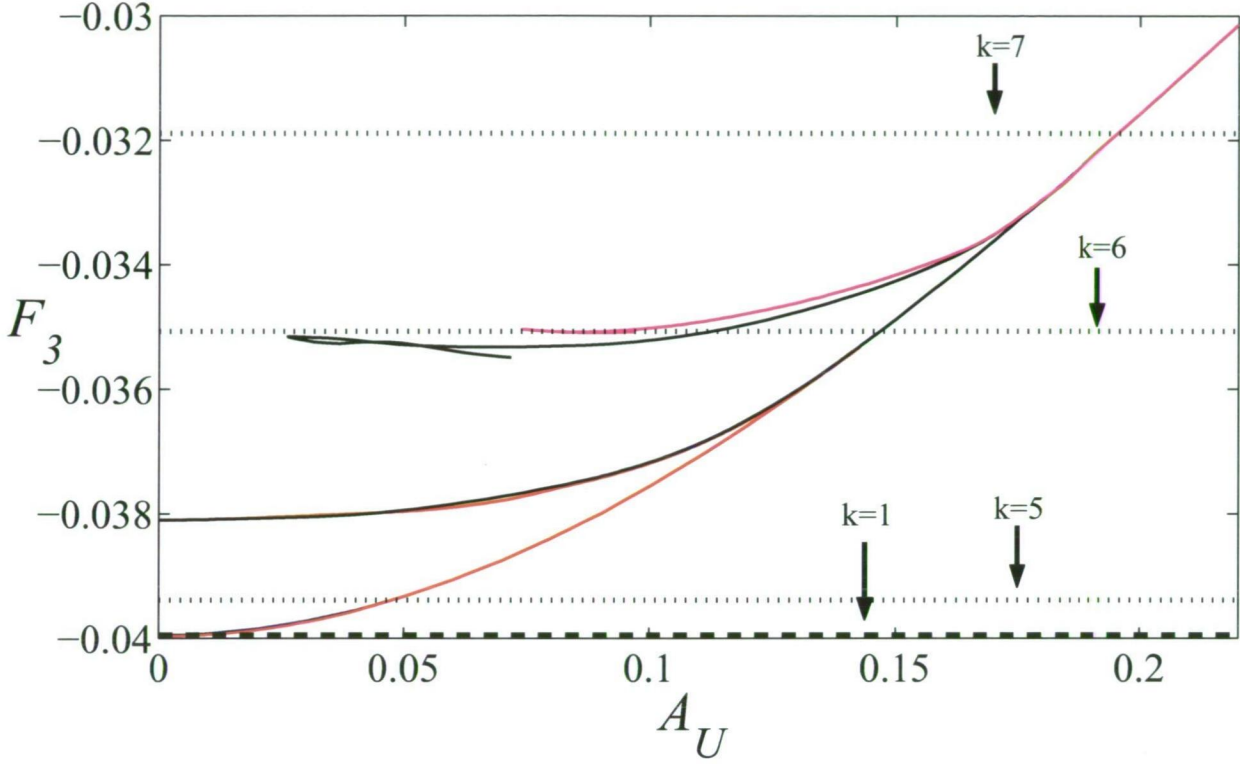


FIGURE 2.13. Dependence of lower layer Froude number F_3 on upper wave amplitude A_U for the slower speed case at $k = 1$.

this agrees very closely with the linearized solution and, as predicted, the interfaces are in phase. The relationship between the parameters F_3 and A_U is presented in figure 2.13. Here the linearized solution is represented by a horizontal dashed line, with the series of multi-coloured solid lines representing various disjoint nonlinear solutions. Each of these solutions has a portion which traces out an increase in Froude number with increasing amplitude. In addition to this, at several points a pair of solutions bifurcates away from this main branch and continues through (A_U, F_3) -space. These extra solutions display nonlinear resonant effects. The first set (bifurcating from $(A_U, F_3) = (0.0462, -0.0394)$) is a 1 : 5 resonance which continues very close to the main branch, right back to $A_U = 0$ and beyond. These solutions have five ripples on the lower interface, that is, a superposed wave of

shorter wavelength. This shorter wavelength component may be either in or out of phase with the primary component; hence the two branches.

The interfacial profiles for $\mathcal{A}_U = 0.025$ are shown in figure 2.14. Shown as a dotted line is the linearized solution for $k = 5$ in figure 2.13; this is the solution mode that interacts with the primary component of the wave to produce the resonance. Similarly the linearized solution for $k = 6$ and $k = 7$ are shown as dotted lines in figure 2.13, with the solutions which bifurcate away these values of F_3 displaying 1 : 6 and 1 : 7 resonances, respectively. Many interfacial profiles have been computed along these solutions branches, but are not presented here in the interests of space; they typically possess many small waves on the lower interface (as in figure 2.14). Each of these resonant effects is excited at a slightly faster speed than the linearized value of Froude number might suggest.

The second set of solutions at this wavenumber emerges from the linearized solution at $F_3 \approx -0.08$. Again, at small amplitudes the nonlinear solutions agree closely with the linearized predictions. As amplitude is increased, the lower layer Froude number decreases until an amplitude of about $\mathcal{A}_U \approx 0.22$. Figure 2.15 shows the relationship between lower fluid speed F_3 and wave amplitude \mathcal{A}_U for these two branches of solutions. The shapes of these solution branches were found to be independent of the numerical parameters, and indicate the complex effects of non-linearity.

The solution profiles corresponding to the large crosses in figure 2.15 are shown in figure 2.16. A 1 : 2 resonance develops at around $\mathcal{A}_U = 0.17$ (just after the first of the profiles shown) and persists through the solution space. As the solutions progress along this curve, the shorter wavelength component itself becomes of moderate amplitude and at least some of the fine structure in the (\mathcal{A}_U, F_3) curve of figure 2.15 may be attributed to this. There is a second set of solutions (shown with a blue line) where the short wavelength component has been superposed with opposite phase to the solutions on the other branch. These may be traced right back to zero amplitude, giving a second small amplitude solution, while convergent

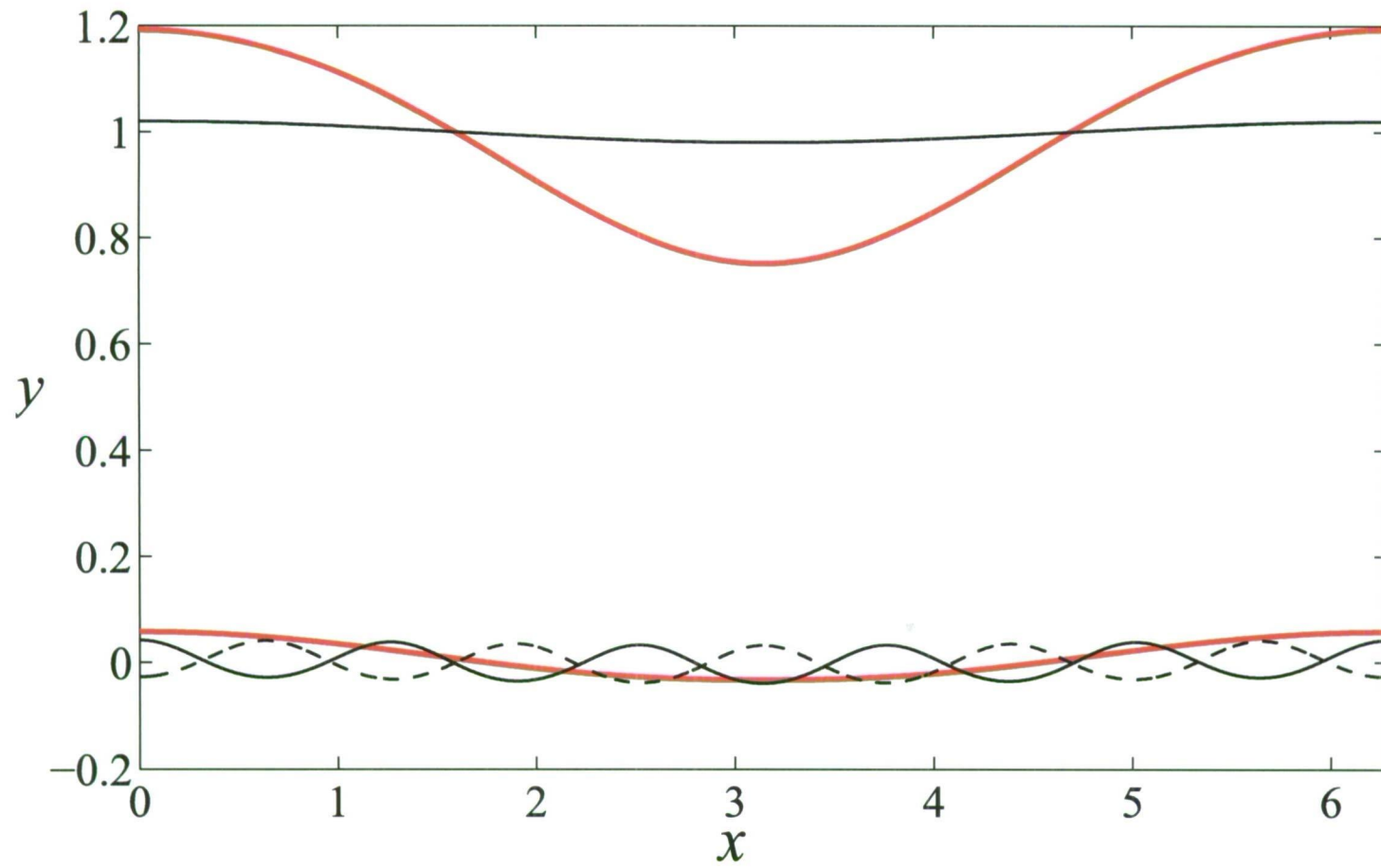


FIGURE 2.14. Three interfacial profiles for the slower speed case. The red lines are wave profiles for $\mathcal{A}_U \approx 0.21$. The solid and dashed black lines display a 1:5 resonance and are for $\mathcal{A}_U \approx 0.025$.

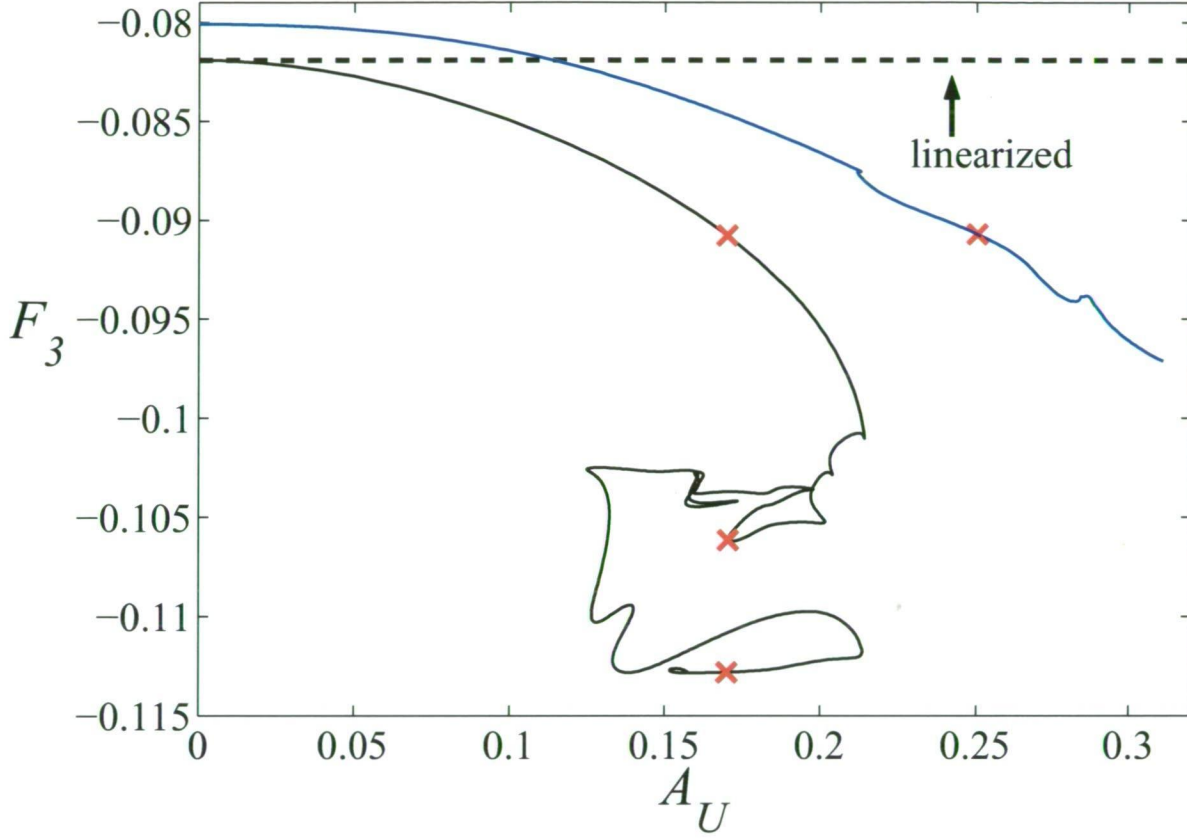


FIGURE 2.15. Dependence of lower layer Froude number F_3 on upper wave amplitude A_U for the faster speed case at $k = 1$.

solutions are unavailable for amplitudes greater than $A_U \approx 0.31$. The lower layer Froude number of the small amplitude solution is near to, but slightly smaller than, the linearized solution for $k = 2$.

2.5.3. Results for $k = 2.5$. For the in-phase solution at this wavelength, linearized theory predicts $F_3 = 0.03925$ with $\alpha = 0.04768$; that is, a lower interface of much larger amplitude than the upper. The nonlinear solutions (shown as a solid line in figure 2.17) agree well with both predictions and we see a similar situation to that of Figure 2.4 (a longer wavelength example from the same mode of solutions). Again, Froude number F_3 increases with amplitude, reaching a maximum at the moderate value $A_L = 0.19$ of the wave amplitude. These solutions are characterised

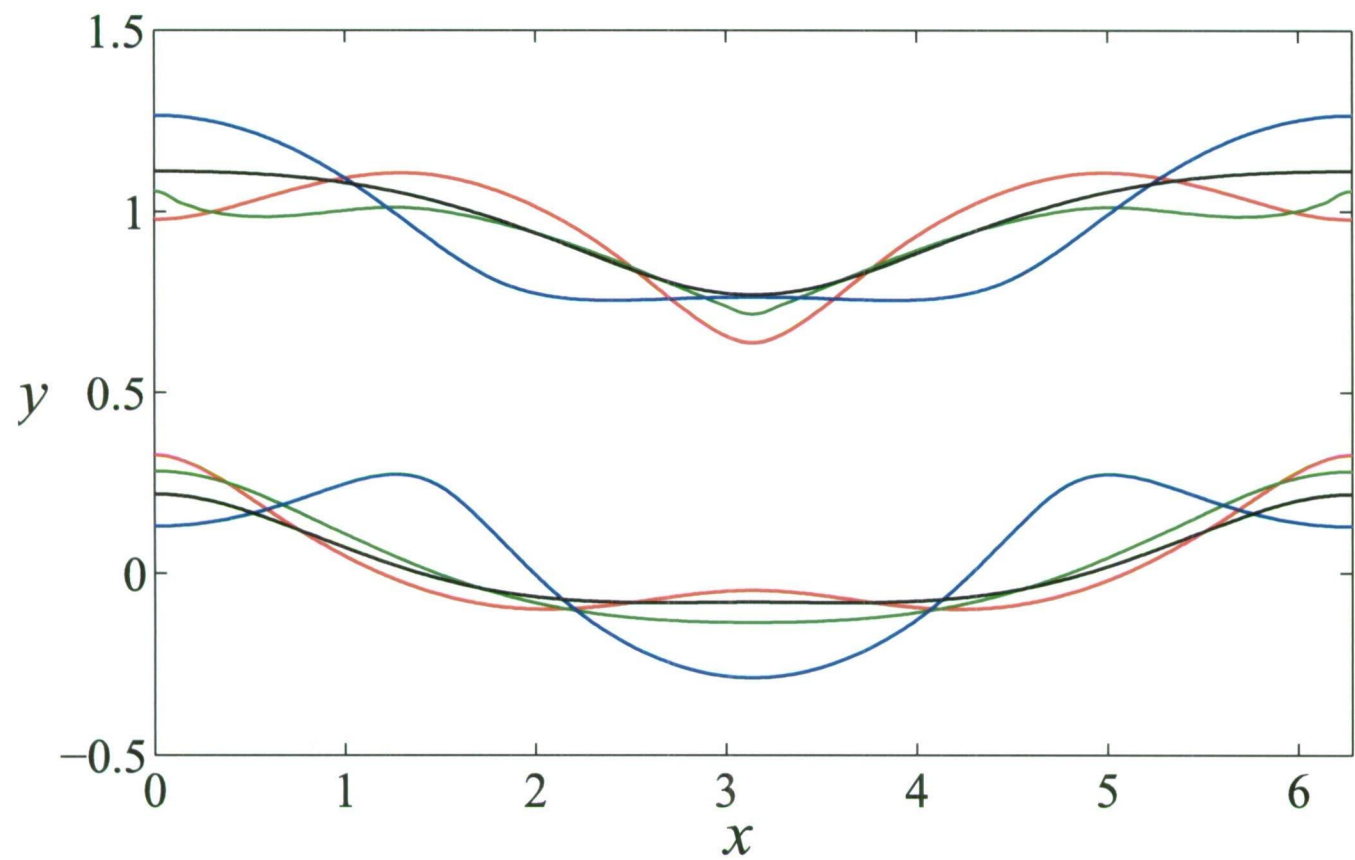


FIGURE 2.16. Four interfacial profiles for the faster speed case. The black, red and green wave profiles are all at an upper wave amplitude of $\mathcal{A}_U \approx 0.17$. The blue profiles are for $\mathcal{A}_U \approx 0.25$. All except the black profiles display a 1:2 resonance.

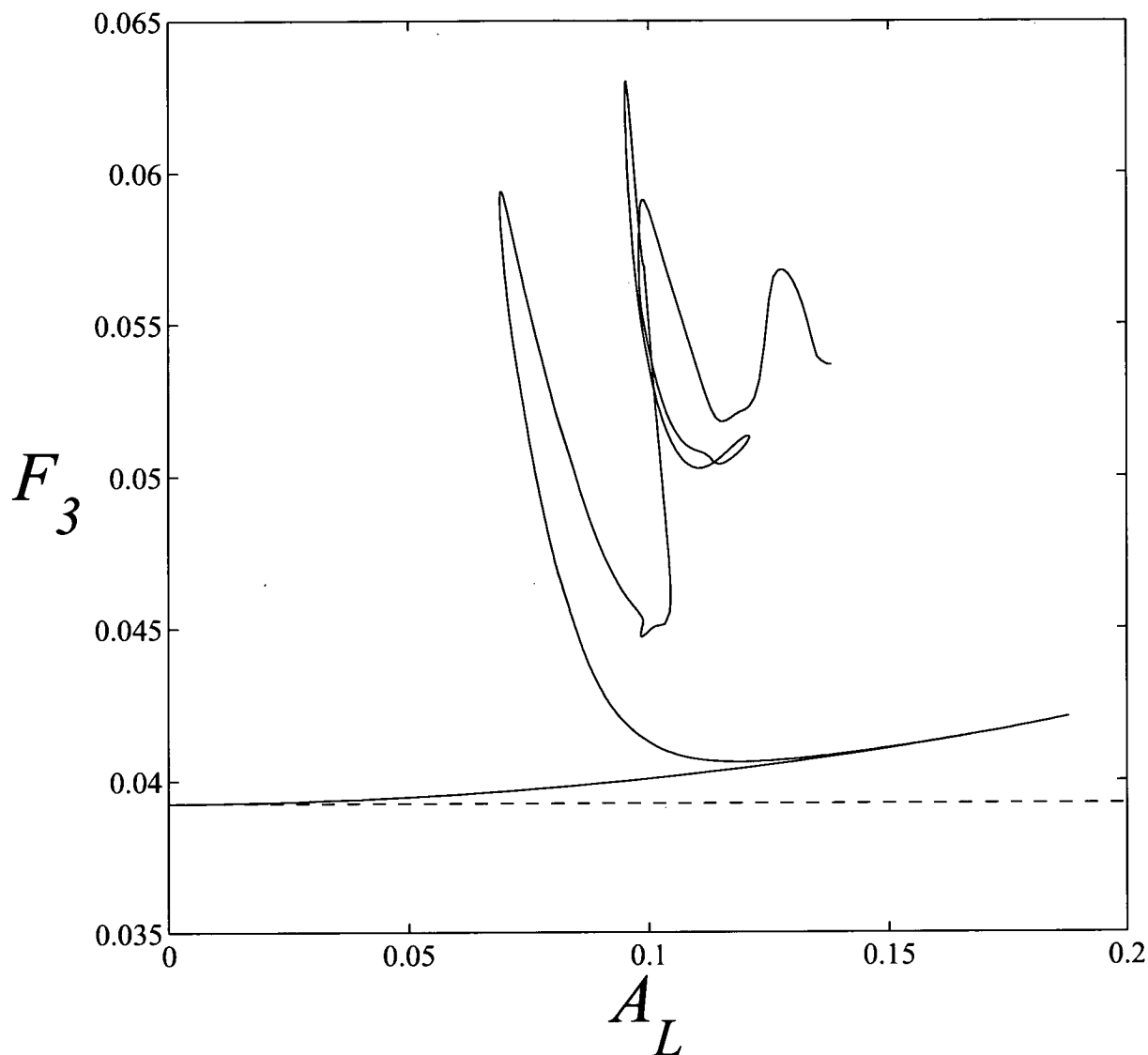


FIGURE 2.17. Dependence of Froude number F_3 on lower wave amplitude A_L for $k = 2.5$, the in-phase case with positive Froude number.

by a nearly flat upper interface and a slightly square lower interface of moderate amplitude.

The (A_L, F_3) curve then turns back on itself and traces out a complicated relationship featuring numerous sharp turning points. As before, the solutions near these points correspond to dimpled waves, several of which are shown in figure

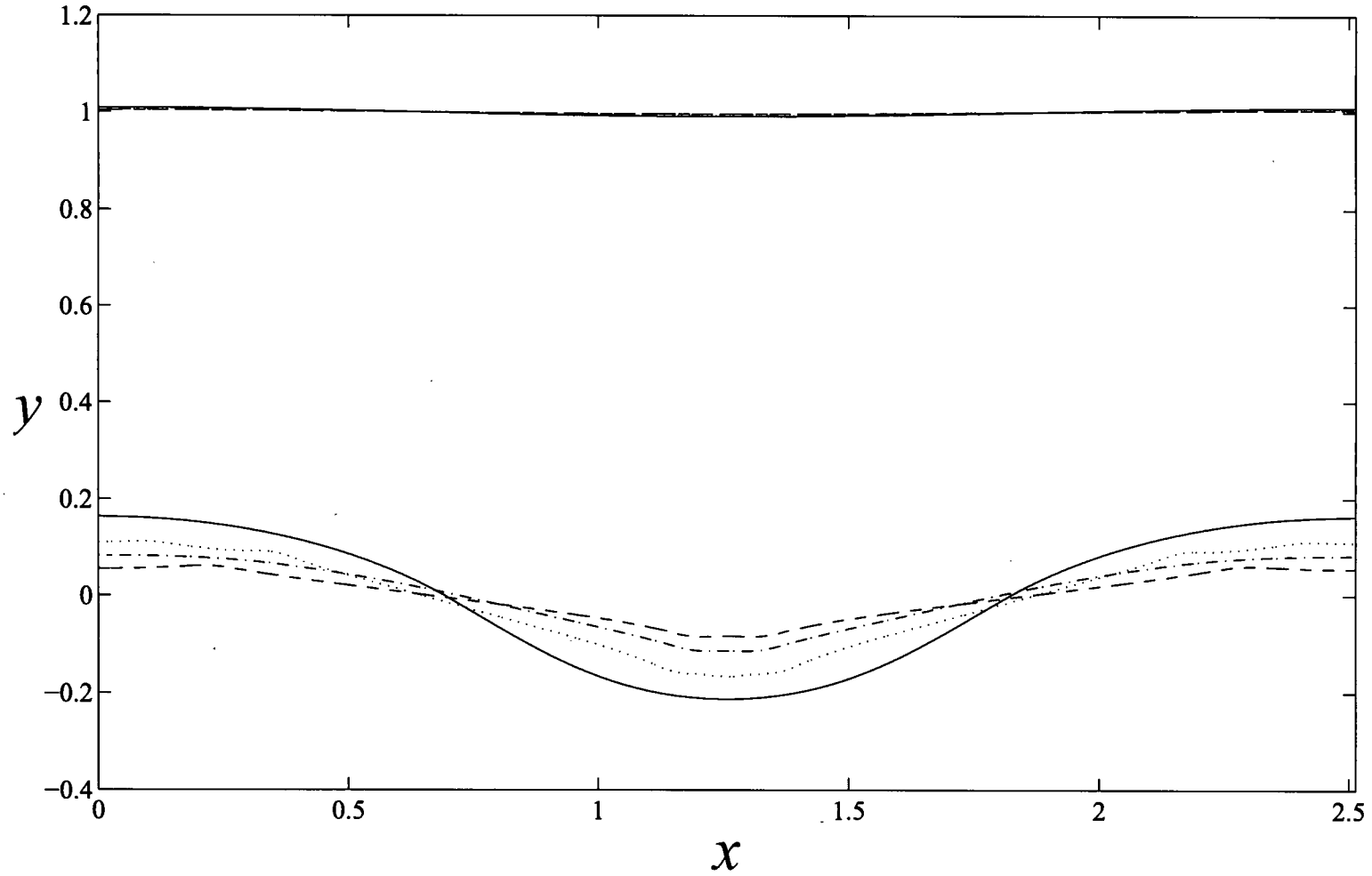


FIGURE 2.18. Four interfacial profiles for the in-phase case with positive Froude number at $k = 2.5$. The profiles shown are for $(\mathcal{A}_L, F_3) = (0.188, 0.0421)$ (solid lines), $(\mathcal{A}_L, F_3) = (0.0693, 0.0594)$ (dashed lines), $(\mathcal{A}_L, F_3) = (0.0986, 0.0447)$ (dash-dot lines) and $(\mathcal{A}_L, F_3) = (0.138, 0.0537)$ (dotted lines).

2.18. The solution of largest amplitude $(\mathcal{A}_L, F_3) = (0.188, 0.0421)$ is shown with a solid line, two moderate amplitude solutions at $(\mathcal{A}_L, F_3) = (0.0693, 0.0594)$ and $(\mathcal{A}_L, F_3) = (0.0986, 0.0447)$ are shown with dashed and dash-dot lines, respectively. The last computed solution, at $(\mathcal{A}_L, F_3) = (0.138, 0.0537)$ and shown in Figure 2.18 with dotted lines, represents the point at which our numerical method failed to continue the branch shown in Figure 2.17. No geometric limitation is obvious from these results, but it is possible that some subtle structure may be formed in the interface profiles that prevents the numerical method from continuing further.

Linear theory predicts two out-of-phase solutions at this wavelength, one at $F_3 = -0.064414$ with a large lower interface ($\alpha = -0.1126$) and another at $F_3 = -0.29616$ with a large upper interface ($\alpha = -25.8476$). Both of these are shown with horizontal dashed lines in figure 2.19. The solid lines in Figure 2.19 are nonlinear solutions obtained with $N = 51$. The two solution branches are evidently not connected in (\mathcal{A}_U, F_3) parameter space. Both sets of nonlinear solutions agree well with linear theory at small amplitudes, and this predicts that the relative amplitudes of the two interfaces in each case will be quite different. Again we see monotonic variation in Froude number as amplitude is increased, up to some maximum before the (\mathcal{A}_U, F_3) curves turn back on themselves and then progress in a complicated fashion.

Solutions on the curve originating from the higher speed exchange flow are shown in figure 2.20. These four curves correspond to the interfacial profiles for $(\mathcal{A}_U, F_3) = (0.1388, -0.2591)$, shown with solid lines, the dashed lines are the solution for $(\mathcal{A}_U, F_3) = (0.05704, -0.07093)$, the solution for $(\mathcal{A}_U, F_3) = (0.6327, -0.1267)$ is shown by dash-dot lines and the dotted lines represent the profiles for $(\mathcal{A}_U, F_3) = (0.1053, -0.2154)$.

These solutions have upper interfaces of much larger amplitude than their lower interfaces at smaller amplitude \mathcal{A}_U . As the solutions are tracked, the interfaces become of comparable amplitude. In particular, the lower interface develops dimple like features at its trough and crest, as well as increasing in mean height. The upper

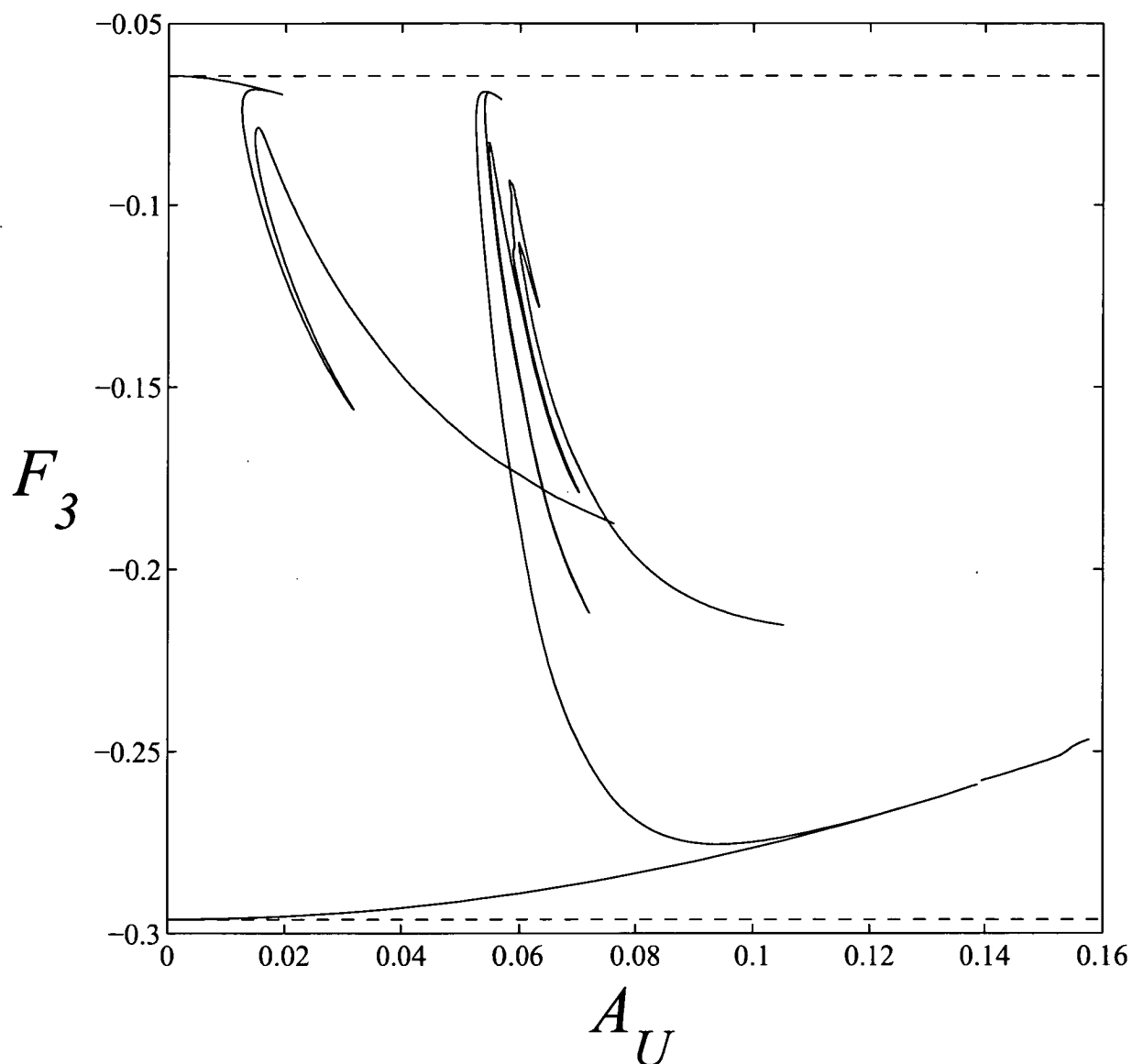


FIGURE 2.19. Dependence of Froude number F_3 on upper wave amplitude A_U for $k = 2.5$, both the out-of-phase cases with negative Froude number.

interface, however, remains approximately sinusoidal. It is possible that the dotted profile for $(A_U, F_3) = (0.1053, -0.2154)$ is close to a limiting solution with an overhanging structure at the crest of the lower interfacial wave, since near vertical portions are present in the computed profile.

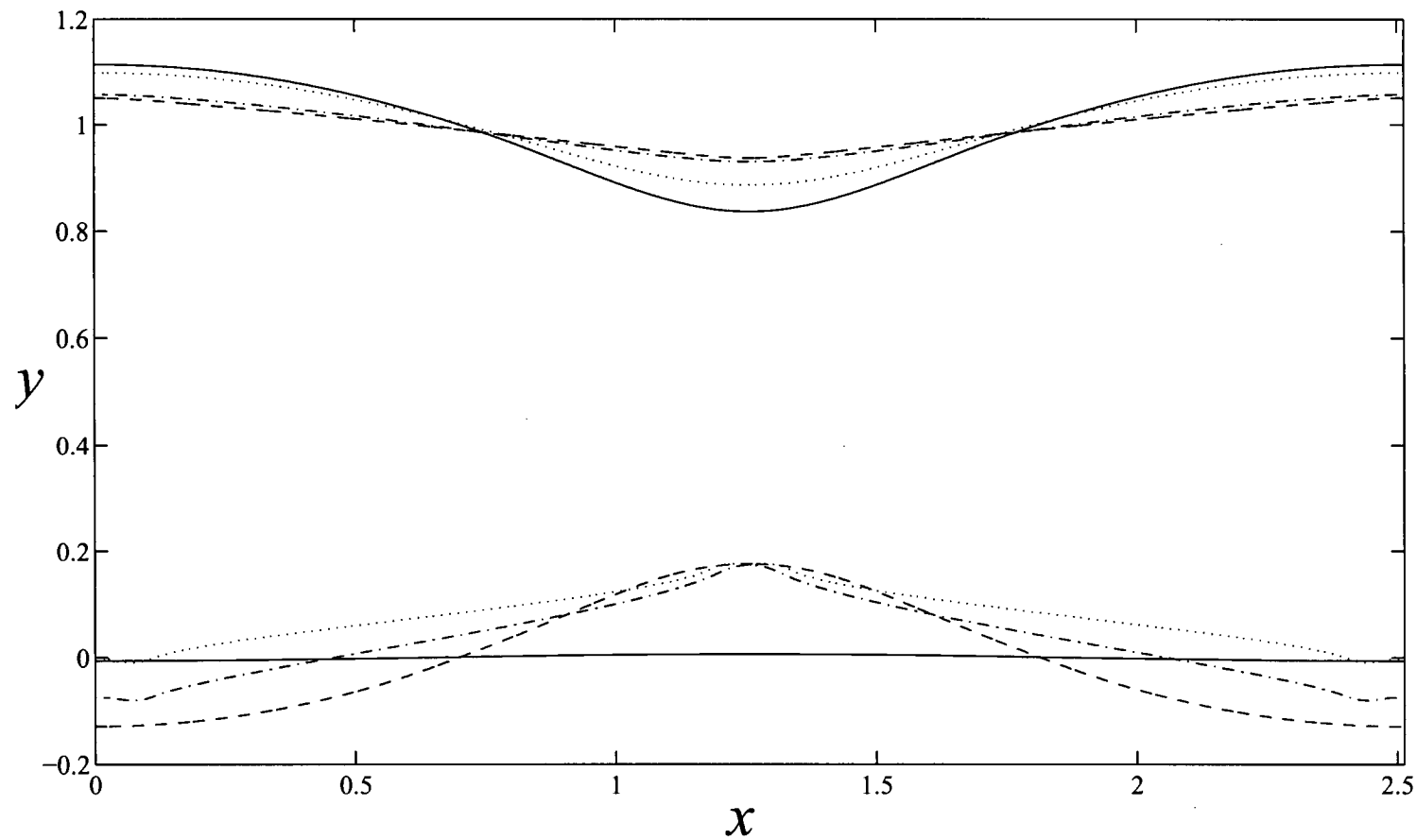


FIGURE 2.20. Four interfacial profiles originating from out-of-phase case with large negative Froude number at $k = 2.5$. The profiles shown are for $(\mathcal{A}_U, F_3) = (0.1388, -0.2591)$ (solid lines), $(\mathcal{A}_U, F_3) = (0.05704, -0.07093)$ (dashed lines), $(\mathcal{A}_U, F_3) = (0.6327, -0.1267)$ (dash-dot lines) and $(\mathcal{A}_U, F_3) = (0.1053, -0.2154)$ (dotted lines).

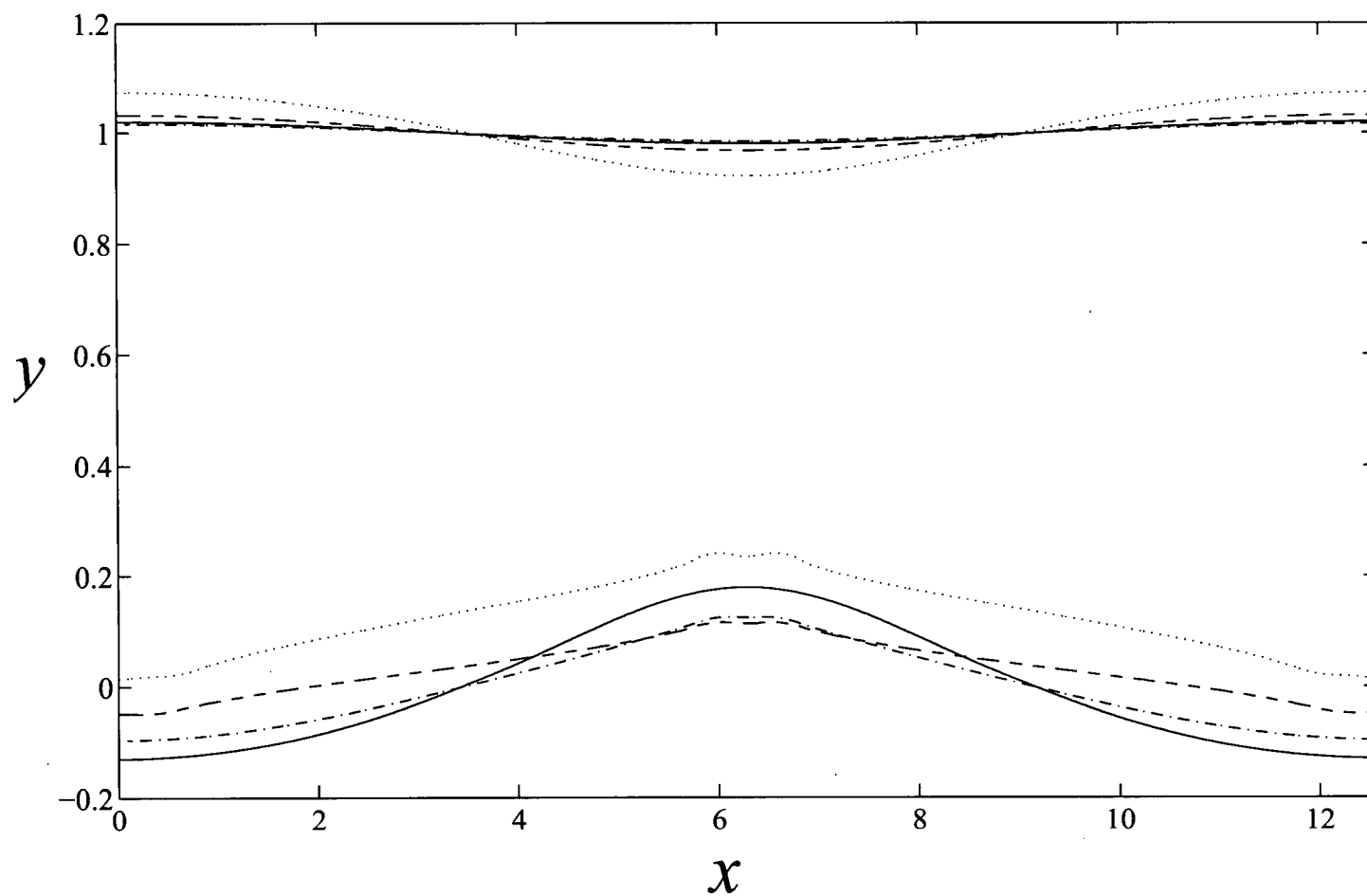


FIGURE 2.21. Four interfacial profiles originating from out-of-phase case with small negative Froude number at $k = 2.5$. The profiles shown are for $(\mathcal{A}_U, F_3) = (0.01951, -0.06958)$ (solid lines), $(\mathcal{A}_U, F_3) = (0.03172, -0.1562)$ (dashed lines), $(\mathcal{A}_U, F_3) = (0.01534, -0.07866)$ (dash-dot lines) and $(\mathcal{A}_U, F_3) = (0.07627, -0.1875)$ (dotted lines).

The case originating from the slower exchange flow displays a similar pattern of behaviour. Some example solutions may be seen in figure 2.21. The profiles shown with solid lines are for the parameters values $(\mathcal{A}_U, F_3) = (0.01951, -0.06958)$, the dashed lines show the solution for $(\mathcal{A}_U, F_3) = (0.03172, -0.1562)$, the solution for $(\mathcal{A}_U, F_3) = (0.01534, -0.07866)$ is shown with dash-dot lines and the dotted lines are the profiles for $(\mathcal{A}_U, F_3) = (0.07627, -0.1875)$.

Here the interfacial profiles possess a larger amplitude lower interface for small to moderate amplitudes. Past the first sharp feature on the (\mathcal{A}_U, F_3) curve in Figure 2.19 the two interfaces eventually become of similar amplitude. These solutions are qualitatively similar to those calculated for the fast exchange flow, with lumps at their peaks and troughs. Indeed, the last computed solutions from the two (\mathcal{A}_U, F_3) curves closely resemble each other, both having a lower interface which displays lumps as well as a significant positive mean displacement.

Notice that there is, in fact, a second small disjoint branch of solutions in (\mathcal{A}_U, F_3) parameter space just beyond $\mathcal{A}_U = 0.14$. This is shown in Figure 2.19. It may represent a remnant of a subharmonic solution which is not able to be continued accurately numerically here beyond the small portion shown.

2.6. Discussion and conclusion

This chapter has presented a wide array of nonlinear solutions to the problem of steady periodic waves on an intrusion layer with constant vorticity. These were seen to agree well with the predictions of linear theory for small amplitudes, with nonlinear effects leading to some highly irregular behaviour for moderate and large amplitudes. Small amplitude solutions which did not coincide with the linearized solution were also present. The numerical scheme used was a straightforward extension to that of Michallet and Dias [41] and Forbes et al. [27], with a reparametrization of the problem using arc-length to allow for the possibility of overhanging waves. Although no such waves were computed, the possibility of overhanging limiting profiles was suggested by some of the numerical results. In

addition it is possible that overhanging waves might be encountered for different (and less relevant) values of the physical parameters; their absence does not reveal a limitation of the numerical technique, and in fact such solutions would be subject to Rayleigh-Taylor instability, so that interest in them is somewhat academic. In this chapter, we chose density ratios close to unity to represent a stratified ocean or reservoir, whereas the dramatically overhanging solitary waves computed by Rus  s and Grue [49] were for fluid density ratios (in our notation) of $D_1 = 0.57$ and $D_3 = 1.43$. When this choice of density ratio was used in the present problem no overhanging profiles were obtained, however, suggesting that the profiles of Rus  s and Grue [49] were due (at least in part) to the presence of a horizontal wall in the bottom fluid layer.

It has been assumed here that the shear in the middle layer is exactly the amount required to make the velocity profile in the three fluids continuous, when both interfaces are horizontal. This was done to mimic the expected effects of viscosity. However, as the fluids here are inviscid tangential slip at each interface is possible, and so equation (2.2.3) could be replaced with the more general sheared flow $F_2 = F_3 + \gamma y$, in which the extra parameter γ is left arbitrary. We have made some preliminary investigations of the effect of varying this parameter γ , but find no major qualitative differences with results presented here. A systematic study of the complete range of possibilities for this parameter upon solutions behaviour is beyond the scope of the present investigation and, in any event, the value of $\gamma = (F_1 - F_3)$ used here is surely of the most physical relevance.

A variety of superharmonic resonances between the different solution modes were computed in this study. In the out-of-phase case at $k = 0.5$, where successive $1:n$ resonances were computed with the shorter wavelength component either in or out of phase, this type of solution was especially abundant. It was seen that, in a nonlinear regime, these resonances were able to be excited at an earlier wave speed than linear theory predicted, with this effect becoming more pronounced for larger amplitudes of the primary mode of solution.

The stability of the nonlinear solutions is an open question. The infinitesimal solutions of section 2.3 will be neutrally stable. Further investigation is required, however, to determine the precise nature of the finite amplitude solutions in a time dependent regime. It was seen that, where resonant effects were not present, the maximum amplitude solutions were only mildly nonlinear and without any obvious geometric limitation. This appears to be in line with the notion of a ‘dynamical limit’, as suggested by Saffman and Yuen [51], the point beyond which any larger amplitude solutions will be unstable.

Future work will include formulating a time-dependent version of this problem, possibly in a similar manner to that by which the Rayleigh-Taylor instability was computed by Forbes et al. [25]. Such a technique would permit a finite steady amplitude solution computed in this chapter to be used as an initial condition in a time-dependent formulation of the flow.

In the following chapter, this technique of Forbes et al. [25] will be applied to the Kelvin-Helmholtz instability. The effects of shear, as in the middle layer of the current chapter, will be accounted for more directly using an approximate (Boussinesq) representation of viscosity, and interfaces of finite thickness.

CHAPTER 3

Accurate methods for computing inviscid and viscous Kelvin-Helmholtz instability

3.1. Introduction

The interface between two inviscid fluids is unstable if there is a large enough difference in the relative velocities of the fluids on either side of the interface. The classical version of this problem outlined by Lord Kelvin [32] and Helmholtz [30], and the associated linear analysis recounted by authors such as Lamb [35] and Taylor [56], involves perturbing the interface between two horizontal fluid layers in relative motion with a small amplitude sinusoid. Under certain conditions this situation is highly unstable and perturbations to the interface will grow exponentially. The non-linear version of the problem has been thoroughly studied and certain phenomena are associated with it. Aside from exponential growth at early times, perhaps the best known of these phenomena is the eventual roll-up of the interface into a ‘cat’s eye’-type spiral [50]. At some finite time before this roll-up occurs, a singularity in curvature appears on the interface, and a famous asymptotic approximation for curvature singularity formation time is given by Moore [42].

The Kelvin-Helmholtz instability occurs in a wide variety of physical situations, often arising as a natural consequence of modelling some other process. A classic example is the spectacular billowing cloud formations in the lower atmosphere, an occurrence which is often associated with atmospheric turbulence [53]. More exotically, there is some evidence to suggest that Kelvin-Helmholtz instability may be the mechanism behind the phenomenon of a glitching pulsar (where the period of a neutron star, as observed terrestrially, becomes temporarily erratic) [38].

Synonymous with the Kelvin-Helmholtz instability is the related problem of a vortex sheet, where the evolution of an infinitesimally thin layer of infinite vorticity is studied. In particular, a diffeo-integral equation formulation of the problem, the Birkhoff-Rott equation [8], has been analysed thoroughly with many theoretical and computational studies. Notably, these studies include the work of Moore [42] and Cowley et al. [17] where the formation of interfacial curvature singularities is investigated with asymptotic techniques. The viscous version of the Kelvin-Helmholtz instability for a liquid-gas interfaces has been investigated in some detail by Funada and Joseph [29].

The work of several authors suggests that there are a few difficulties inherent in computing fluid instabilities of this type. In the vortex sheet formulation the evolution of the interface is often impeded by the appearance of small (typically at near grid scale) wavelength ‘wiggles’ after some finite time. This blow-up of higher order modes is essentially due to the fact that a perturbation at any wavelength smaller than the primary mode will also be unstable. Hence, the response of the system to the small inaccuracies that are (inevitably) introduced as the computation proceeds through time is to generate spurious secondary instabilities which may become so severe as to cloud the effects that were intended to be studied. There are several approaches that may be employed to mitigate against this occurrence: Krasny [33] employs a spectral filtering technique, whilst Tryggvason et al. [58] use viscosity, effectively to regularize the problem, for example.

The appearance of the curvature singularity after finite time also presents certain computational challenges, particularly when using spectral methods. In the closely related problem of the inviscid Rayleigh-Taylor instability it has been found that it is not possible to continue following the evolution of the solution after the point of curvature singularity formation; see the investigations of Forbes, Chen & Trenham [25] and Forbes [24]. Despite this, this type of spectral method has the advantage of being able to compute the shape of the interface most efficiently and to a high degree of accuracy up to the point where it breaks down. The methods

of Forbes et al. [25] will be adapted in section 3.4 to analyse the inviscid Kelvin-Helmholtz instability. A finite difference scheme is then introduced in section 3.5 to compute solutions to the viscous version of the problem since such methods are typically more computationally efficient and stable than a spectral method for this type of flow.

Two versions of the Kelvin-Helmholtz instability will be presented in this chapter: an inviscid version that is essentially an extension of the classical formulation and a comparable situation in weakly compressible Boussinesq fluid, where viscosity is included. Walls are added above and below the interface, providing a finite computational domain which should allow for comparisons to be drawn between the inviscid and viscous models. Section 3.3 presents a perturbation analysis of a linearized version of the inviscid problem and a stability criterion is obtained, similar to analysis of the unbounded flow given by authors such as Lamb [35, article 232] and Chandrasekhar [11, chapter 11]. A novel spectral method, of the type presented in Forbes et al. [25], is introduced in section 3.4 and this is used to compute a non-linear solution up to the point of curvature singularity formation. This method makes use of a novel smoothing technique to suppress the blow-up of higher order modes. In order to investigate the behaviour of the instability past the formation of a curvature singularity a related, and very similar, version of the instability is modelled in sections 3.5–3.6 for viscous fluid flow. Here the sharp interface of the inviscid problem is replaced by an interfacial region of finite width and the initial conditions (which are now continuous profiles) must be specified with care. The introduction of this finite width ‘interface’ means that the vorticity on the interface is no longer infinite and as a consequence it will be possible to follow the evolution of the viscous flow past the point where a curvature singularity forms in the inviscid problem. The focus of this chapter will be on accurately tracking the shape of the viscous interface with an efficient numerical scheme, with a view to examining effects such as the roll-up of the interface at later times. Additionally the evolution of inviscid and viscous flows will be compared up to the point that

the interface in the inviscid problem develops a singularity in curvature. A similar comparison between an inviscid and viscous versions of the problem has been made in detail by Tryggvason et al. [58].

3.2. Inviscid model: governing equations

The Kelvin-Helmholtz instability involves two fluid layers flowing parallel to each other. Such a system will evolve unstably when subject to a small interfacial perturbation if there is a large enough difference in the horizontal velocities of the two layers. In the classical treatment of this problem by authors such as Lamb [35] and Taylor [56] it assumed that the two fluid layers are unbounded (infinitely deep). The version of the problem considered here assumes that both layers have a finite depth with an upper layer of depth h_1 and the lower layer of depth h_2 . (Hereafter all quantities subscripted with a 1 are properties of the upper layer, whilst quantities subscripted with a 2 refer to the lower layer.) Similarly the densities of the two layers are ρ_1 and ρ_2 , where it is always the case that $\rho_2 > \rho_1$ so that buoyancy effects do not dominate. Each layer has a base horizontal speed, given by c_1 and c_2 , respectively.

It is convenient to introduce non-dimensional variables before proceeding further. The depth of the lower layer h_2 will be used as a length scale. This leads to a natural choice of time and speed scales, namely $h_2/\sqrt{gh_2}$ and $\sqrt{gh_2}$. Density is scaled relative to the lower layer density ρ_2 . The crucial parameters of the problem are now reduced to two Froude numbers, $F_1 = c_1/\sqrt{gh_2}$ and $F_2 = c_2/\sqrt{gh_2}$, and a density ratio $D = \rho_1/\rho_2$, where $D < 1$. The dimensionless upper layer depth is now $h = h_1/h_2$.

The dimensionless configuration of the flow is shown in figure 3.1. When unperturbed, the two fluid layers are separated by an infinitely thin interface at $y = 0$ and are bounded by horizontal walls lying at $y = -1$ and $y = h$. More generally the interface will be represented by a function $y = \eta(x, t)$ that will evolve through time, meaning that the exact shape of each layer is not known a priori. In addition to the

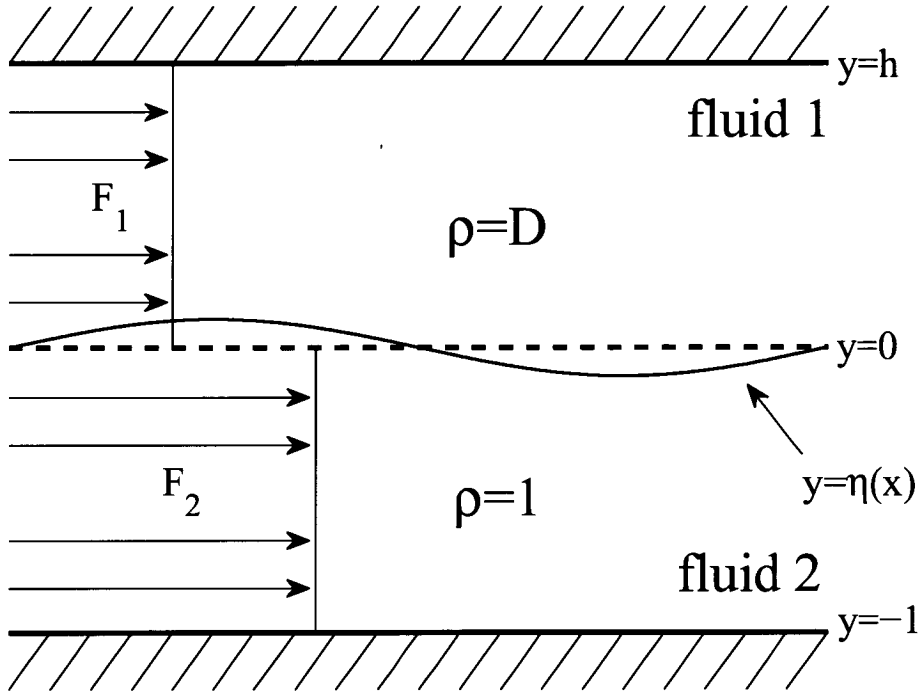


FIGURE 3.1. A schematic diagram showing the flow configuration for the inviscid model.

fluid in each layer being inviscid, it is also assumed that each fluid is incompressible and flows irrotationally. As a consequence, velocity potentials, Φ_1 and Φ_2 , may be introduced in each layer where these relate to the horizontal and vertical components of velocity by simple differentiation, $u_i = F_i + \partial\Phi_i/\partial x$ and $v_i = \partial\Phi_i/\partial y$ for $i = 1, 2$. Both potentials satisfy Laplace's equation in their respective layers

$$\nabla^2\Phi_1 = 0 \quad \text{for } \eta(x, t) < y < h$$

$$\nabla^2\Phi_2 = 0 \quad \text{for } -1 < y < \eta(x, t)$$

where each region is bounded by a wall and the interface function. There are three boundary conditions on the interface. The tangential component of velocity on

either side of the interface is zero, leading to the kinematic boundary conditions

$$\frac{\partial \eta}{\partial t} = v_i - u_i \frac{\partial \eta}{\partial x} \quad \text{on } y = \eta(x) \quad (3.2.1)$$

in each layer $i = 1, 2$. A dynamic boundary condition is obtained by writing Bernoulli's equation in each layer and then equating pressure at the interface, and the resulting expression is

$$\begin{aligned} \frac{\partial \Phi_2}{\partial t} - D \frac{\partial \Phi_1}{\partial t} &= \frac{1}{2} F_2^2 - \frac{1}{2} D F_1^2 - \frac{1}{2} (u_2^2 + v_2^2) \\ &+ \frac{1}{2} D (u_1^2 + v_1^2) - (1 - D) y \quad \text{on } y = \eta(x) \end{aligned} \quad (3.2.2)$$

where it is understood that all quantities are evaluated on the interface $y = \eta(x, t)$. Inviscid slip conditions are present at the top and bottom walls so that $v_1 = 0$ on $y = h$ and $v_2 = 0$ on $y = -1$. It is assumed that the solutions are periodic in x with wavelength $\lambda = 2\pi/k$, where k is a dimensionless wavenumber. In sections 3.3 and 3.4 this will be used as the wavelength of the perturbation to the interface. Ultimately the stability of the interface and its subsequent evolution will be determined by the five parameters of the system, namely the wavenumber k , the upper layer depth h , the density ratio D and the two Froude numbers, F_1 and F_2 .

3.3. Linearized solution for inviscid problem

It is instructive to study the behaviour of the system outlined in section 3.2 when dealing with a perturbation of small amplitude. The linearization technique used here is similar to the classical treatment of the Kelvin-Helmholtz problem, presented in Lamb [35, article 232], with the presence of the walls the only slight modification. It will be seen that this is but a minor complication, leading to a slightly more elaborate stability criterion than in the case of unbounded flow. A similar result to that that is derived here is given by Turner [59, page 95].

It is assumed that the solution is a small perturbation about the base flow, in which the interface is purely horizontal. The appropriate perturbed forms of the

interface height function and the velocity potentials are

$$\eta(x, t) = \varepsilon H(x, t) + \mathcal{O}(\varepsilon^2) \quad (3.3.1)$$

$$\Phi_1(x, y, t) = \varepsilon \Phi_{11}(x, y, t) + \mathcal{O}(\varepsilon^2) \quad (3.3.2)$$

$$\Phi_2(x, y, t) = \varepsilon \Phi_{21}(x, y, t) + \mathcal{O}(\varepsilon^2) \quad (3.3.3)$$

in which ε is a small parameter proportional to the amplitude of the interfacial wave. By substituting (3.3.1)–(3.3.3) into the kinematic conditions (3.2.1) and discarding terms of order ε^2 and higher, a linearized version of the conditions is obtained in the form

$$\frac{\partial H}{\partial t} = \frac{\partial \Phi_{i1}}{\partial y} - F_i \frac{\partial H}{\partial x} \quad \text{on } y = 0 \quad (3.3.4)$$

with $i = 1, 2$, as before. Similarly the linearized version of the dynamic condition (3.2.2) is

$$\frac{\partial \Phi_{21}}{\partial t} - D \frac{\partial \Phi_{11}}{\partial t} = DF_1 \frac{\partial \Phi_{11}}{\partial x} - F_2 \frac{\partial \Phi_{21}}{\partial x} - (1 - D)H \quad \text{on } y = 0 \quad (3.3.5)$$

where (3.3.1)–(3.3.3) have been substituted into the dynamic condition (3.2.2) and terms of order ε^2 have been discarded. It is assumed that the perturbed interface height function H in equation (3.3.1) will be a travelling wave of period $2\pi/k$ and frequency ω , so that

$$H(x, t) = g_1 e^{i(\omega t - kx)}. \quad (3.3.6)$$

Here g_1 is an arbitrary initial amplitude, possibly complex. The corresponding solutions for the velocity potentials are

$$\Phi_{11}(x, y, t) = a_1 \cosh(k(y - h)) e^{i(\omega t - kx)} \quad (3.3.7)$$

$$\Phi_{21}(x, y, t) = a_2 \cosh(k(y + 1)) e^{i(\omega t - kx)} \quad (3.3.8)$$

where the hyperbolic cosine is required to satisfy the condition that the vertical component of velocity is zero at either wall. The crucial parameter here is ω , as

instability occurs when this develops a non-zero imaginary part. By substituting the travelling wave solution (3.3.6)–(3.3.8) into the linearized boundary conditions (3.3.4)–(3.3.5) it is possible to solve for ω in terms of the other parameters of the system. The ultimate expression for ω is

$$\omega = \frac{2k}{\coth k + D \coth kh} \left\{ F_2 \coth k + DF_1 \coth kh \right. \\ \left. \pm \frac{1}{k} \sqrt{(1-D)(\coth k + D \coth kh) - kD \coth k \coth kh (F_1 - F_2)^2} \right\}$$

which leads to the criterion that the flow will be unstable when

$$(1-D)(\coth k + D \coth kh) - kD \coth k \coth kh (F_1 - F_2)^2 < 0$$

or, by simple rearrangement, a more useful version is obtained in the form

$$|F_1 - F_2| > \sqrt{\frac{(1-D) \coth k + D \coth kh}{D} \frac{1}{k \coth k \coth kh}}. \quad (3.3.9)$$

Thus instability will occur when the difference in Froude numbers is large enough. The classical result for unbounded fluids is that instability occurs for perturbations of small enough wavelength (see Lamb [35]), and this still holds in (3.3.9) when the upper and lower walls are present. The criterion obtained by Lamb may be reproduced from (3.3.9) by taking the limit as $k \rightarrow \infty$, effectively setting the hyperbolic cotangents to 1.

3.4. Non-linear solution for inviscid problem

The inviscid problem will now be solved using a novel method based on Fourier series techniques. This is an extension of methods originally developed in Forbes et al. [25] to model the closely related problem of the inviscid Rayleigh-Taylor instability. In that treatment of the Rayleigh-Taylor problem an arc-length formulation was introduced to represent the interface height function. Whilst such a formulation has the potential to represent multi-valued interfaces and capture phenomena such as roll-up, it was found in Forbes et al. [25] that this was generally not possible

without somehow regularizing the problem (for instance with surface tension) and even then the competing interests of a small amount of roll-up against the formation of a curvature singularity meant that the method broke down a small time after the interface became multi-valued. It will be assumed here that the interface height is single valued, and it is anticipated that the method will break down after some finite time, namely at the formation of a curvature singularity in the interface height function.

The appropriate forms of the Fourier series solutions for the interface height η and the two velocity potentials, Φ_1 and Φ_2 , are

$$\eta(x, t) = P_0 + \sum_{n=1}^N P_n(t) \cos(nkx) + Q_n(t) \sin(nkx) \quad (3.4.1)$$

$$\Phi_1(x, y, t) = \sum_{n=1}^N \cosh(nk(y - h)) [A_n(t) \cos(nkx) + B_n(t) \sin(nkx)] \quad (3.4.2)$$

$$\begin{aligned} \Phi_2(x, y, t) = & C_0(t) + \sum_{n=1}^N \cosh(nk(y + 1)) [C_n(t) \cos(nkx) \\ & + D_n(t) \sin(nkx)]. \end{aligned} \quad (3.4.3)$$

These solutions become exact as $N \rightarrow \infty$. As with the linearized solution of section 3.3 a hyperbolic cosine dependence in the velocity potentials is necessary to satisfy the conditions that the vertical component of velocity is zero at both walls. Here the time dependent coefficients A_n , B_n , C_n , D_n , P_n , Q_n , for $n = 1 \dots N$, and C_0 have been introduced; it is these $6N + 1$ coefficients that will be solved for. The mean height of the interface P_0 may be shown to be constant, as in Forbes et al. [25], and in practice will be set to zero.

A large system of differential equations for the coefficients is obtained by substituting the series representations (3.4.1)–(3.4.3) into the boundary conditions (3.2.1)–(3.2.2), multiplying by Fourier basis functions and integrating over a period. Taking the kinematic conditions (3.2.1), multiplying by the even Fourier

basis functions $\cos(jkx)$ and integrating over a horizontal period gives

$$\frac{\pi}{k}P'_j = -\pi F_1 Q_j + jk \sum_{n=1}^N S_{jn}^{(1S)} A_n - jk \sum_{n=1}^N T_{jn}^{(1S)} B_n \quad (3.4.4)$$

$$\frac{\pi}{k}P'_j = -\pi F_2 Q_j + jk \sum_{n=1}^N S_{jn}^{(2S)} C_n - jk \sum_{n=1}^N T_{jn}^{(2S)} D_n \quad (3.4.5)$$

where $j = 1 \dots N$ and the integrals

$$\begin{aligned} S_{jn}^{(1S)} &= \int_0^{2\pi/k} \sinh(nk(\eta - h)) \sin(nkx) \sin(jkx) dx \\ S_{jn}^{(2S)} &= \int_0^{2\pi/k} \sinh(nk(\eta + 1)) \sin(nkx) \sin(jkx) dx \\ T_{jn}^{(1S)} &= \int_0^{2\pi/k} \sinh(nk(\eta - h)) \cos(nkx) \sin(jkx) dx \\ T_{jn}^{(2S)} &= \int_0^{2\pi/k} \sinh(nk(\eta + 1)) \cos(nkx) \sin(jkx) dx \end{aligned}$$

have been defined for convenience of notation. These integrals feature the odd Fourier basis $\sin(jkx)$ owing to an intermediate integration by parts step. The corresponding differential equations obtained by multiplying (3.2.1) by $\sin(jkx)$ and integrating over a period are

$$\frac{\pi}{k}Q'_j = \pi j F_1 P_j - jk \sum_{n=1}^N S_{jn}^{(1C)} A_n + jk \sum_{n=1}^N T_{jn}^{(1C)} B_n \quad (3.4.6)$$

$$\frac{\pi}{k}Q'_j = \pi j F_2 P_j - jk \sum_{n=1}^N S_{jn}^{(2C)} C_n + jk \sum_{n=1}^N T_{jn}^{(2C)} D_n \quad (3.4.7)$$

again with $j = 1 \dots N$. Here the integrals

$$\begin{aligned} S_{jn}^{(1C)} &= \int_0^{2\pi/k} \sinh(nk(\eta - h)) \sin(nkx) \cos(jkx) dx \\ S_{jn}^{(2C)} &= \int_0^{2\pi/k} \sinh(nk(\eta + 1)) \sin(nkx) \cos(jkx) dx \\ T_{jn}^{(1C)} &= \int_0^{2\pi/k} \sinh(nk(\eta - h)) \cos(nkx) \cos(jkx) dx \\ T_{jn}^{(2C)} &= \int_0^{2\pi/k} \sinh(nk(\eta + 1)) \cos(nkx) \cos(jkx) dx \end{aligned}$$

have been defined. To avoid redundancy only equations (3.4.4) and (3.4.7) appear in the system of differential equations. The other two equations (3.4.5) and (3.4.6) are replaced with the differences between equations (3.4.4) and (3.4.5) and equations (3.4.6) and (3.4.7), respectively. These two new equations are then further differentiated directly with respect to time to yield

$$\begin{aligned} 0 = & \frac{\pi}{k}(F_1 - F_2)Q'_j + \sum_{n=1}^N \mathcal{L}_{jn}^{(S)} P'_n + \sum_{n=1}^N \mathcal{M}_{jn}^{(S)} Q'_n \\ & - \sum_{n=1}^N \mathcal{S}_{jn}^{(1S)} A'_n + \sum_{n=1}^N \mathcal{T}_{jn}^{(1S)} B'_n + \sum_{n=1}^N \mathcal{S}_{jn}^{(2S)} C'_n - \sum_{n=1}^N \mathcal{T}_{jn}^{(2S)} D'_n \end{aligned} \quad (3.4.8)$$

for $j = 1 \dots N$, and

$$\begin{aligned} 0 = & \frac{\pi}{k}(F_1 - F_2)P'_j + \sum_{n=1}^N \mathcal{L}_{jn}^{(C)} P'_n + \sum_{n=1}^N \mathcal{M}_{jn}^{(C)} Q'_n \\ & - \sum_{n=1}^N \mathcal{S}_{jn}^{(1C)} A'_n + \sum_{n=1}^N \mathcal{T}_{jn}^{(1C)} B'_n + \sum_{n=1}^N \mathcal{S}_{jn}^{(2C)} C'_n - \sum_{n=1}^N \mathcal{T}_{jn}^{(2C)} D'_n \end{aligned} \quad (3.4.9)$$

for $j = 1, \dots, N$. In addition to those previously defined, some integrals related to the velocity potentials have been written as

$$\begin{aligned} \mathcal{L}_{jn}^{(C)} &= \int_0^{2\pi/k} \left(\frac{\partial \Phi_1}{\partial x} - \frac{\partial \Phi_2}{\partial x} \right) \cos(nkx) \cos(jkx) dx \\ \mathcal{L}_{jn}^{(S)} &= \int_0^{2\pi/k} \left(\frac{\partial \Phi_1}{\partial x} - \frac{\partial \Phi_2}{\partial x} \right) \cos(nkx) \sin(jkx) dx \\ \mathcal{M}_{jn}^{(C)} &= \int_0^{2\pi/k} \left(\frac{\partial \Phi_1}{\partial x} - \frac{\partial \Phi_2}{\partial x} \right) \sin(nkx) \cos(jkx) dx \\ \mathcal{M}_{jn}^{(S)} &= \int_0^{2\pi/k} \left(\frac{\partial \Phi_1}{\partial x} - \frac{\partial \Phi_2}{\partial x} \right) \sin(nkx) \sin(jkx) dx. \end{aligned}$$

The dynamic condition (3.2.2) is dealt with in a similar way. Two sets of differential equations are obtained, and the result of multiplying (3.2.2) by the odd and even Fourier basis functions $\sin(jkx)$ and $\cos(jkx)$ and integrating over a period are

respectively

$$-D \sum_{n=1}^N \mathcal{G}_{jn}^{(1S)} A'_n - D \sum_{n=1}^N \mathcal{H}_{jn}^{(1S)} B'_n + \sum_{n=1}^N \mathcal{G}_{jn}^{(2S)} C'_n + \sum_{n=1}^N \mathcal{H}_{jn}^{(2S)} = \mathcal{I}_j^{(S)} \quad (3.4.10)$$

$$-D \sum_{n=1}^N \mathcal{G}_{jn}^{(1C)} A'_n - D \sum_{n=1}^N \mathcal{H}_{jn}^{(1C)} B'_n + \sum_{n=1}^N \mathcal{G}_{jn}^{(2C)} C'_n + \sum_{n=1}^N \mathcal{H}_{jn}^{(2C)} = \mathcal{I}_j^{(C)} \quad (3.4.11)$$

for $j = 1 \dots N$, where the integrals

$$\begin{aligned} \mathcal{H}_{jn}^{(1C)} &= \int_0^{2\pi/k} \cosh(nk(\eta - h)) \sin(nkx) \cos(jkx) dx \\ \mathcal{H}_{jn}^{(2C)} &= \int_0^{2\pi/k} \cosh(nk(\eta + 1)) \sin(nkx) \cos(jkx) dx \\ \mathcal{H}_{jn}^{(1S)} &= \int_0^{2\pi/k} \cosh(nk(\eta - h)) \sin(nkx) \sin(jkx) dx \\ \mathcal{H}_{jn}^{(2S)} &= \int_0^{2\pi/k} \cosh(nk(\eta + 1)) \sin(nkx) \sin(jkx) dx \\ \mathcal{G}_{jn}^{(1C)} &= \int_0^{2\pi/k} \cosh(nk(\eta - h)) \cos(nkx) \cos(jkx) dx \\ \mathcal{G}_{jn}^{(2C)} &= \int_0^{2\pi/k} \cosh(nk(\eta + 1)) \cos(nkx) \cos(jkx) dx \\ \mathcal{G}_{jn}^{(1S)} &= \int_0^{2\pi/k} \cosh(nk(\eta - h)) \cos(nkx) \sin(jkx) dx \\ \mathcal{G}_{jn}^{(2S)} &= \int_0^{2\pi/k} \cosh(nk(\eta + 1)) \cos(nkx) \sin(jkx) dx \end{aligned}$$

have been introduced. Additionally, the integrals on the right hand sides of (??)

and (??) are

$$\begin{aligned} \mathcal{I}_j^{(S)} &= \int_0^{2\pi/k} \mathcal{J} \sin(jkx) dx \\ \mathcal{I}_j^{(C)} &= \int_0^{2\pi/k} \mathcal{J} \cos(jkx) dx \end{aligned}$$

and \mathcal{J} is the right hand side of the dynamic condition (3.2.2)

$$\mathcal{J} = \frac{1}{2} F_2^2 - \frac{1}{2} D F_1^2 - \frac{1}{2} (u_2^2 + v_2^2) + \frac{1}{2} D (u_1^2 + v_1^2) - (1 - D) \eta. \quad (3.4.12)$$

Finally the dynamic condition is integrated over a period to give the single equation

$$\begin{aligned}
 & -D \sum_{n=1}^N \mathcal{G}_{0n}^{(1)} A'_n - D \sum_{n=1}^N \mathcal{H}_{0n}^{(1)} B'_n \\
 & + \sum_{n=1}^N \mathcal{G}_{0n}^{(2)} C'_n + \sum_{n=1}^N \mathcal{H}_{0n}^{(2)} D'_n + \frac{2\pi}{k} C'_0 = \mathcal{I}_0.
 \end{aligned} \tag{3.4.13}$$

for the zeroth Fourier mode. Again, the intermediate integral quantities

$$\begin{aligned}
 \mathcal{G}_{0n}^{(1)} &= \int_0^{2\pi/k} \cosh(nk(\eta - h)) \cos(nkx) dx \\
 \mathcal{H}_{0n}^{(1)} &= \int_0^{2\pi/k} \cosh(nk(\eta - h)) \sin(nkx) dx \\
 \mathcal{G}_{0n}^{(2)} &= \int_0^{2\pi/k} \cosh(nk(\eta + 1)) \cos(nkx) dx \\
 \mathcal{H}_{0n}^{(2)} &= \int_0^{2\pi/k} \cosh(nk(\eta + 1)) \sin(nkx) dx \\
 \mathcal{I}_0 &= \int_0^{2\pi/k} \mathcal{J} dx.
 \end{aligned}$$

have been introduced for convenience of notation.

The required system of $6N + 1$ differential equations is thus given by (3.4.4), (3.4.7) and (3.4.8)–(3.4.13). This large system will be solved numerically and so it is convenient to write it in a vectorized form

$$\mathbf{M} \mathbf{S}' = \mathcal{R}$$

where $\mathbf{S} = [A_n, B_n, C_n, D_n, P_n, Q_n, C_0]$ is a vector of the unknown coefficients, \mathbf{M} is a mass matrix for the left hand side of the differential equations and \mathcal{R} is a vector of the right hand sides of the systems of differential equations.

Solutions to the system will be computed using the ODE113 routine of MATLAB, which is a variable order (between 1 and 13) Adams method. This provides a good balance between computational efficiency (specifically, the choice of time step size) and accuracy of the solution, especially at small times. All the integrals are evaluated using the trapezoidal rule with the number of grid points adjusted to

provide sufficient accuracy for the choice of N , the number of coefficients in each of the series (3.4.1)–(3.4.3).

A well known computational issue with the unregularized Kelvin-Helmholtz problem is the blow-up of higher-order modes in the interface function, as discussed by Krasny [33], for example. The common approaches involve either altering the problem under consideration, typically by introducing some kind of regularization such as surface tension (see Siegel [52] or Hou et al. [31]) or a finite width interfacial layer (for instance Baker & Shelley [6]), or somehow to smooth out these anomalies during the computational process (see Krasny [33]). The latter approach is adopted here. A smoothing scheme similar to that used by Longuet-Higgins & Cokelet [37] in the computation of free-surface waves is introduced to filter the higher order modes. This may be applied either after each time-step of the differential equation solver or perhaps more appropriately, for early times, as is required to keep the blow-up of higher order modes at an acceptably low level. The aim here is to prevent the erroneous blow-up in these high order solution components from leading to inaccuracies in lower order modes at later times. The scheme presented here will filter both even and odd modes. To smooth out the blow-up of the even M -th mode, for instance, the Fourier series representation of surface elevation η in equation (3.4.1) is evaluated on a grid of $2M + 1$ evenly spaced points spanning one period, that is from 0 to $2\pi/k$. A 5-point smoothing function is then applied to each grid point to obtain a new smoothed function $\bar{\eta}$

$$\bar{\eta}(x_j) = \frac{1}{16} (-\eta(x_{j-2}) + 4\eta(x_{j-1}) + 10\eta(x_j) + 4\eta(x_{j+1}) - \eta(x_{j+2}))$$

where $x_j = \pi(j - 1)/kM$ are the grid points. This averaged function is then re-Fourier analyzed to obtain a set of smoothed Fourier coefficients. To smooth out an odd higher order mode of the Fourier series representation the same smoothing function is used but the grid is shifted by a quarter of the period of the mode being targeted, so that the grid points used are $x_j = \pi(2j - 1)/(2kM)$. Typically this procedure is repeated several times to smooth out a number of modes at each

time step. For early time steps, where the solution is expected to be close to the linear solution, it may be necessary to smooth out up to half of the coefficients (both odd and even), then relaxing this for later time steps when the solution will genuinely have higher-order modes present, rather than the erroneous blow-up that this smoothing procedure is designed to mitigate against.

3.4.1. Choice of initial conditions. The choice of the initial values of the coefficients is crucial; the problem is both highly unstable and strongly non-linear so that the evolution of the solution at later times is very sensitive to small changes in the initial condition. It is desirable that the initial condition of the non-linear system is identical to that of the linearized solution of section 3.3. A feature of that condition is that both the interface height function and the two velocity potentials are perturbed in a very specific way. In order to obtain usable expressions from the linearized solution the time-dependency parameter ω from the travelling wave solution is split into its real and imaginary parts, $\omega = \omega_1 + i\omega_2$ with both ω_1 and ω_2 purely real. The most intuitive way to initiate the non-linear system is to give the interface height function some small perturbation and work out the corresponding expressions for the velocity potentials. Taking only the real part of expressions (3.3.6)–(3.3.8) we have

$$\begin{aligned} H(x, 0) &= P_{10} \cos kx + Q_{10} \sin kx \\ \Phi_{11}(x, y, 0) &= \cosh(k(y - h))(A_{10} \cos kx + B_{10} \sin kx) \\ \Phi_{21}(x, y, 0) &= \cosh(k(y + 1))(C_{10} \cos kx + D_{10} \sin kx) \end{aligned}$$

in which the coefficients A_{10} , B_{10} etc. are purely real and will be used to approximate the first coefficients in each of the series. Thus, $P_1(0) = P_{10}$ and so on. It is necessary to choose values for the velocity potential coefficients so that they match exactly a given perturbation of the interface height function. By simple rearrangement of the linearized kinematic conditions it is possible to obtain, after a little

algebra,

$$\begin{aligned}
A_{10} &= (Q_{10}(\omega_1 - F_1 k) + \omega_2 P_{10})/k \sinh kh \\
B_{10} &= (-P_{10}(\omega_1 - F_1 k) + \omega_2 Q_{10})/k \sinh kh \\
C_{10} &= (-Q_{10}(\omega_1 - F_2 k) - \omega_2 P_{10})/k \sinh k \\
D_{10} &= (P_{10}(\omega_1 - F_2 k) - \omega_2 Q_{10})/k \sinh k.
\end{aligned}$$

A complete initial condition for the non-linear problem is formed by setting the first coefficient of each series equal to the respective expression above with the remaining coefficients set to zero. It will be usual either to perturb the interface with a pure sine or cosine of a certain amplitude, so in practice in the above expressions either P_{10} or Q_{10} will be set to zero.

3.5. Weakly compressible viscous model: Governing Equations

The inviscid model described in sections 3.2–3.4 suffers from the the limitation that a curvature singularity will form at the interface after a finite time, after which it will cease to be valid [42]. As a result it is necessary to modify the classical inviscid problem to obtain solutions beyond this time, where features such as interfacial roll-up may develop. When dealing with an infinitely thin interface the problem may be regularized by including effects like surface tension or viscosity. Another approach is to replace the interface with an interfacial region of finite depth. Sometimes known as a vortex layer (as opposed to a vortex sheet), this has the advantage of having a region of large but finite vorticity as opposed to the infinite vorticity that is present at a genuine interface; this finite vorticity is inherently easier to handle computationally. A combination of these approaches will be adopted here. The inviscid problem will be mimicked by considering a body of weakly compressible fluid with a small amount of viscosity. Initial conditions for both velocity and density will be specified carefully with a view to matching closely those of the inviscid system of sections 3.2–3.4. Essentially, the sharp changes in density and

velocity are replaced with continuously varying profiles in which the changes now occur rapidly, but smoothly, over a layer of small finite width.

This new system will be governed by a weakly compressible version of the Navier-Stokes equations based on those used by Farrow and Hocking [21] to model tank withdrawal flows. The formulation will be slightly different as the problem is particularly well suited to adopting a vorticity-streamfunction formulation. Vorticity is a quantity of obvious interest for this particular flow and it is convenient to use it directly to model this instability. Implicit in this Boussinesq formulation is the assumption that density does not vary much and may be written as the sum of an average density ρ_0 and an unsteady component $\bar{\rho}$, in the form $\rho(x, y, t) = \rho_0 + \bar{\rho}(x, y, t)$. Density only appears as a derivative in this formulation and so ρ and $\bar{\rho}$ will be used interchangeably throughout. Beginning with the primitive variables system of Farrow and Hocking [21], vorticity ζ is introduced, defined as $\zeta = \partial v / \partial x - \partial u / \partial y$. Since the fluid is nearly incompressible a streamfunction ψ exists such that $u = \partial \psi / \partial y$ and $v = -\partial \psi / \partial x$, and by taking the curl of the momentum equations the pressure may be eliminated. The resulting system is

$$\frac{\partial^2 \psi}{\partial x^2} + \frac{\partial^2 \psi}{\partial y^2} = -\zeta \quad (3.5.1)$$

$$\frac{\partial \zeta}{\partial t} + u \frac{\partial \zeta}{\partial x} + v \frac{\partial \zeta}{\partial y} = \nu \left(\frac{\partial^2 \zeta}{\partial x^2} + \frac{\partial^2 \zeta}{\partial y^2} \right) - \frac{\partial \rho}{\partial x} \quad (3.5.2)$$

$$\frac{\partial \rho}{\partial t} + u \frac{\partial \rho}{\partial x} + v \frac{\partial \rho}{\partial y} = \sigma \left(\frac{\partial^2 \rho}{\partial x^2} + \frac{\partial^2 \rho}{\partial y^2} \right). \quad (3.5.3)$$

Here the parameters ν and σ control the viscosity and diffusivity respectively. Specifically, ν is the inverse of a dimensionless Reynolds number and σ is a scaled inverse Prandtl number, controlling the rate at the which fluids diffuse. This formulation has the advantage of not needing to deal with pressure explicitly and has one fewer governing equations than would the equivalent system in primitive variables.

Equations (3.5.1)–(3.5.3) will be solved using finite difference methods. To do this the governing equations will be discretized over a box with equivalent dimensions to that of the region used in the inviscid problem. The box will be of height

$h + 1$ and have a width of one wavelength $\lambda = 2\pi/k$ of the perturbation. A discrete grid with M points in the x -direction and N points in the y -direction is defined with constant grid spacings $\Delta x = 2\pi/k(M - 1)$ and $\Delta y = (h + 1)/(N - 1)$. Before giving details of the discretization it is useful to specify boundary conditions on the box. Periodicity is assumed for all variables in the x -direction, so that $\psi(0, y, t) = \psi(2\pi/k, y, t)$ and similarly for ζ , ρ , u and v . Slip conditions are implemented on the top and bottom walls; hence, at $y = -1$ and $y = h$ the vertical component of velocity v is equal to zero. This implies that both ψ and ω must also be constant at the walls. At the lower wall $y = -1$ we impose the conditions $\rho = 1$, $\psi = 0$ and $\zeta = 0$. On the upper boundary $y = h$ the conditions are $\rho = D$, $\psi = \psi_0$ and $\zeta = 0$, in which the constant ψ_0 is determined from the initial condition. The use of the slip condition, $\zeta = 0$, on both walls is a widely used approximation (see, for instance, Farrow & Hocking [21]) and simplifies the numerical scheme greatly. Another advantage to this choice is that viscous boundary layers will not form at the walls meaning that computational effort will not be put into resolving effects that are secondary to the development of the interface. A subscript notation will be adopted in the discretization procedure such that it will be understood that writing, for instance, $\psi_{i,j}^k$ refers to the streamfunction at the point $x = (i - 1)\Delta x$ and $y = -1 + (j - 1)\Delta y$, evaluated at the k -th time step.

The solution procedure is based on an alternating direction implicit (ADI) Peaceman-Rachford scheme. This type of solution method was proposed by Peaceman and Rachford [44] both as a way of solving the heat equation through time and as a quasi-transient method to solve Laplace's equation. The application of such a scheme here is possible as the governing equations (3.5.2) and (3.5.3) are essentially heat equations with non-linear convection terms. An ADI method involves splitting each time step in two, updating a solution first from the k -th to the $k + 1/2$ -th time step and then from the $k + 1/2$ -th to the $k + 1$ -th time step. For the first half step the equations are discretized in such a way that only the derivatives in x feature the updated (to the $k + 1/2$ -th level) values of the variable being solved for

with other terms left at the k -th level. Similarly the discretization for the second half step uses the updated values (now to the $k + 1$ -th level) only for derivatives in y . At each half-step a large system of difference equations is solved implicitly. It may be shown that methods of this type are unconditionally stable (in the von Neumann sense) for purely linear problems. Nevertheless, the choice of time step is critical to guarantee the accuracy of the solution.

To proceed from the k -th time step to the new $k + 1$ -th level, the vorticity equation (3.5.2) is updated first to the intermediate $k + 1/2$ -th level using the scheme

$$\begin{aligned} & \frac{\zeta_{i,j}^{k+\frac{1}{2}} - \zeta_{i,j}^k}{\frac{1}{2} \Delta t} + u_{i,j}^k \frac{\zeta_{i+1,j}^{k+\frac{1}{2}} - \zeta_{i-1,j}^{k+\frac{1}{2}}}{2 \Delta x} + v_{i,j}^k \frac{\zeta_{i,j+1}^k - \zeta_{i,j-1}^k}{2 \Delta y} \\ &= \sigma \left(\frac{\zeta_{i+1,j}^{k+\frac{1}{2}} - 2\zeta_{i,j}^{k+\frac{1}{2}} + \zeta_{i-1,j}^{k+\frac{1}{2}}}{\Delta x^2} + \frac{\zeta_{i,j+1}^k - 2\zeta_{i,j}^k + \zeta_{i,j-1}^k}{\Delta y^2} \right) - \frac{\rho_{i+1,j}^k - \rho_{i-1,j}^k}{2 \Delta x} \end{aligned} \quad (3.5.4)$$

to obtain a system of $M - 1$ difference equations for each row, $j = 2 \dots N - 1$ (with the first and last rows being already dealt with by the boundary conditions). Here, forward differences have been used to estimate all time derivatives, with all derivatives in space estimated with central differences. At this half-step only the derivatives in x are updated to the new level. Each system is then solved implicitly using a Thomas algorithm which has been modified to account for the periodic boundary conditions (see Press et al [47, chapter 2.7]). Similarly successive implicit systems of $N - 2$ linear equations may be formed by now updating the derivatives in y to the full step

$$\begin{aligned} & \frac{\zeta_{i,j}^{k+1} - \zeta_{i,j}^{k+\frac{1}{2}}}{\frac{1}{2} \Delta t} + u_{i,j}^k \frac{\zeta_{i+1,j}^{k+\frac{1}{2}} - \zeta_{i-1,j}^{k+\frac{1}{2}}}{2 \Delta x} + v_{i,j}^k \frac{\zeta_{i,j+1}^{k+1} - \zeta_{i,j-1}^{k+1}}{2 \Delta y} \\ &= \sigma \left(\frac{\zeta_{i+1,j}^{k+\frac{1}{2}} - 2\zeta_{i,j}^{k+\frac{1}{2}} + \zeta_{i-1,j}^{k+\frac{1}{2}}}{\Delta x^2} + \frac{\zeta_{i,j+1}^{k+1} - 2\zeta_{i,j}^{k+1} + \zeta_{i,j-1}^{k+1}}{\Delta y^2} \right) - \frac{\rho_{i+1,j}^k - \rho_{i-1,j}^k}{2 \Delta x} \end{aligned} \quad (3.5.5)$$

and considering each row $i = 1, \dots, M - 1$ in turn. A regular Thomas algorithm is then used to solve the resulting sets of difference equations to update vorticity to the $k + 1$ th level. The values of vorticity at the new time step are now used to

update streamfunction, so that (3.5.1) is satisfied to a high degree of accuracy. A quasi-time derivative is added to the Poisson equation (3.5.1)

$$\frac{\partial \psi}{\partial \tau} = \nabla^2 \psi + \zeta \quad (3.5.6)$$

which will approach zero as $\tau \rightarrow \infty$; that is, the streamfunction will converge to a steady state (in τ) solution of (3.5.6) which is equal to the desired solution of the regular Poisson equation (3.5.1). An ADI method is employed to solve (3.5.6). Each step in quasi-time τ is split into two half steps and streamfunction is updated to the new step in τ by sweeping over the rows and then columns of the grid as sets of linear equations are solved implicitly. This is done repeatedly with different values of $\Delta\tau$ until the solution has converged to an acceptable level. The discretization of (3.5.6) for first half step in τ is

$$\frac{\psi_{i,j}^{\kappa+\frac{1}{2}} - \psi_{i,j}^{\kappa}}{\frac{1}{2}\Delta\tau} = \zeta_{i,j}^{k+1} + \frac{\psi_{i+1,j}^{\kappa+\frac{1}{2}} - 2\psi_{i,j}^{\kappa+\frac{1}{2}} + \psi_{i-1,j}^{\kappa+\frac{1}{2}}}{\Delta x^2} + \frac{\psi_{i,j+1}^{\kappa} - 2\psi_{i,j}^{\kappa} + \psi_{i,j-1}^{\kappa}}{\Delta y^2}$$

where $j = 2, \dots, N-1$, and the index κ has been introduced to represent the κ -th step through τ . Sweeping across the columns the discretization is

$$\frac{\psi_{i,j}^{\kappa+1} - \psi_{i,j}^{\kappa+\frac{1}{2}}}{\frac{1}{2}\Delta\tau} = \zeta_{i,j}^{k+1} + \frac{\psi_{i+1,j}^{\kappa+\frac{1}{2}} - 2\psi_{i,j}^{\kappa+\frac{1}{2}} + \psi_{i-1,j}^{\kappa+\frac{1}{2}}}{\Delta x^2} + \frac{\psi_{i,j+1}^{\kappa+1} - 2\psi_{i,j}^{\kappa+1} + \psi_{i,j-1}^{\kappa+1}}{\Delta y^2}$$

with $i = 1, \dots, M-1$ giving the necessary implicit equations to update streamfunction fully to the $\kappa+1$ -th step. There are several factors that affect the rate of convergence of this scheme. As noted in Peaceman & Rachford [44] the choice of successive $\Delta\tau$ is crucial. There are a variety of schemes used to select these values, for instance Wachspress [64] as well as the scheme of Peaceman & Rachford [44], which amount to using quite small values for early steps in τ and gradually increasing these until quite large values of $\Delta\tau$ are used for the later iterates. The choice of $\Delta\tau$ used here is simple, but fairly robust, with the first 50 steps of the routine using $\Delta\tau = 10^{-3}$, followed by 30 steps of $\Delta\tau = 10^{-2}$ and then as many steps of $\Delta\tau = 10^{-1}$ as are needed for convergence. The acceptable level of error is simply

calculated from the Poisson equation and it is typical that $\|\nabla^2\psi + \zeta\| < 10^{-10}$ after fewer than 100 iterations. Where convergence is slow an alternate procedure may be used. For the first 50 steps in τ the step-size is still fixed $\Delta\tau = 10^{-3}$, but then for the next 30 steps $\Delta\tau$ is chosen from a range of values between 10^{-3} and 10^{-2} by running a test case and using the $\Delta\tau$ that gives the largest reduction in error at each individual step. This is repeated for a further 20 steps using values between 10^{-2} and 10^{-1} to select an optimum sequence of $\Delta\tau$ values. Applying such a procedure can reduce the number of iterates required to reach an acceptable level of convergence by up to half.

The final step in solving the governing equations is to deal with the density equation (3.5.3). This will be handled in an identical way to the solution of the vorticity equation (3.5.2), by splitting the time step in two and sweeping first across the the grid rows and then along the columns, repeatedly solving systems of implicit equations to update the density ρ to the new time level. For the first half-step in time the discretization is

$$\begin{aligned} & \frac{\rho_{i,j}^{k+\frac{1}{2}} - \rho_{i,j}^k}{\frac{1}{2}\Delta t} + u_{i,j}^{k+1} \frac{\rho_{i+1,j}^{k+\frac{1}{2}} - \rho_{i-1,j}^{k+\frac{1}{2}}}{2\Delta x} + v_{i,j}^{k+1} \frac{\rho_{i,j+1}^k - \rho_{i,j-1}^k}{2\Delta y} \\ &= \nu \left(\frac{\rho_{i+1,j}^{k+\frac{1}{2}} - 2\rho_{i,j}^{k+\frac{1}{2}} + \rho_{i-1,j}^{k+\frac{1}{2}}}{\Delta x^2} + \frac{\rho_{i,j+1}^k - 2\rho_{i,j}^k + \rho_{i,j-1}^k}{\Delta y^2} \right) \end{aligned} \quad (3.5.7)$$

where $j = 2, \dots, N-1$, so the values of density for each row are solved for implicitly. Here both components of velocity are evaluated at the new time step from the newly computed streamfunction using central difference formulas

$$\begin{aligned} u_{i,j}^{k+1} &= \frac{\psi_{i,j+1}^{k+1} - \psi_{i,j-1}^{k+1}}{2\Delta y} \\ v_{i,j}^{k+1} &= -\frac{\psi_{i+1,j}^{k+1} - \psi_{i-1,j}^{k+1}}{2\Delta x}. \end{aligned}$$

Finally, sweeping across the grid columns density is solved to the full step using a discretization with updated derivatives in y

$$\begin{aligned} & \frac{\rho_{i,j}^{k+1} - \rho_{i,j}^{k+\frac{1}{2}}}{\frac{1}{2} \Delta t} + u_{i,j}^{k+1} \frac{\rho_{i+1,j}^{k+\frac{1}{2}} - \rho_{i-1,j}^{k+\frac{1}{2}}}{2 \Delta x} + v_{i,j}^{k+1} \frac{\rho_{i,j+1}^{k+1} - \rho_{i,j-1}^{k+1}}{2 \Delta y} \\ &= \nu \left(\frac{\rho_{i+1,j}^{k+\frac{1}{2}} - 2\rho_{i,j}^{k+\frac{1}{2}} + \rho_{i-1,j}^{k+\frac{1}{2}}}{\Delta x^2} + \frac{\rho_{i,j+1}^{k+1} - 2\rho_{i,j}^{k+1} + \rho_{i,j-1}^{k+1}}{\Delta y^2} \right) \end{aligned} \quad (3.5.8)$$

with $i = 1, \dots, M-1$ and the resulting systems of $N-2$ linear equation are solved implicitly as with the vorticity equation.

There are a number of factors that are critical when using this method in practice. The choice of initial condition is somewhat problematic, and this will be dealt with in section 3.6, in as much as care needs to be taken in ensuring that the choice of vorticity and streamfunction is both consistent (ie. they match each other) and corresponds to a problem of interest, in this case approximating the inviscid problem. It is also important, when dealing with problems of this type solved with a method such as this, to balance computational efficiency with the various discretization parameters. In particular in this case the grid in y must be fine enough that it can resolve a small initial perturbation (the parameter Δy effectively places a lower bound on the amplitude ϵ of the initial perturbation). The time steps Δt also need to be chosen carefully with a view to being small enough to be accurate and capture all phenomena of interest, but large enough that the computational effort required is not unnecessarily onerous. An additional consideration is the choice of the viscosity and diffusivity parameters. Although both of these have a physical interpretation, it is nevertheless the case that choosing these parameters too small may result in the system of implicit equations (3.5.4)–(3.5.8) becoming ill-conditioned.

3.6. Choice of initial conditions for viscous model

Care must be taken in choosing the initial conditions for the viscous model. There are several features that are desirable. The initial conditions must mimic the

inviscid model closely enough that the two are comparable; it is intended that the same situation will be modelled here as was done using the techniques of sections 3.2–3.4. Additionally, the initial profiles for streamfunction and vorticity must be self-consistent. To achieve this, care must be taken that the Poisson equation (3.5.1) is initially satisfied to a high degree of accuracy.

As with the inviscid model it is helpful here to consider first an unperturbed case, a base flow, which will then have a perturbation added to it to obtain the case of interest. It is relatively simple to choose a stratified density profile that is a close approximation to the two incompressible layers of the inviscid problem. The profile chosen is

$$\rho(x, y, 0) = \frac{D+1}{2} + \frac{D-1}{2} \tanh(Sy) \quad (3.6.1)$$

where a scaled hyperbolic tangent in the vertical direction is used to mimic the two incompressible layers. Here D is a density ratio, as before, and a steepness parameter S has been introduced to control the rapidity of the density change across the ‘interface’ at $y = 0$. A piecewise profile could be used here, and although this would be an exact match for the inviscid case, such a choice has disadvantages in this context. In particular it would make the choice of a corresponding initial vorticity unattainable, as the interfacial region has no width and hence an infinite vorticity.

A hyperbolic tangent profile is also used as the basis to define the other components of the initial condition. As in the inviscid case, the base flow has a zero vertical velocity component and here the horizontal component is

$$u(x, y, 0) = \frac{F_1 + F_2}{2} + \frac{F_1 - F_2}{2} \tanh(Sy) \quad (3.6.2)$$

in which the Froude numbers F_1 and F_2 are as defined previously, and the steepness parameter S is as in equation (3.6.1). Having specified a velocity profile the corresponding streamfunction may be calculated by integrating with respect to y ,

thus obtaining

$$\psi(x, y, 0) = \frac{F_1 + F_2}{2}y + \frac{F_1 - F_2}{2S} \ln(\cosh(Sy)) + \psi_0$$

where ψ_0 is a constant chosen so that $\psi = 0$ at $y = -1$. A vorticity profile that exactly matches (3.6.2) is calculated from the definition of vorticity, namely $\zeta = \partial v / \partial x - \partial u / \partial y$, leading to

$$\zeta(x, y, 0) = -\frac{(F_1 - F_2)S}{2} \text{sech}^2(Sy). \quad (3.6.3)$$

It is this hyperbolic secant profile in vorticity that will be perturbed to give the desired initial conditions. The initial conditions for streamfunction and both velocity components are then calculated to match the perturbed vorticity.

The initial perturbed density profile is obtained by adjusting the argument of the hyperbolic tangent in (3.6.1) so that instead of its point of inflection being about $y = 0$ it is now about some initial interfacial profile $y = f(x)$. For the simplest case of an initial small amplitude sinusoid, with $f(x) = \epsilon \sin(kx)$, this leads to an initial density of

$$\rho(x, y, 0) = \frac{D+1}{2} + \frac{D-1}{2} \tanh(S(y - \epsilon \sin(kx)))$$

where the parameters ϵ , the perturbation amplitude, and the wavenumber k may be adjusted as necessary. In a similar fashion the initial vorticity is chosen to be

$$\zeta(x, y, 0) = -\frac{(F_1 - F_2)S}{2} \text{sech}^2(S(y - \epsilon \sin x)) \quad (3.6.4)$$

with the base flow vorticity (3.6.3) being adjusted in a similar way to the density profile. This effectively gives a layer of vorticity that has both finite width and a maximum that varies sinusoidally. The strength and sharpness of this profile may be adjusted by varying the Froude numbers and the steepness parameter.

Several approaches might be used to obtain a matching streamfunction. It is possible to use, for instance, the Peaceman-Rachford approach outlined in section

3.5 to solve the Poisson equation and thus get the desired profile. In practice, however, doing so is inefficient and surprisingly computationally intensive. A preferable approach, and the one that will be used here, is to obtain a Fourier series representation of the initial vorticity which is then integrated to obtain the corresponding streamfunction, giving a highly accurate solution to the Poisson equation. The appropriate double Fourier series representation is

$$\begin{aligned} \zeta(x, y, 0) = & -\frac{(F_1 - F_2)S}{2} \sum_{q=1}^N \left[A_{0q} + \sum_{p=1}^M A_{pq} \cos(pkx) \right. \\ & \left. + B_{pq} \sin(pkx) \right] \sin\left(\frac{\pi q}{h+1}(y+1)\right) \end{aligned} \quad (3.6.5)$$

which becomes exact as both M and $N \rightarrow \infty$. The two expressions for vorticity may be equated and Fourier analyzed in the usual fashion to get expressions for the series coefficients. These are

$$\begin{aligned} A_{pq} &= \frac{2k}{\pi(h+1)} \int_0^{2\pi/k} \int_{-1}^h g(x, y) \cos(pkx) \sin\left(\frac{\pi q}{h+1}(y+1)\right) dy dx \\ B_{pq} &= \frac{2k}{\pi(h+1)} \int_0^{2\pi/k} \int_{-1}^h g(x, y) \sin(pkx) \sin\left(\frac{\pi q}{h+1}(y+1)\right) dy dx \\ A_{0q} &= \frac{k}{\pi(h+1)} \int_0^{2\pi/k} \int_{-1}^h g(x, y) \sin\left(\frac{\pi q}{h+1}(y+1)\right) dy dx \end{aligned}$$

where the function $g(x, y) = \text{sech}^2(S(y - \epsilon \sin kx))$ has been defined for convenience of notation. The streamfunction ψ is determined by substituting the series representation of vorticity (3.6.5) into the Poisson equation. By assuming the boundary condition on the upper wall is the same as that of the base flow, the appropriate series representation for streamfunction is

$$\begin{aligned} \psi(x, y, 0) = & \frac{F_1 + F_2}{2} (y+1) - \frac{(F_1 - F_2)S}{2} \sum_{q=1}^N \left[\frac{1}{\beta_q^2} A_{0q} \right. \\ & \left. + \sum_{p=1}^M \frac{1}{\alpha_{pq}^2} (A_{pq} \cos(pkx) + B_{pq} \sin(pkx)) \right] \sin(\beta_q(y+1)) \end{aligned} \quad (3.6.6)$$

with $\beta_q = \pi q/(h+1)$ and $\alpha_{pq}^2 = k^2 p^2 + \beta_q^2$. This representation also satisfies the boundary conditions at the wall, where at the bottom wall $\psi = 0$ and at $y = h$,

the top wall, the streamfunction has the constant value $\psi = (F_1 + F_2)(h + 1)/2$. Sufficient accuracy is obtained by evaluating all integrals with a Gauss-Legendre quadrature scheme (as made available by von Winckel [63]) using 201 grid points in both the x and y directions, with all series truncated at $M = N = 101$ coefficients. To ensure complete consistency the vorticity and velocity components are then recalculated from (3.6.6) for use in the finite difference scheme of section 3.5.

3.7. Results

In sections 3.2–3.6 several approaches were used to model the Kelvin-Helmholtz problem. The inviscid model was solved using both a linear and non-linear scheme, whilst a viscous model that is comparable, but not identical, to the inviscid approach was solved using ADI methods. The focus of the results presented will be on comparing the behaviour of the three approaches. It is expected that the two inviscid solutions will match closely for early times before diverging as the non-linear effects begin to dominate. Although a similar comparison may be made between the viscous and inviscid models, this is expected to be more qualitative in nature. This is because there are several critical points of difference in the initial conditions for the two schemes (the velocity fields, for instance) and as such they will develop in similar, but noticeably different ways. Although the respective growth rates of the inviscid and viscous models may be slightly different, their solutions should evolve in a similar enough way that a comparison between the two will be instructive.

The behaviour of both models is dependent upon a large number of parameters. It is not the intention of this study to examine exhaustively the effect of each of these on the evolution of the solution; instead, representative cases will be chosen with a view to capturing the behaviour of interest. Only cases that are unstable, as determined by the inviscid stability criterion (3.3.9), will be considered. By first choosing wavenumber k , density ratio D and upper layer height h , it is straightforward to select corresponding Froude numbers so that the system is unstable to small perturbations. These choices will be used for the inviscid model, as well as

the initial condition of the viscous model. To allow easy comparison to the inviscid model the critical parameters of the viscous model, the diffusivity σ and viscosity ν , will be chosen to be small, meaning that the fluid is nearly inviscid and the two viscous layers will mix slowly. The size of the perturbation to be used is limited by the choice of grid size for the viscous model; specifically, the initial sinusoidal perturbation must have an amplitude that is no smaller than $5\Delta y$, since smaller perturbations would be lost in sub-grid-scale noise. Similarly, the size of the grid limits the choice of the steepness parameter in the viscous initial condition. Choosing too large a steepness may result in the width of the interfacial region falling below the grid scale, meaning that the rapid changes (at the interfacial region) in the initial condition appear piecewise rather than smooth. The key here is to choose a value such that the initial vorticity is large, but the interfacial region is still narrow enough that it may be legitimately thought of as an interface.

Two cases will be considered in detail. For both of these a number of parameters will be fixed, as mentioned above. For both inviscid and viscous models the wavenumber will set at $k = 1$, the density ratio as $D = 0.99$ and the upper layer height at $h = 1$. Additionally the parameters used in the viscous model are the viscosity $\nu = 1 \times 10^{-5}$ and the diffusivity $\sigma = 1 \times 10^{-5}$.

The first case to be considered involves equal but opposite currents with $F_1 = 0.2$ and $F_2 = -0.2$. This is unstable according to the linear stability criterion (3.3.9), but its growth rate is only modest, thus providing a good balance in terms of achieving large enough growth within a reasonable time. The second case will use the same basic parameters but with $F_1 = 0.1$ and $F_2 = 0.5$, so that both layers flow in the same direction. Linear theory predicts that for this case the interface will be an exponentially growing travelling wave and it is anticipated that the non-linear version will look similar to the first case, but travel as it grows. This choice has been made to emphasize the built-in periodicity of the ADI solution technique. As both cases have an identical difference in their two Froude numbers, that is $|F_1 - F_2| = 0.4$, it is anticipated that they will grow at the same rate. Indeed the

only difference should be that the second case travels as it grows, whereas the first case will be stationary.

3.7.1. The case $F_1 = 0.2$, $F_2 = -0.2$. A commonly studied version of this problem is where the two layers flow with equal but opposite speeds. In the Birkhoff-Rott formulation [8], the choice is effectively $F_1 = 0.5$ and $F_2 = -0.5$ in the variables of this study. The blow-up of higher order modes in the non-linear inviscid scheme is too rapid with this choice of Froude numbers, and so the more moderate values of $F_1 = 0.2$ and $F_2 = -0.2$ are used here instead. These values still give a highly unstable system and should allow the interface to evolve to a point where the behaviour of interest may be seen. The initial perturbation size is chosen to be quite large at $\epsilon = 0.05$ so that the same perturbation may be used in both the inviscid and viscous schemes.

The first comparison to be made is between the linearized and non-linear inviscid models. Obtaining a solution to the linearized version of the problem is straightforward, only requiring parameter values to be substituted into various expressions from section 3.3. For the purpose of comparison here it will be assumed that the initial perturbation is purely sinusoidal so that, in the notation of section 3.3, $Q_{10} = 0.05$ and $P_{10} = 0$. The resulting solutions for the interface height function and the two velocity potentials may then be computed at any time from their definitions (3.3.6)–(3.3.8). For an unstable choice of parameters such as this, the interface height function is simply an exponentially growing sine wave. The choice of equal but opposite Froude numbers means that the wave does not travel as it grows.

Obtaining the corresponding non-linear solution is more computationally intensive. The choice of initial condition is identical to that used in the linearized solution, as set out in section 3.4.1, and as such it is expected that both models will evolve in a similar fashion, at least for early times. It is known that the inviscid interface will, after some finite time, develop a curvature singularity [42] and as

such it is anticipated that the model will break down at this point, typically near where the interface develops a region that is near vertical.

Figure 3.2 shows a comparison between the predictions of linear theory (dashed line) and the corresponding non-linear results (solid line) for the inviscid model, up to the time $t = 7.35$ at which the curvature singularity forms. The non-linear and linear solutions coincide for early times, as shown in figure 3.2(b) for $t = 2$. By $t = 4$ both solutions have grown to about the same height (approximately double that of the initial condition), but the non-linear solution has begun to skew slightly to one side as the non-linearity starts to have some visible effect. This leaning of the interface towards the centre continues as the solution evolves, and at the later computed times, shown here for $t = 6$ and $t = 7$ in figures 3.2(d) and 3.2(e), respectively, the peak of the non-linear wave is now significantly to the right of the peak of the linear solution and the trough of the non-linear wave has moved to the left of the corresponding point on the linear wave. The net result is that the region in the centre of the non-linear interface has become steep, to the point that it is close to being vertical. A short time after this the method starts to break down. At the final computed time $t = 7.35$, shown in figure 3.2(f), the non-linear interface is almost vertical near its centre and has begun to develop high order ‘wiggles’, where the resolution of the Fourier series is at its limits and the interface now visibly displays some Gibbs’ phenomenon behaviour [34].

All the non-linear solutions shown here were computed with $N = 51$ coefficients in each Fourier series, with all the intermediate integrals evaluated using 1601 grid points. Several computational difficulties were encountered, mainly involving the spurious blow-up of higher order modes. A number of strategies were used to counter this, namely the smoothing scheme of section 3.4 and using a lower order solution at an intermediate time (usually evaluated less accurately with 21 coefficients) to bootstrap up to the full solution.

It is instructive to study the curvature of the interface at various points in its evolution. The aim here is to confirm that a singularity in curvature does, in fact,

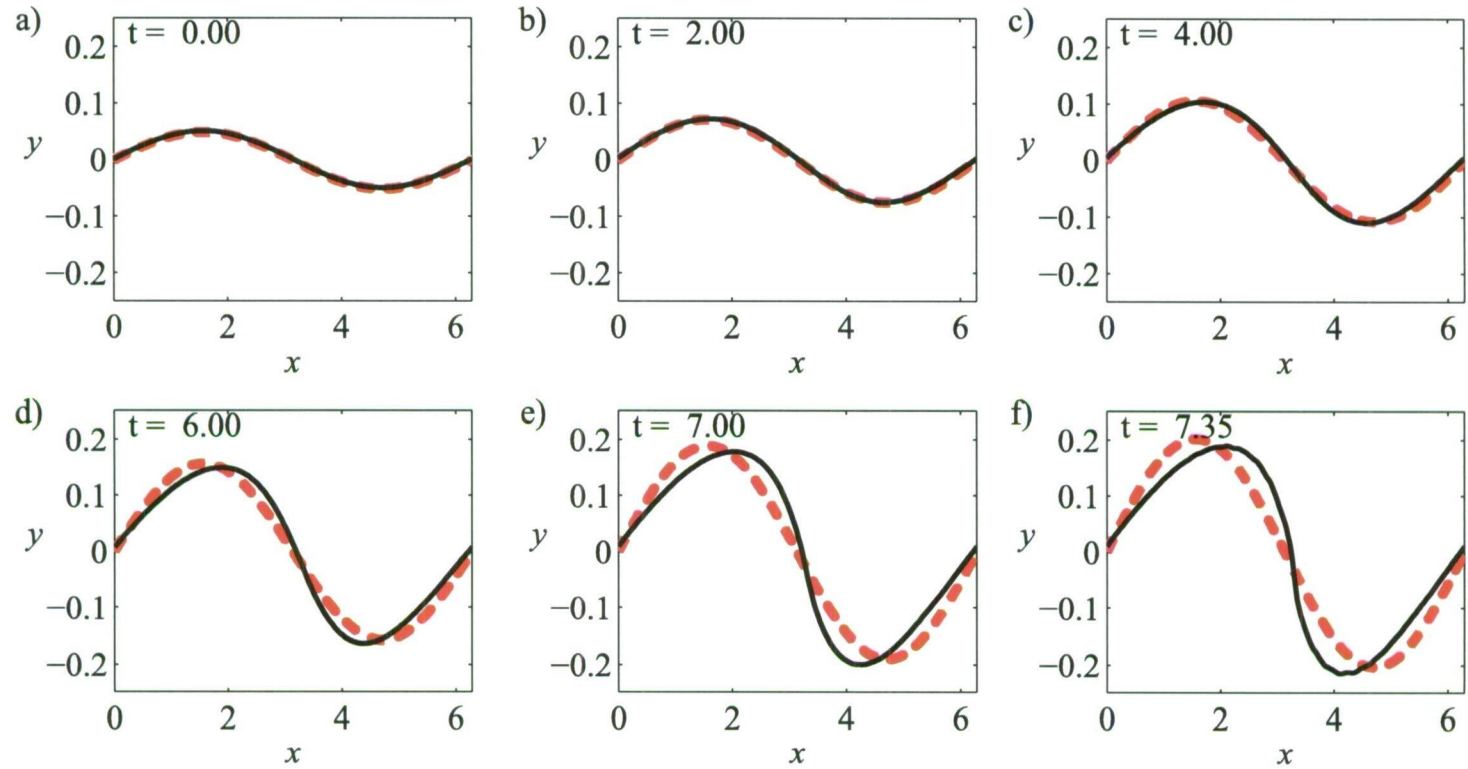


FIGURE 3.2. Evolution of the inviscid interface for the case $F_1 = 0.2$, $F_2 = -0.2$, for both the linearized (dashed line) and fully nonlinear (solid line) solutions. Figures 3.2(a)–(f) show the times $t = 0, 2, 4, 6, 7$ and 7.35 , respectively.

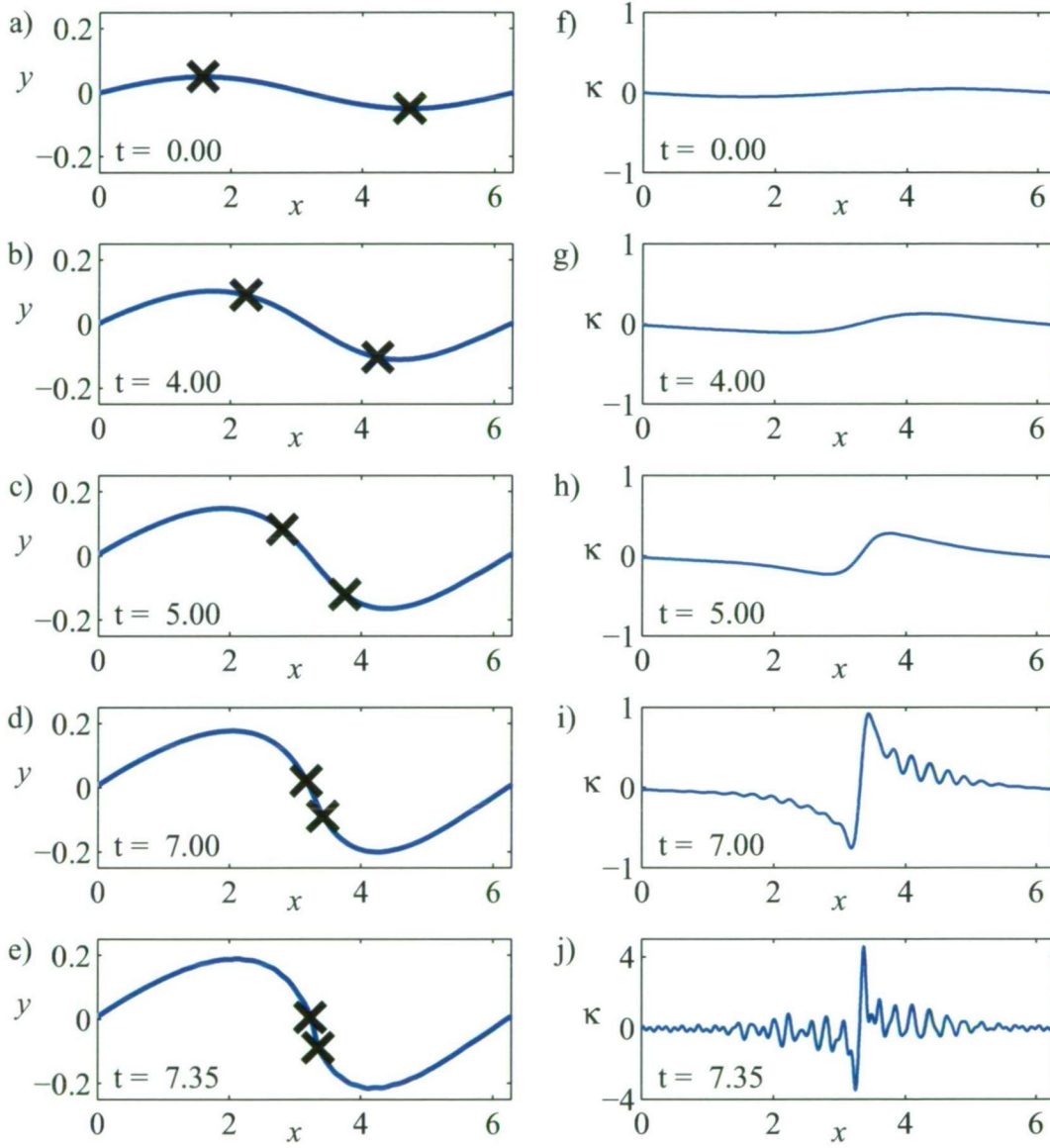


FIGURE 3.3. Comparison of interface shape and curvature for the case $F_1 = 0.2$, $F_2 = -0.2$, where interfacial profiles are shown at selected times in figures 3.3(a)-(e) and the corresponding curvature for the same times is shown in figures 3.3(f)-(j). The heavy crosses in figures 3.3(a)-(e) mark the maximum and minimum points of curvature.

form in finite time and that this coincides with the last times that the non-linear method was able to compute. Curvature may be calculated at any point on the interface using the formula

$$\kappa(x, t) = \frac{\partial^2 \eta / \partial x^2}{1 + (\partial \eta / \partial x)^{3/2}}.$$

Interest lies in the points of maximum and minimum curvature. Figures 3.3(a)–(e) show the interface height function for the five times $t = 0, 4, 6, 7$ and 7.35 and the corresponding curvatures these times is shown in figures 3.3(f)–(j). The last of pair of these plots (figures 3.3(e) and (h)) represent the solution for the point at which the inviscid model failed. On the plots of the interface height function the large crosses mark the maximum and minimum points of curvature respectively. Initially, the points of large curvature lie at the peak and trough of the wave, as shown in figure 3.3(a). As the solution evolves, these large curvature points move closer together towards the central portion of the wave, so that by $t = 6$ both the maximum and minimum points of curvature lie on a section of the wave that is near vertical and appears to be locally linear. At the last computed time $t = 7.35$, the points of high curvature lie very close. The proximity (in the x direction) of the maximum and minimum points is limited by the number of coefficients used in each series, in this case $N = 51$, and the curvature (shown in figure 3.3(j)) at the last computed time, for instance, is dominated by the contribution for the 51st coefficient, with the central peaks effectively being a result of the large contribution from the highest mode. Here it is clear that the points of large positive and large negative curvature are close to each other, in the way that a singularity might be represented with Fourier series methods. The values of curvature here are $\kappa \approx 4$ which is large in this context, and certainly very much larger than the initial values.

The same parameter values are used for the viscous model. Sufficient accuracy is obtained by using $M = 200$ and $N = 400$. This gives a grid spacing in y of $\Delta y = 5 \times 10^{-3}$, which means that the size of the perturbation is large enough in comparison to the size of the grid that the model will be able to resolve it. With

similar considerations in mind, the steepness parameter is set at $S = 40$ in equation (3.6.4). An initial condition is created using the methods of section 3.6, here using 101 coefficients in both directions with 201 Gauss-Legendre integration points. The resulting initial streamfunction and vorticity satisfy the Poisson equation (3.5.1) to a very high degree of accuracy. The ADI method is used to advance the solution. Time steps of $\Delta t = 1 \times 10^{-3}$ are used from $t = 0$ to $t = 1$ with time steps of $\Delta t = 1 \times 10^{-2}$ being used thereafter.

Several solutions for vorticity at various times are shown in figure 3.4, with the corresponding density profiles shown in figure 3.5. Density and vorticity will be discussed primarily here as they show best the evolution of the diffuse interface, but for completeness the streamfunction and velocity components at the moderate time $t = 15$ are given as an example in figure 3.6. As may be seen from figure 3.4 and figure 3.5 the solutions of vorticity and density evolve in an extremely similar manner. For early times the diffuse interface behaves just like the inviscid case, appearing at first to be an exponentially growing sinusoid, before developing a degree of non-linearity and by $t = 13$ has approached a similar profile to the last computed profile of the inviscid model. The discrepancy in the time for the two models to reach this point is due to the slight differences in the initial conditions and is to be expected.

The viscous model allows the evolution of the interface to be followed past the point where the inviscid model broke down. After this time, the viscous interface develops a small overhanging portion near its centre. A detail of this breaking is shown in figure 3.7, plotted with the single density contour $\rho = 0.995$ for clarity. This point of breaking is analogous to the formation of a curvature singularity in the inviscid model. It is of interest that there is a patch of large negative vorticity at this point, indicating that the region in question is highly rotational. Once the interface has turned over it continues to grow in amplitude. In this configuration there is light fluid from the upper layer lying underneath heavier fluid from the lower layer. This itself represents a further (Rayleigh-Taylor) instability as discussed by

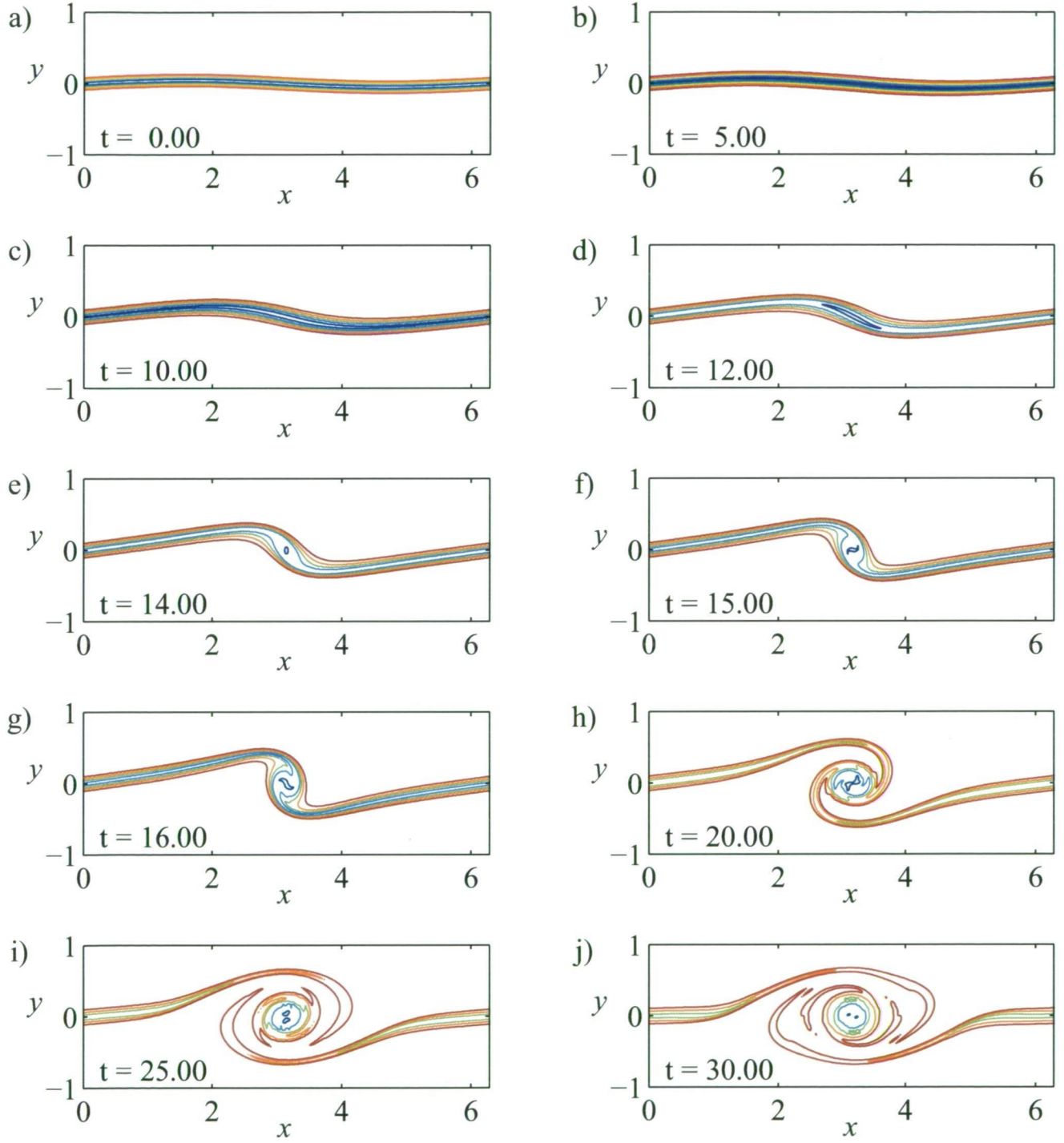


FIGURE 3.4. Evolution of vorticity in the viscous model for the case $F_1 = 0.2$, $F_2 = -0.2$ displayed as contours for a selection of times between $t = 0$ and $t = 30$.

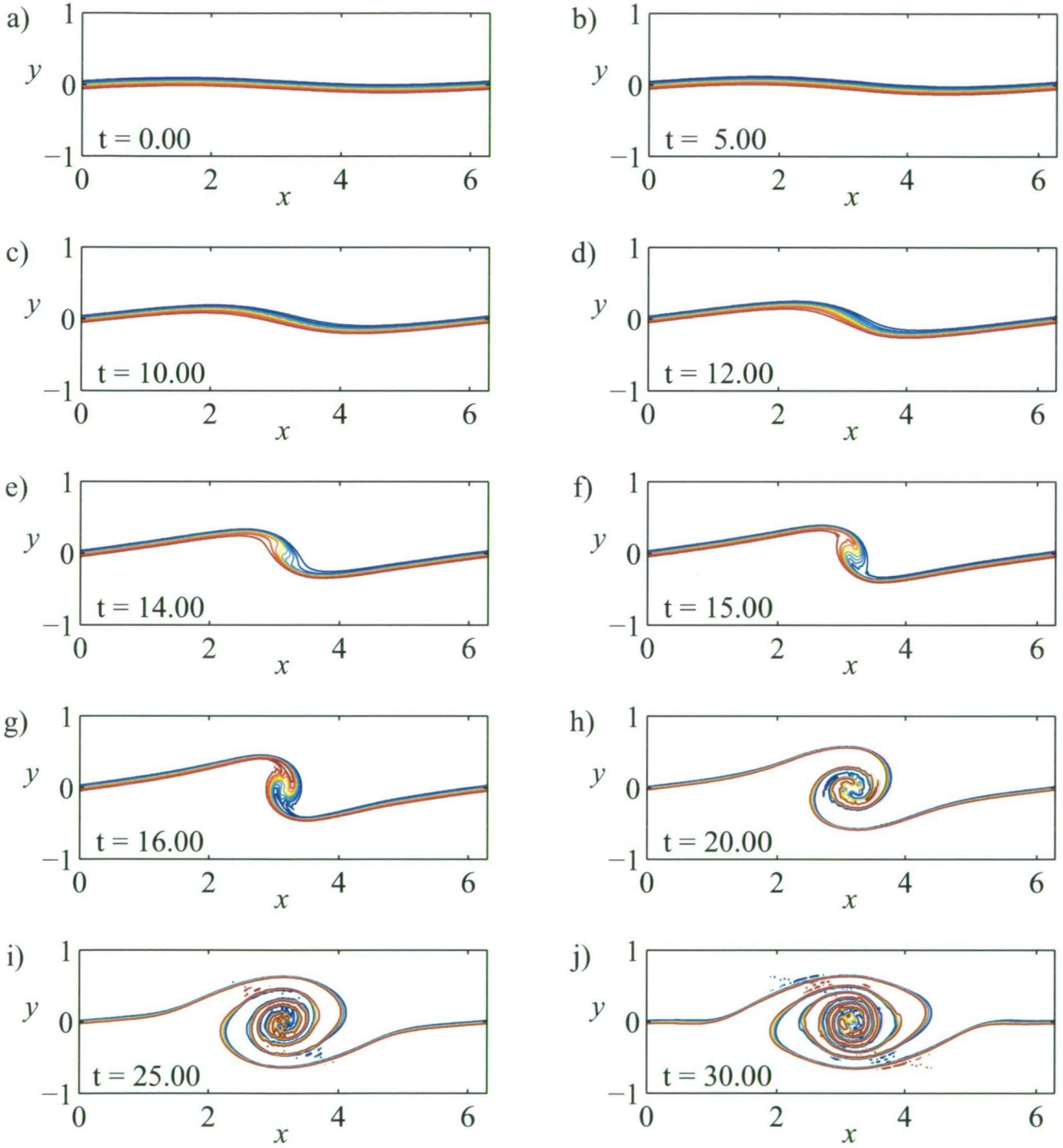


FIGURE 3.5. Evolution of density in the viscous model for the case $F_1 = 0.2$, $F_2 = -0.2$ displayed as contours for a selection of times between $t = 0$ and $t = 30$.

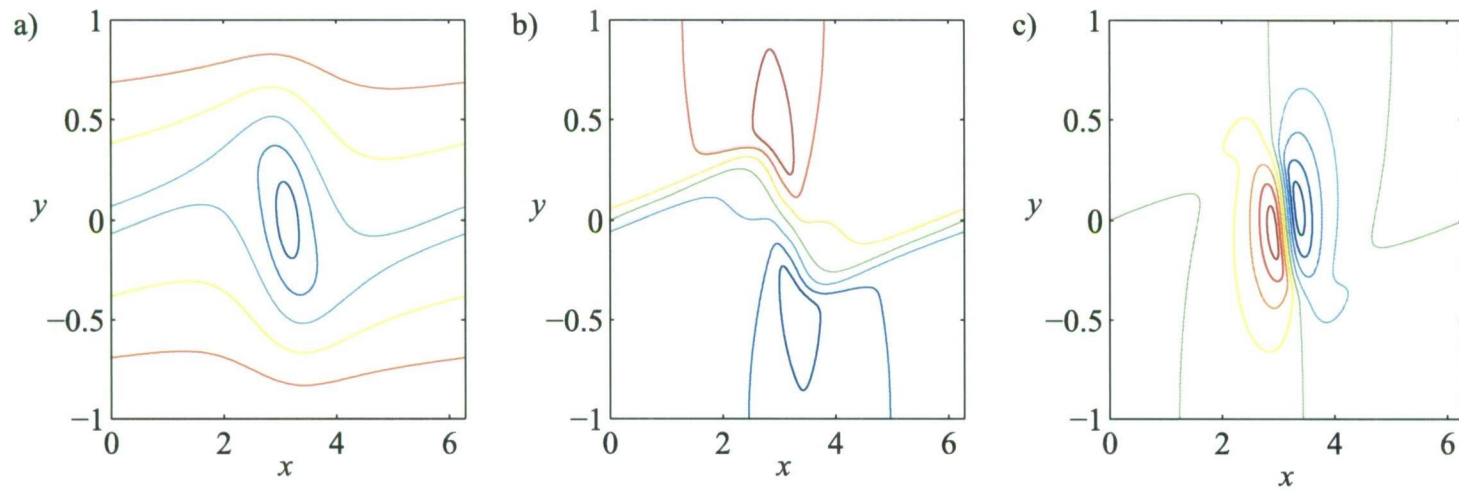


FIGURE 3.6. Contour plots of streamfunction and velocity components from the viscous model at $t = 15$ for the case $F_1 = 0.2$, $F_2 = -0.2$.

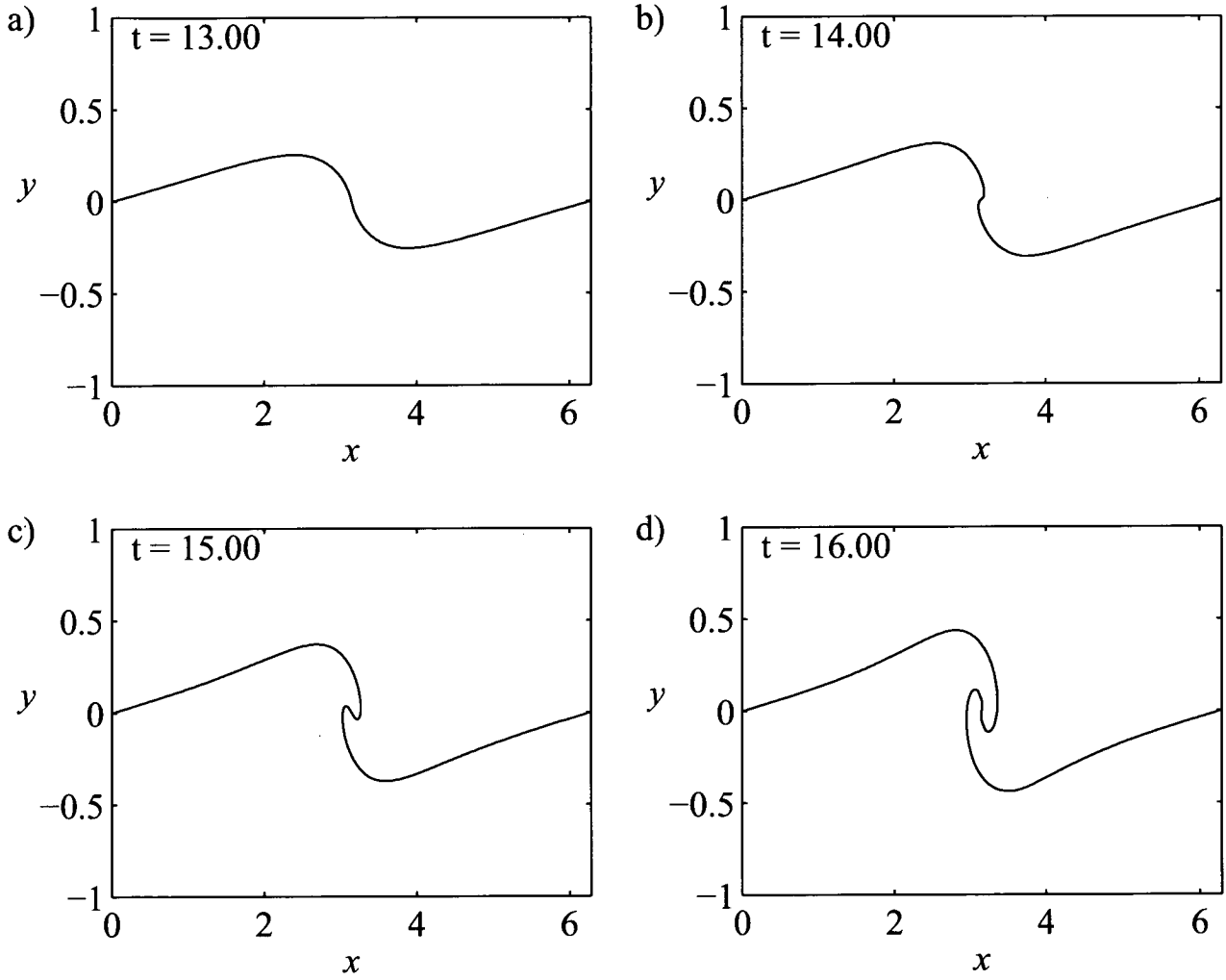


FIGURE 3.7. Plots of a single contour of density $D = 0.995$ for the case $F_1 = 0.2$, $F_2 = -0.2$. The four time steps shown here, $t = 13, 14, 15$ and 16 , illustrate the crucial point at which the density profile overturns.

Forbes [24]. A short time later, fingers of each of the two fluids protrude into the other fluid and they begin to curl back on themselves. As that happens again a combination of buoyancy effects and the fluids' relative motion lead to repeating and the effects cascade, meaning that the interface starts to spiral in the typical manner of interfacial roll-up. The spirals become more and more tightly wound and

the interface continues to evolve past the last time step shown here, although the spirals will eventually become finer than the grid size. This has already happened to some extent in the centre of the roll-up where, at later times, the fluids have effectively mixed.

3.7.2. The case $F_1 = 0.1$, $F_2 = 0.5$. For completeness, a case where the two Froude numbers are not of equal magnitude will now be investigated. All other parameters remain the same as in the case discussed in section 3.7.1, but the Froude numbers are changed to $F_1 = 0.1$ and $F_2 = 0.5$. Only the viscous solution will be shown here to highlight the built-in periodicity of the ADI method. Several vorticity profiles at different times are shown in figure 3.8. The evolution of this solution is nearly identical to that of the previous case (notably this case overturns at a slightly later time), with a small amplitude sinusoid again growing exponentially at early times and rolling up into a tight spiral by $t = 30$. The clear difference between this and the previous case is that here the solution travels as it evolves. Although not unexpected, the close similarity between two cases with the same absolute difference in Froude numbers is shown very clearly here. These results also agree qualitatively with the linearized theory of section 3.3, since that analysis gave a linear travelling wave when the Froude numbers used were not equal and opposite.

3.8. Conclusion

The Kelvin-Helmholtz instability was modelled for both inviscid and viscous fluids. A linearized perturbation analysis was performed on the inviscid model, modifying the classic problem to include horizontal walls above and below the unstable interface. Non-linear solutions to the inviscid model were then computed using a Fourier series technique developed for the study of Rayleigh-Taylor waves by Forbes, Chen and Trenham [25] and, although a number of computational difficulties were encountered, some well-known features of Kelvin-Helmholtz waves were reproduced. This included the appearance of a finite time curvature singularity on

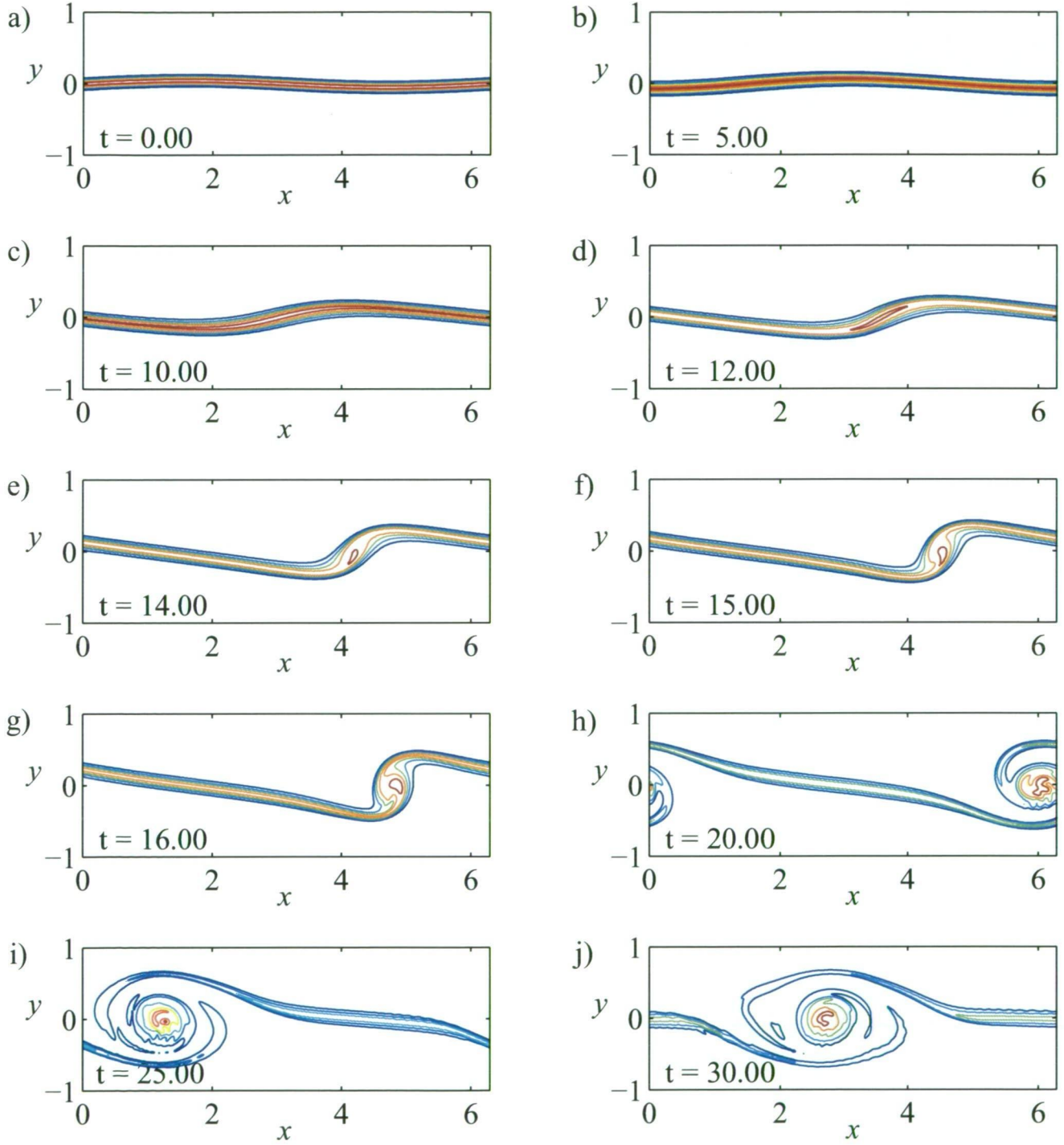


FIGURE 3.8. Evolution of vorticity in the viscous model for the case $F_1 = 0.1$, $F_2 = 0.5$ displayed as contours for a selection of times between $t = 0$ and $t = 30$. Here the solution evolves in a similar fashion to the case shown in figure 3.3, with the added feature that this wave travels to the right as it grows.

the interface, as predicted by Moore [42] and others, and a short time after this occurs the solution technique breaks down. For earlier times strong agreement was seen between the linearized and non-linear solutions where the interface is essentially an exponentially growing linear wave.

Although the viscous model of sections 3.5–3.6 does not evolve at exactly the same rate as the inviscid model (owing to subtle differences in initial conditions), there are a several valuable points of comparison to be made between the two. For early times, both grow in a similar fashion. At the point where the viscous interface overturns (analogous to the formation of the curvature singularity) a patch of large vorticity appears at the point on the interface where the inviscid curvature singularity was. The finite width ‘interface’ then rolls up around this highly rotational point, eventually forming a tightly wound spiral. It may be possible in a future study to refine the choice of initial condition further so that the behaviour of the viscous model more closely matches that of the inviscid scheme.

Much care was taken in the inviscid scheme to damp growth of unstable high order modes. This was fairly successful, although even with use of the various smoothing techniques the computational stability of the solution is very sensitive to the choice of parameter values. In particular the Froude numbers F_1 and F_2 (and to some extent the wavenumber k) must be chosen with care.

Similarly for the viscous model most of the computational effort was put into solving the Poisson equation (3.5.1) to a high degree of accuracy. The convergence of that method was highly sensitive to the sequence of quasi-time steps $\Delta\tau$ used and several robust choices were outlined; their use meant that the desired degree of accuracy could be achieved relatively efficiently. This computationally intensive procedure is a by-product of the choice to use a vorticity-streamfunction formulation. Despite this, the advantages of such a formulation (over using primitive variables) for this problem, and in particular the direct of computation of vorticity, make incurring such a computational cost acceptable.

CHAPTER 4

Waves in two-layer shear flow for viscous and inviscid fluids

4.1. Introduction

As has already been seen in chapters 2 and 3, the presence of shear in fluid flow is associated with a variety of wavelike behaviours. The focus of this chapter will shift to examining the effect a finite amount of shear may have on stratified flows and on fluid interfaces. Mechanisms for the generation of shear are often found in viscous flow, for instance in boundary layers or in the flow between moving plates, and similar effects are possible in rotational inviscid flow. Since shear is essentially a measure of spatial velocity gradient, it is often convenient to describe or treat these types of flows in terms of vorticity. For example, the linear velocity profile established between two moving plates (plane Couette flow) may be described as having constant vorticity. Such a description is particularly useful in dealing with wavelike behaviour or periodic disturbances, an example of which is the treatment of co-rotating vortices by Saffman [50].

Pullin and Grimshaw [48] calculated numerous large amplitude steady waves, including some with limiting features such as corners, on a two layer inviscid flow with shear in the lower layer. Similarly, in chapter 2 of this thesis numerous steady waves were computed on a free shear layer and these featured a variety of resonant interactions between wave modes. Standing waves are often studied in the context of water waves; these are discussed in terms of their associated vorticity in Ehrnstrom and Wahlen [20].

A number of shear flows are unstable to small perturbations. Two examples of these are the Kelvin-Helmholtz and Holmboe instabilities. In the Kelvin-Helmholtz

instability two fluid layers flow past each other so that there is a thin region of infinite shear at their common boundary. This was studied for both viscous and inviscid fluids in chapter 3 where the predicted growth of the wave and the formation of a cat's-eye spiral were seen at the interface. In the Holmboe instability the shear is spread over a layer of finite width and, as presented by Umrhan and Heifetz [61], this flow configuration permits a variety of solution modes, including travelling and standing waves. The stability of a variety of different shear flows are investigated in Criminale and Drazin [18], although the focus there is on perturbing some base vorticity or velocity profiles in a few very specific ways. The flow presented in this chapter will typically be perturbed by giving the interface between the layers a sinusoidal disturbance.

Two fluid layers of slightly different densities, bounded above and below by rigid walls, will be considered in this chapter. The lower layer is denser than the upper so that the flow is buoyantly stable. When unperturbed, each layer flows with constant vertical shear. The amount of shear in each layer may differ, but the associated horizontal velocity is chosen so that it is continuous across the interface between the fluids. There are two cases here that are of particular interest: the case where both layers flow with equal amounts of shear and the case where one layer has no shear.

Two versions of this flow will be considered: one that assumes both fluid layers are inviscid and one that includes the effects of viscosity. The inviscid version will be based on a classical description of a two-layer incompressible fluid, with an infinitely thin interface separating the two layers. By contrast, the viscous version of the flow will feature a continuously stratified, weakly compressible fluid, albeit one that mimics the layered fluid of the inviscid case. The interface (or quasi-interface) in each of these two flows will be given a small sinusoidal perturbation (thus perturbing both density and velocity) and the subsequent behaviour of the wave in the interfacial region will be the focus of the work in this chapter.

The two different formulations of the flow are introduced in section 4.2 and care has been taken to ensure that these match each other as closely as possible. This enables direct comparison so that the effects of viscosity may be assessed as in Forbes [24]. Both formulations are then studied using linearization techniques; the assumption here is that, once perturbed, the evolving flow does not change too far from the base flow. In section 4.3 this is achieved by approximating the fully non-linear governing equations of the inviscid problem with their linearized equivalents. Similarly, the viscous formulation is carefully analyzed using perturbation series techniques and a spectral solution is specified in section 4.4. Here much attention is given to choosing appropriate initial conditions so that the system is perturbed in a similar way to the inviscid problem. The results of these two solution techniques are compared in section 4.5, where a variety of solutions for different parameter values are presented. Notably these display a range of oscillatory behaviours, including standing waves, both damped and undamped. The validity of these solutions in the context of the solution technique for the viscous flow will be discussed.

4.2. Model formulation

The flow to be considered consists of two horizontal fluid layers of different densities. The upper fluid is denoted as layer 1 and the lower fluid is layer 2; quantities associated with each layer are subscripted accordingly. These layers are in motion with a continuous horizontal velocity profile, such that the speed at the interface of the two layers is c_0 and each layer flows with constant vertical shear, namely ω_1 in the top layer and ω_2 in the lower layer; hence the base horizontal speeds of each layer are $u_1 = c_0 - \omega_1 y$ and $u_2 = c_0 - \omega_2 y$, respectively. There is thus a sharp change in both density and vorticity about $y = 0$, although the horizontal speed is continuous here. Walls are present above and below the interface, at $y = h_1$ and $y = -h_2$, respectively. A schematic diagram of the flow configuration is shown in figure 4.1.

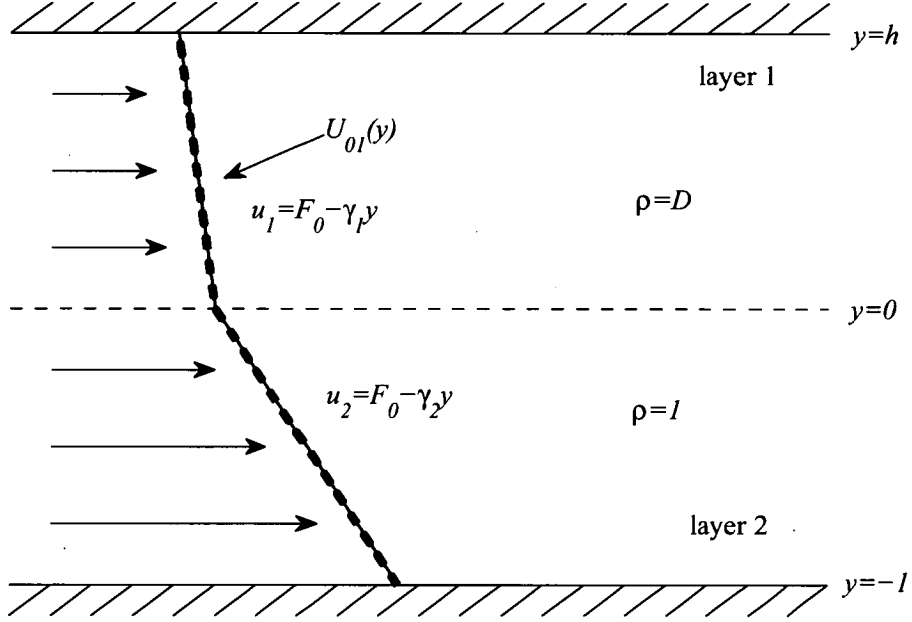


FIGURE 4.1. Schematic of the two-layer shear flow. The heavy dashed line shows the continuous horizontal velocity profile $U_{0l}(y)$ used in the viscous formulation, while the thin solid line is the horizontal profile for the inviscid case.

Non-dimensional variables will be introduced for convenience. The length scale is chosen to be the depth of the lower layer h_2 . It follows that an appropriate choice for the speed scale is $\sqrt{gh_2}$ and similarly the time scale to be used is $\sqrt{h_2/g}$. The lower layer density ρ_2 is used to scale density. This gives a number of key dimensionless parameters, namely a Froude number $F_0 = c_0/\sqrt{gh_2}$, two dimensionless measures of shear $\gamma_1 = \omega_1\sqrt{h_2/g}$ and $\gamma_2 = \omega_2\sqrt{h_2/g}$, a density ratio $D = \rho_1/\rho_2$ and the dimensionless height of the upper layer $h = h_1/h_2$. This set of five parameters will be used for both the inviscid and viscous formulations presented below.

There will be a few key choices for these parameters. In particular, interest lies in investigating the effect of changing the strength of the shear parameters γ_1 and γ_2 in each layer. The case of equal shear, that is where $\gamma_1 = \gamma_2$, will be studied

first. The stability of a similar flow with a continuously stratified density profile (and only the lower wall) was examined by Chandrasekhar [11, article 103a]. In viscous fluids, shear flows of this type are often referred to as plane Couette flow (see, for instance, Drazin & Reid [19, chapters 4 and 5] for various approaches to the viscous problem or Case [10] for an investigation of the stability of the equivalent inviscid flow), namely the flow induced between moving plates. The next step is to consider the related case of $\gamma_1 = 0$ and $\gamma_2 \neq 0$. A similar flow was studied by Pullin & Grimshaw [48] where numerous large amplitude steady waves (including over hanging waves) were computed and it is possible that steady waves of a smaller amplitude may be obtained here. In each of these cases the base flow will be given a small sinusoidal perturbation in both density and vorticity. It is the response to this disturbance and subsequent evolution of the flow, with particular emphasis on the interfacial region, that will be the focus of the study.

4.2.1. Inviscid formulation. The inviscid version of this problem involves two immiscible fluid layers flowing as described above. Both layers are assumed to be inviscid and incompressible. There is an interface between the layers lying at $y = 0$ when the system is unperturbed, and more generally the interface is represented by the function $y = \eta(x, t)$. This implies that the exact shape of the layers is not known a priori, and by the very nature of the problem the layers' shapes change as the interface evolves. The inclusion of shear means that the flow is inherently rotational; however, as only constant shear is considered it is possible to write the velocity as a sum of rotational and irrotational parts, thus allowing velocity potentials Φ_1 and Φ_2 to be constructed for the irrotational parts of the fluid motions in each layer. In the upper layer, between $y = \eta(x, t)$ and $y = h$, the velocity components are

$$\begin{aligned} u_1 &= F_0 - \gamma_1 y + \frac{\partial \Phi_1}{\partial x} \\ v_1 &= \frac{\partial \Phi_1}{\partial y} \end{aligned}$$

and similarly in the lower layer, between $y = -1$ and $y = \eta(x, t)$, the horizontal and vertical components of velocity are written as

$$\begin{aligned} u_2 &= F_0 - \gamma_2 y + \frac{\partial \Phi_2}{\partial x} \\ v_2 &= \frac{\partial \Phi_2}{\partial y}. \end{aligned}$$

The velocity potentials satisfy Laplace's equation in their respective regions, that is

$$\begin{aligned} \nabla^2 \Phi_1 &= 0 \quad \eta(x, t) < y < h \\ \nabla^2 \Phi_2 &= 0 \quad -1 < y < \eta(x, t) \end{aligned}$$

as is usual for incompressible inviscid fluids. Additionally, there are a number of boundary conditions to be defined on the interface. On either side of the interface it is required that the normal component of velocity is zero, leading to the condition that

$$\frac{\partial \eta}{\partial t} = v_i - u_i \frac{\partial \eta}{\partial x} \quad \text{on } y = \eta(x, t) \quad (4.2.1)$$

for $i = 1, 2$, so that the condition is applied in each fluid at the interface. A further condition is obtained by considering Bernoulli's equation and equating pressure on either side of the interface. The resulting dynamic condition is

$$\begin{aligned} \frac{\partial \Phi_2}{\partial t} - D \frac{\partial \Phi_1}{\partial t} &= \frac{1}{2}(1-D)F_0^2 - \frac{1}{2}(u_2^2 + v_2^2) + \frac{1}{2}D(u_1^2 + v_1^2) \\ &\quad - \gamma_2 \psi_2 + D\gamma_1 \psi_1 - (1-D)\eta \quad \text{on } y = \eta(x, t) \end{aligned} \quad (4.2.2)$$

where the streamfunctions ψ_1 and ψ_2 have been introduced in each layer as a consequence of allowing a constant shear in the layers. These are defined as

$$\psi_i = F_0 y - \frac{1}{2}\gamma_i y^2 + \Psi_i$$

for $i = 1, 2$, and here Ψ_i is the irrotational component of the streamfunction and relates to the velocity potentials via the Cauchy-Riemann equations; that is,

$\partial\Phi_i/\partial x = \partial\Psi_i/\partial y$ and $\partial\Phi_i/\partial y = -\partial\Psi_i/\partial x$. Also note that the complete streamfunction ψ_i reproduces the velocity components for $u_i = \partial\psi_i/\partial y$ and $v_i = -\partial\psi_i/\partial x$ by simple differentiation. Additionally it is required that the vertical component of velocity v is equal to zero at the top and bottom walls, $y = -1$ and $y = h$. The behaviour of this inviscid system when subjected to a small perturbation will be investigated in section 4.3.

4.2.2. Viscous formulation. To model the shear flow in a viscous compressible fluid, a modified version of the Navier-Stokes equations will be introduced. This is similar to the approach used by Farrow and Hocking [21] to model the flow of withdrawal from a tank, although the version presented here will use a vorticity-streamfunction formulation. An approach of this type has already been used to model the viscous version of the Kelvin-Helmholtz instability in chapter 3. There are several advantages to using such a formulation; in particular, it avoids the need to solve explicitly for pressure and allows the direct computation of vorticity. For the problem at hand this is particularly convenient as the defining parameters of the flow are the amounts of shear in each layer, which are themselves a measure of vorticity. It is assumed that the flow is Boussinesq so that, as in Farrow and Hocking [21], the density ρ may be written as the sum $\rho = \rho_0 + \bar{\rho}(x, y, t)$ of an average part ρ_0 and a time dependent component $\bar{\rho}(x, y, t)$, in which density does not vary greatly from the average ρ_0 . A consequence of using the vorticity-streamfunction approach is that density only ever appears as a derivative and as such it is possible to use ρ and $\bar{\rho}$ interchangeably. These assumptions are built into the approach of Farrow and Hocking [21] and the primitive variable system used there will now be extended by the introduction of a vorticity-streamfunction formulation.

Vorticity ζ is defined in terms of the horizontal and vertical velocity components as $\zeta = \partial v/\partial x - \partial u/\partial y$ and by taking the curl of the momentum equation in the primitive variable formulation it is possible to eliminate pressure. At the same time the continuity equation may be now written in terms of streamfunction, which may be introduced as the fluid is nearly incompressible, and this streamfunction

ψ relates to the velocity components by simple differentiation, that is $u = \partial\psi/\partial y$ and $v = -\partial\psi/\partial x$. The version of the Navier-Stokes equations that is derived as a consequence is

$$\frac{\partial^2 \psi}{\partial x^2} + \frac{\partial^2 \psi}{\partial y^2} = -\zeta \quad (4.2.3)$$

$$\frac{\partial \zeta}{\partial t} + u \frac{\partial \zeta}{\partial x} + v \frac{\partial \zeta}{\partial y} = \nu \left(\frac{\partial^2 \zeta}{\partial x^2} + \frac{\partial^2 \zeta}{\partial y^2} \right) - \frac{\partial \rho}{\partial x} \quad (4.2.4)$$

and the continuity equation of mass conservation takes the form

$$\frac{\partial \rho}{\partial t} + u \frac{\partial \rho}{\partial x} + v \frac{\partial \rho}{\partial y} = \sigma \left(\frac{\partial^2 \rho}{\partial x^2} + \frac{\partial^2 \rho}{\partial y^2} \right). \quad (4.2.5)$$

Here, the parameters ν and σ are an inverse Reynolds number and an inverse Prandtl number, respectively. These parameters control the amount of viscosity and the rate at which the fluids mix, that is the diffusivity, and in practice these values will be chosen so that the flow mimics the situation of the two inviscid immiscible fluid layers outlined in section 4.2.1.

As in the inviscid formulation it is necessary to define a background flow. The difference here is that continuous functions are required, as opposed to the piecewise profiles used in section 4.2.1, to avoid unintentionally introducing large spikes in derivatives and so on. A steepness parameter S is introduced to control the rapidity of the change of the variables across the interfacial region. To match the profiles of the inviscid version hyperbolic tangent functions are used for both density and vorticity. The appropriate forms for these are

$$R_{01}(y) = \frac{D+1}{2} + \frac{D-1}{2} \tanh Sy \quad (4.2.6)$$

$$\Omega_{01}(y) = \frac{\gamma_1 + \gamma_2}{2} + \frac{\gamma_1 - \gamma_2}{2} \tanh Sy \quad (4.2.7)$$

where the functions $R_{01}(y)$ and $\Omega_{01}(y)$ are introduced as background density and vorticity respectively. It is necessary to obtain matching expressions for the horizontal component of velocity and the streamfunction (the vertical component of velocity is assumed to be zero for this background flow, as in the inviscid version).

These are obtained by integrating the background vorticity $\Omega_{01}(y)$ and the resulting expressions are

$$U_{01}(y) = -\frac{\gamma_1 - \gamma_2}{2}y - \frac{\gamma_1 - \gamma_2}{2S} \log(\cosh Sy) + F_0 \quad (4.2.8)$$

$$\Psi_{01}(y) = -\frac{\gamma_1}{2}y^2 + \left(F_0 + \frac{\gamma_1 - \gamma_2}{2S} \log 2\right)y - \frac{\gamma_1 - \gamma_2}{4S} \text{Li}_2(-e^{-2Sy}) \quad (4.2.9)$$

with

$$c = \frac{\gamma_1}{2} + (F_0 + \frac{\gamma_1 - \gamma_2}{2} \log 2) + \frac{\omega_1 - \omega_2}{4S} \text{Li}_2(-e^{2S}),$$

and here $\text{Li}_2(y)$ is the dilogarithm function (see Abramowitz and Stegun [1, section 27.7]). The constants of integration in (4.2.8) and (4.2.9) have been chosen such that the horizontal velocity profile $U_{01}(y)$ is equal to F_0 for $y = 0$ and the stream-function $\Psi_{01}(y)$ is equal to zero at the bottom wall $y = -1$. These profiles closely match those used in the inviscid version of the problem and as an example the horizontal velocity component profiles for the piecewise profile from section 4.2.1 are compared with that in equation (4.2.8), as illustrated in figure 4.1. As the steepness parameter S is increased the two profiles become nearly indistinguishable, although typically moderate values for S will be selected so that the resolution required in later computational schemes is not too fine.

4.3. Linearized solution to the inviscid problem

The inviscid problem of section 4.2.1 is approximated with a linearized system. This system is subjected to a small perturbation and the resulting behaviour studied. The goal here is to establish whether the system behaves differently for various choices of parameters values. There is a possibility that the interface may grow unstably when given a small perturbation, for instance. Such an analysis is common in dealing with inviscid flows of this type, a classic example being the derivation of the stability criterion for Kelvin-Helmholtz instability as presented, for example, by Lamb [35, article 232].

The solution is assumed to be a small perturbation about the background flow, as was set out in section 4.2.1, in which the interface is assumed to be horizontal and the layers flow with constant but possibly different amounts of shear, and the horizontal velocity profile is specified so that it is continuous across the interface. Apart from perturbing the interface height function $\eta(x, t)$ it is also necessary to perturb the velocity potentials Φ_1 and Φ_2 as well as the two streamfunctions Ψ_1 and Ψ_2 ; to this end the small amplitude linearization parameter ε is introduced. When perturbations of order ε are applied to the background flow the resulting expressions are

$$\eta(x, t) = \varepsilon H(x, t) + \mathcal{O}(\varepsilon^2) \quad (4.3.1)$$

$$\Phi_i(x, y, t) = \varepsilon \Phi_{i1}(x, y, t) + \mathcal{O}(\varepsilon^2) \quad (4.3.2)$$

$$\Psi_i(x, y, t) = \varepsilon \Psi_{i1}(x, y, t) + \mathcal{O}(\varepsilon^2) \quad (4.3.3)$$

for $i = 1, 2$, in which terms of order ε^2 and higher are neglected. Effectively ε is a small parameter proportional to the height of the perturbed interfacial wave. The expressions (4.3.1)–(4.3.3) may be substituted into the kinematic boundary conditions (4.2.1) and after retaining only first-order terms these conditions become

$$\frac{\partial H}{\partial t} = \frac{\partial \Phi_{i1}}{\partial y} - F_0 \frac{\partial H}{\partial x} \quad \text{on } y = 0, i = 1, 2 \quad (4.3.4)$$

for each side of the interface. Here the perturbed forms of the velocity potentials have been used in evaluating the respective velocity components. By substituting the perturbed expressions (4.3.1)–(4.3.3) into the dynamic boundary condition (4.2.2) a linearized version of that condition may be obtained, namely

$$\begin{aligned} \frac{\partial \Phi_{21}}{\partial t} - D \frac{\partial \Phi_{11}}{\partial t} &= -F_0 \left(\frac{\partial \Phi_{21}}{\partial x} - D \frac{\partial \Phi_{11}}{\partial x} \right) \\ &\quad - \gamma_2 \Psi_{21} + D \gamma_1 \Psi_{11} - (1 - D)H \quad \text{on } y = 0 \end{aligned} \quad (4.3.5)$$

and again terms of order ε^2 and higher have been discarded. The perturbations are now assumed to take some general forms and by substituting these into the

linearized boundary conditions it is possible to examine the behaviour of the interface. The perturbed part of the interfacial height is assumed to be a travelling wave with period $2\pi/k$ and a frequency of ω ; that is

$$H(x, t) = g_1 e^{i(\omega t - kx)} \quad (4.3.6)$$

where an arbitrary initial amplitude g_1 has been introduced. In a similar fashion the perturbed parts of the linearized velocity potentials are

$$\Phi_{11}(x, y, t) = a_1 \cosh(k(y - h)) e^{i(\omega t - kx)} \quad (4.3.7)$$

$$\Phi_{21}(x, y, t) = a_2 \cosh(k(y + 1)) e^{i(\omega t - kx)} \quad (4.3.8)$$

where the hyperbolic cosines are used so that the vertical components of velocity, v_1 and v_2 , are zero at the top and bottom walls, respectively. The corresponding streamfunctions may be obtained via the Cauchy-Riemann equations and it is straightforward to show that the appropriate forms for these are

$$\Psi_{11}(x, y, t) = -ia_1 \sinh(k(y - h)) e^{i(\omega t - kx)} \quad (4.3.9)$$

$$\Psi_{21}(x, y, t) = -ia_2 \sinh(k(y + 1)) e^{i(\omega t - kx)}. \quad (4.3.10)$$

Here a_1 and a_2 are the same constants as were used in (4.3.7) and (4.3.8). In terms of how the system behaves through time, the important parameter here is the frequency ω . When this parameter has a non-zero imaginary part a small perturbation to the interface will grow exponentially. The travelling wave solutions (4.3.6)–(4.3.10) may be substituted into the linearized boundary conditions and after a little algebra the arbitrary constants may be eliminated. This gives a quadratic for ω and the resulting dispersion relation is

$$\omega = \frac{2F_0 k \delta + \gamma_2 - D\gamma_1}{2\delta} \pm \frac{1}{2\delta} \sqrt{(\gamma_2 - D\gamma_1)^2 + 4\delta(1 - D)} \quad (4.3.11)$$

with $\delta = \coth k + D \coth kh$. The part of this expression under the square root can never be less than zero (since $D < 1$) and so the system will never become unstable

in the sense that a small perturbation will grow exponentially. This is not to say that (4.3.11) indicates that the linearized problem has no interesting time dependent behaviour. The result of the superposition of the two resulting frequencies above is a classic standing wave, which for certain choices of parameters will travel as it oscillates. Pure travelling waves are also available when one of the frequencies in (4.3.11) is zero.

4.4. First-order perturbation series approach to the viscous problem

The linearized inviscid analysis of section 4.3 shows that a small interfacial perturbation to the two-layer shear flow will not grow unstably. This implies that most of the interesting subsequent evolution of the system occurs in a small neighbourhood of this interfacial region. There are a few options for modelling such a situation in viscous flow. One approach might be to use a finite difference or finite element scheme over the flow region, as was used to model the Kelvin-Helmholtz instability in chapter 3. For this to be done efficiently and with sufficient resolution to resolve a small perturbation either a fine grid size would need to be chosen or an uneven grid focused on the interfacial region would need to be implemented. The latter may not account for effects at the walls, such as boundary layers, whilst the former is potentially computationally expensive. A fully non-linear spectral solution, such as the type used by Forbes [24] to model the Rayleigh-Taylor instability, is similarly computationally expensive.

In Forbes [24] the Rayleigh-Taylor instability was modelled to a very high degree of accuracy with a vorticity-streamfunction approach. Double Fourier series were used to give a very general form of the solutions for density and vorticity. A particular advantage of this approach is that the series may be specified in such a way that the definition of vorticity (4.2.3) is satisfied identically. For an unstable flow such as the Rayleigh-Taylor instability, where an initial flow condition develops in highly complex non-linear ways to produce solutions at later times which are very different from the initial condition, the generality of this approach is justified;

indeed it is necessary to capture the growth of the initial perturbation. The computational cost in such a method is that a large number of double integrals need to be calculated at each time step, with the number of integrals increasing as more Fourier coefficients are used in the double series for accuracy.

The major simplification of the approach used to model the 2-layer shear flow here, compared with a full spectral method, is to assume that the Fourier series contains only the first and zeroth modes in x ; that is, it is monochromatic. This places several restrictions on the type of solution that will be allowed, namely that the wave cannot grow too large and that any evolution in the x -direction will be restricted to that allowed by the reduced series. As the predictions of inviscid linear theory were that a small perturbation will not grow exponentially and will result in a standing wave that possibly travels in x these restrictions are acceptable for this flow. In addition to this, an analysis based on perturbation series techniques is performed on the governing equations (4.2.3)–(4.2.5) under the assumption that the evolving flow is a small perturbation to the flow profile specified in section 4.2.2.

As a first step it is assumed that the solutions for density and vorticity are given in terms of a background flow, namely $R_0(y, t)$ for density and $\Omega_0(y, t)$ for vorticity, plus a small perturbation. These are written as

$$\zeta(x, y, t) = \Omega_0(y, t) + \varepsilon \Omega_1(x, y, t) + \mathcal{O}(\varepsilon^2) \quad (4.4.1)$$

$$\rho(x, y, t) = R_0(y, t) + \varepsilon R_1(x, y, t) + \mathcal{O}(\varepsilon^2) \quad (4.4.2)$$

where ε has been introduced as a small parameter in the order of the initial perturbation and in this analysis terms of order ε^2 and higher will eventually be discarded. The initial conditions for the background density $R_0(y, t)$ and vorticity $\Omega_0(y, t)$ are the hyperbolic tangent profiles specified in section 4.2.2, $R_{01}(y)$ and $\Omega_{01}(y)$, and time dependence is included in $R_0(y, t)$ and $\Omega_0(y, t)$ to account for the gradual diffusion of these initially sharp profiles. At a later stage a corresponding streamfunction will be obtained by simple integration so that it identically satisfies the definition of vorticity (4.2.3) and then this may be differentiated to obtain expressions for the

velocity components. For the purposes of this analysis of the governing equations, however, it is necessary to introduce the perturbed forms of these, namely

$$\psi(x, y, t) = \Psi_0(y, t) + \varepsilon \Psi_1(x, y, t) + \mathcal{O}(\varepsilon^2) \quad (4.4.3)$$

$$u(x, y, t) = U_0(y, t) + \varepsilon U_1(x, y, t) + \mathcal{O}(\varepsilon^2) \quad (4.4.4)$$

$$v(x, y, t) = 0 + \varepsilon V_1(x, y, t) + \mathcal{O}(\varepsilon^2) \quad (4.4.5)$$

where the velocity components are related to the streamfunction by $u = \partial\psi/\partial y$ and $v = -\partial\psi/\partial x$. The above forms of the solutions (4.4.1)–(4.4.5) are effectively the first two terms of a perturbation series and the following procedure makes use of these to obtain a first-order perturbation approximation to the governing equations (4.2.3)–(4.2.5). Such techniques are outlined by Bender and Orszag [7, chapter 7], for instance.

The perturbed expressions (4.4.1)–(4.4.5) are substituted into the governing equations (4.2.3)–(4.2.5). An unperturbed (zeroth-order) version of this system is then obtained by setting $\varepsilon = 0$ and the resulting form of the governing equations is

$$\frac{\partial^2 \Psi_0}{\partial y^2} = -\Omega_0 \quad (4.4.6)$$

$$\frac{\partial \Omega_0}{\partial t} = \nu \frac{\partial^2 \Omega_0}{\partial y^2} \quad (4.4.7)$$

$$\frac{\partial R_0}{\partial t} = \sigma \frac{\partial^2 R_0}{\partial y^2}. \quad (4.4.8)$$

Here the unperturbed definition of vorticity (4.4.6) relates the zeroth-order parts of vorticity and streamfunction, whilst these forms of the vorticity equation (4.4.7) and the density equation (4.4.8) account for the diffusion of the initial background profile. A first order approximation of the governing equations may now be obtained by substituting the perturbed forms (4.4.1)–(4.4.5) into the governing equations and, first neglecting terms of $\mathcal{O}(\varepsilon^2)$ and higher, since the $\mathcal{O}(1)$ terms constitute the unperturbed system above, then by method of variation of parameters the terms of order ε then constitute a system of differential equations that may be solved

separately. The resulting first-order approximations of equations (4.2.3)–(4.2.5) are

$$\frac{\partial^2 \Psi_1}{\partial x^2} + \frac{\partial^2 \Psi_1}{\partial y^2} = -\Omega_1 \quad (4.4.9)$$

$$\frac{\partial \Omega_1}{\partial t} + U_0 \frac{\partial \Omega_1}{\partial x} + V_1 \frac{\partial \Omega_0}{\partial y} = \nu \nabla^2 \Omega_1 - \frac{\partial R_1}{\partial x} \quad (4.4.10)$$

$$\frac{\partial R_1}{\partial t} + U_0 \frac{\partial R_1}{\partial x} + V_1 \frac{\partial R_0}{\partial y} = \sigma \nabla^2 R_1. \quad (4.4.11)$$

This version of the governing equations, combined with the unperturbed equations (4.4.6)–(4.4.8), represents an approximation to the original equations that should be sufficient to capture the expected standing wave behaviour of the two layer shear flow. In solving this system it is possible to solve the unperturbed equations first, since they do not depend on the first order terms, and then use those solutions in treating the first order equations (4.4.9)–(4.4.11). In effect, the original system of three non-linear differential equations has been replaced with two sets of three linear differential equations.

The zeroth-order parts of vorticity Ω_0 and density R_0 are chosen to be the base flow plus a time dependent Fourier series in y . Here the series are specified so that they satisfy the boundary conditions at the top and bottom wall that both the vorticity ζ and the density ρ are constant at the top and bottom walls; namely that for vorticity $\zeta = \gamma_1$ at $y = h$ and $\zeta = \gamma_2$ at $y = -1$, while for density $\rho = D$ at $y = h$ and $\rho = 1$ at $y = -1$. Since these are the values for the base vorticity $\Omega_{01}(y)$ and density $R_{01}(y)$ at the walls, the series part of the zeroth-order expressions is zero at $y = h$ and $y = -1$. It follows that the appropriate form of these zeroth-order

parts is

$$\Omega_0(y, t) = \Omega_{01}(y) + \sum_{n=1}^N A_{0n}(t) \sin(\beta_n(y+1)) \quad (4.4.12)$$

$$R_0(y, t) = R_{01}(y) + \sum_{n=1}^N C_{0n}(t) \sin(\beta_n(y+1)) \quad (4.4.13)$$

where $\beta_n = n\pi/(h+1)$ and the Fourier series coefficients $A_{0n}(t)$ and $C_{0n}(t)$, for $n = 1, \dots, N$, have been introduced with the series becoming more accurate as N tends to infinity. The corresponding series for streamfunction, obtained by integrating the expression for Ω_0 (4.4.12) twice in y so that the zeroth-order definition of vorticity (4.4.6) is satisfied, is

$$\Psi_0(y, t) = \Psi_{01}(y) + \sum_{n=1}^N \frac{1}{\beta_n^2} A_{0n}(t) \sin(\beta_n(y+1)) \quad (4.4.14)$$

and here $\Psi_{01}(y)$ is the background streamfunction as defined in section 4.2.2. This may then be differentiated to obtain the zeroth-order part of horizontal velocity, the series form of which is

$$U_0(y, t) = U_{01}(y) + \sum_{n=1}^N \frac{1}{\beta_n} A_{0n}(t) \cos(\beta_n(y+1)) \quad (4.4.15)$$

and this will be used in the first-order governing equations (4.4.10) and (4.4.11), once the coefficients $A_{0n}(t)$, for $n = 1, \dots, N$, have been evaluated.

The series form of the zeroth-order part of vorticity (4.4.12) is now substituted into the zeroth-order approximation to the vorticity equation (4.4.7), and similarly the zeroth-order part of density (4.4.13) is substituted into the zeroth-order density equation (4.4.8). These are then multiplied by the Fourier basis function $\sin(\beta_j(y+1))$, for $j = 1, \dots, N$, and integrated in the y direction from $y = -1$ to $y = h$. The resulting sets of differential equations for the series coefficients A_{0j} and

C_{0j} , for $j = 1, \dots, N$, are

$$A'_{0j} = \frac{2\nu}{h+1} \mathcal{J}_j - \nu \beta_j^2 A_{0j} \quad (4.4.16)$$

$$C'_{0j} = \frac{2\sigma}{h+1} \mathcal{K}_j - \sigma \beta_j^2 C_{0j} \quad (4.4.17)$$

where in these equations the integrals

$$\mathcal{J}_j = \int_{-1}^h \frac{d^2 \Omega_{01}}{dy^2} \sin(\beta_j (y+1)) dy \quad (4.4.18)$$

$$\mathcal{K}_j = \int_{-1}^h \frac{d^2 R_{01}}{dy^2} \sin(\beta_j (y+1)) dy \quad (4.4.19)$$

for $j = 1, \dots, N$, have been introduced for convenience of notation. Since equations (4.4.16) and (4.4.17) are inhomogeneous exponential decay equations they have closed form solutions and these are

$$A_{0j} = \frac{2\mathcal{J}_j}{\beta_j^2(h+1)} \left(1 - e^{-\nu \beta_j^2 t}\right) \quad (4.4.20)$$

$$C_{0j} = \frac{2\mathcal{K}_j}{\beta_j^2(h+1)} \left(1 - e^{-\sigma \beta_j^2 t}\right) \quad (4.4.21)$$

for $j = 1, \dots, N$. Here it has been assumed that the zeroth-order part of vorticity and density are initially the undiffused base profiles specified as $\Omega_{01}(y)$ and $R_{01}(y)$, and as such the Fourier series coefficients in equations (4.4.20) and (4.4.21) have been chosen so that they are initially zero.

The first-order parts of (4.4.1)–(4.4.5) are assumed to be Fourier series in x and y . They only contain, as previously discussed, the zeroth and first modes in x which greatly reduces the number of time dependent coefficients that need to be solved for, while remaining sufficiently general that the expected small amplitude behaviour of the flow will be captured. The series forms of the first-order parts of

vorticity Ω_1 and density R_1 are

$$\Omega_1(x, y, t) = \sum_{n=1}^N [A_{10n}(t) + A_{1n}(t) \cos kx + B_{1n}(t) \sin kx] \sin(\beta_n(y+1)) \quad (4.4.22)$$

$$R_1(x, y, t) = \sum_{n=1}^N [C_{10n}(t) + C_{1n}(t) \cos kx + D_{1n}(t) \sin kx] \sin(\beta_n(y+1)) \quad (4.4.23)$$

where the $6N$ Fourier series coefficients $A_{10n}(t)$, $A_{1n}(t)$, $B_{1n}(t)$, $C_{10n}(t)$, $C_{1n}(t)$ and $D_{1n}(t)$, for $n = 1, \dots, N$, have been introduced and the above series become more accurate as N tends to infinity. As with the series part of the zeroth-order expression for vorticity (4.4.12) and density (4.4.13), the first-order series have been chosen so that they are zero on the walls at $y = h$ and $y = -1$. The series form of the first-order part of vorticity (4.4.22) is now used to obtain the corresponding expression for streamfunction so that the first-order approximation of the definition of vorticity (4.4.9) is satisfied. Having substituted the series (4.4.22) into the definition of vorticity (4.4.9) it follows, after some straightforward integration, that

$$\Psi_1(x, y, t) = \sum_{n=1}^N \left\{ \frac{1}{\beta_n^2} A_{10n}(t) + \frac{1}{\alpha_n^2} [A_{1n}(t) \cos kx + B_{1n}(t) \sin kx] \right\} \sin(\beta_n(y+1)) \quad (4.4.24)$$

with $\alpha_n^2 = k^2 + \beta_n^2$ and this may then be differentiated to obtain the first-order series of the velocity components; the expressions for the horizontal component of velocity U_1 and the vertical component V_1 are

$$U_1(x, y, t) = \sum_{n=1}^N \left\{ \frac{1}{\beta_n} A_{10n}(t) + \frac{\beta_n}{\alpha_n^2} [A_{1n}(t) \cos kx + B_{1n}(t) \sin kx] \right\} \cos(\beta_n(y+1)) \quad (4.4.25)$$

$$V_1(x, y, t) = \sum_{n=1}^N \frac{k}{\alpha_n^2} [A_{1n}(t) \sin kx - B_{1n}(t) \cos kx] \sin(\beta_n(y+1)). \quad (4.4.26)$$

Note that here only the first-order series for the vertical velocity component V_1 will be used in evaluating the first-order versions of the vorticity equation (4.4.10) and the density equation (4.4.11); the expression for U_1 is included for completeness.

The first-order series (4.4.22)–(4.4.26) as well as the zeroth-order series (4.4.12)–(4.4.15) are now substituted into the first-order perturbation approximations of the vorticity equation (4.4.10) and the density equation (4.4.11) and will be analyzed to obtain differential equations for the Fourier series coefficients. The vorticity equation will be considered first. Once the appropriate series have been substituted into equation (4.4.10) the resulting expression is multiplied by the Fourier basis functions $\sin(\beta_j(y+1))$, for $j = 1, \dots, N$, and then integrated in the x direction from $x = 0$ to $x = 2\pi/k$, that is over one period, and in the y direction from $y = -1$ to $y = h$. This yields a system of differential equations for the coefficients associated with the zeroth mode in x , namely

$$A'_{10j} = -\nu\beta_j^2 A_{10j} \quad (4.4.27)$$

for $j = 1, \dots, N$. Equation (4.4.27) is an exponential decay equation, with solution

$$A_{10j}(t) = A_{10j}(0) e^{-\nu\beta_j^2 t}. \quad (4.4.28)$$

Here the solution has been specified in terms of the initial value of the coefficient $A_{10j}(0)$ and the choice of initial conditions for this and the remaining Fourier series coefficients will be discussed in detail in section 4.4.1. A similar procedure is applied to derive differential equations featuring the coefficients associated with the first mode in x . The vorticity equation (4.4.10), having had the various series substituted into it, is multiplied by each Fourier basis function $\cos kx \sin(\beta_j(y+1))$, for $j = 1, \dots, N$, and integrated from $x = 0$ to $x = 2\pi$ in the x direction and from $y = -1$

to $y = h$ in the y direction. After some rearrangement this gives

$$\begin{aligned} A'_{1j} = & -\frac{2k}{h+1} \sum_{n=1}^N \left(\mathcal{U}_{nj} - \frac{\mathcal{Z}_{nj}}{\alpha_n^2} \right) B_{1n} \\ & -\frac{2k}{h+1} \sum_{m=1}^N \sum_{n=1}^N \left(\frac{1}{\beta_m} - \frac{\beta_m}{\alpha_n^2} \right) A_{0m} B_{1n} \mathcal{W}_{mn}^j - \nu \alpha_j^2 A_{1j} - k D_{1j} \end{aligned} \quad (4.4.29)$$

for $j = 1, \dots, N$. Similarly, the vorticity equation is now multiplied by $\sin kx \sin(\beta_j(y+1))$ and integrated to obtain

$$\begin{aligned} B'_{1j} = & \frac{2k}{h+1} \sum_{n=1}^N \left(\mathcal{U}_{nj} - \frac{\mathcal{Z}_{nj}}{\alpha_n^2} \right) A_{1n} \\ & + \frac{2k}{h+1} \sum_{m=1}^N \sum_{n=1}^N \left(\frac{1}{\beta_m} - \frac{\beta_m}{\alpha_n^2} \right) A_{0m} A_{1n} \mathcal{W}_{mn}^j - \nu \alpha_j^2 B_{1j} + k C_{1j}. \end{aligned} \quad (4.4.30)$$

for $j = 1, \dots, N$. Several integrals have been introduced in equations (4.4.29) and (4.4.30), and these have been defined as

$$\mathcal{U}_{nj} = \int_{-1}^h U_{01} \sin(\beta_n(y+1)) \sin(\beta_j(y+1)) dy \quad (4.4.31)$$

$$\mathcal{Z}_{nj} = \int_{-1}^h \frac{d\Omega_{01}}{dy} \sin(\beta_n(y+1)) \sin(\beta_j(y+1)) dy \quad (4.4.32)$$

$$\mathcal{W}_{mn}^j = \int_{-1}^h \cos(\beta_m(y+1)) \sin(\beta_n(y+1)) \sin(\beta_j(y+1)) dy. \quad (4.4.33)$$

It has been found convenient here to use the fact that

$$\mathcal{W}_{mn}^j = \begin{cases} (h+1)/4 & \text{if } j = -m + n \text{ or } j = m + n \\ -(h+1)/4 & \text{if } j = m - n \\ 0 & \text{otherwise} \end{cases}$$

in order to avoid extraneous computational effort in evaluating the double sum terms. Note that equations (4.4.29) and (4.4.30) are both linear differential equations since the coefficient from the zeroth-order series (the A_{0m} in the double series term) may be evaluated directly from equation (4.4.20).

A similar set of differential equations may be derived from analyzing (4.4.11), the first-order approximation to the density equation. Substituting the requisite zeroth and first-order series into (4.4.11), then multiplying by the Fourier basis function $\sin(\beta_j(y+1))$, for $j = 1, \dots, N$, and integrating gives

$$C'_{10j} = -\sigma\beta_j^2 C_{10j} \quad (4.4.34)$$

and, similar to the previous exponentially decay equation (4.4.27), the appropriate closed form solution is

$$C_{10j}(t) = C_{10j}(0) e^{-\sigma\beta_j^2 t} \quad (4.4.35)$$

for $j = 1, \dots, N$. The first-order density equation is now multiplied by $\cos kx \sin(\beta_j(y+1))$ and integrated to give

$$\begin{aligned} C'_{1j} = & -\frac{2k}{h+1} \sum_{n=1}^N D_{1n} \mathcal{U}_{nj} - \frac{2k}{h+1} \sum_{m=1}^N \sum_{n=1}^N \frac{1}{\beta_m} A_{0m} D_{1n} \mathcal{W}_{mn}^j \\ & + \frac{2k}{h+1} \sum_{n=1}^N \frac{1}{\alpha_n^2} B_{1n} \mathcal{R}_{nj} + \frac{2k}{h+1} \sum_{m=1}^N \sum_{n=1}^N \frac{\beta_m}{\alpha_n^2} C_{0m} B_{1n} \mathcal{W}_{mn}^j - \sigma\alpha_j^2 C_{1j} \end{aligned} \quad (4.4.36)$$

for $j = 1, \dots, N$, and finally the density equation is multiplied by $\sin kx \sin(\beta_j(y+1))$ and integrated to yield the differential equation

$$\begin{aligned} D'_{1j} = & \frac{2k}{h+1} \sum_{n=1}^N C_{1n} \mathcal{U}_{nj} + \frac{2k}{h+1} \sum_{m=1}^N \sum_{n=1}^N \frac{1}{\beta_m} A_{0m} C_{1n} \mathcal{W}_{mn}^j \\ & - \frac{2k}{h+1} \sum_{n=1}^N \frac{1}{\alpha_n^2} A_{1n} \mathcal{R}_{nj} - \frac{2k}{h+1} \sum_{m=1}^N \sum_{n=1}^N \frac{\beta_m}{\alpha_n^2} C_{0m} A_{1n} \mathcal{W}_{mn}^j - \sigma\alpha_j^2 D_{1j} \end{aligned} \quad (4.4.37)$$

for $j = 1, \dots, N$. In addition to making use of the integrals previously defined in (4.4.31)–(4.4.33), in equations (4.4.36) and (4.4.37) the integral

$$\mathcal{R}_{nj} = \int_{-1}^h \frac{dR_{01}}{dy} \sin(\beta_n(y+1)) \sin(\beta_j(y+1)) dy \quad (4.4.38)$$

has been introduced. The coefficients in these equations from the zeroth order series A_{0m} and C_{0m} may be evaluated from (4.4.20) and (4.4.21), respectively. Equations

(4.4.29), (4.4.30), (4.4.36) and (4.4.37) thus constitute a set of $4N$ linear differential equations for the unknown coefficients from the first-order series.

It is worth noting that since the integrals (4.4.31)–(4.4.33) and (4.4.38) are not time dependent, they need only be calculated once for a particular choice of background flow. Taking this a step further it is possible to rewrite the integrals (4.4.31), (4.4.32) and (4.4.38) in terms of the flow parameters by explicitly using the choice of background flow made in section (4.2.2). By making the substitutions for U_1 , $d\Omega_1/dy$ and dR_1/dy , as defined in (4.2.8), (4.2.7) and (4.2.6) respectively, these integrals become

$$\mathcal{U}_{nj} = -\frac{\gamma_1 + \gamma_2}{2}\mathcal{M}_{nj} - \frac{\gamma_1 - \gamma_2}{2}\mathcal{N}_{nj} + F_0\mathcal{L}_{nj} \quad (4.4.39)$$

$$\mathcal{Z}_{nj} = \frac{(\gamma_1 - \gamma_2)S}{2}\mathcal{P}_{nj} \quad (4.4.40)$$

$$\mathcal{R}_{nj} = \frac{(D-1)S}{2}\mathcal{P}_{nj} \quad (4.4.41)$$

where the additional integrals \mathcal{L}_{nj} , \mathcal{M}_{nj} , \mathcal{N}_{nj} and \mathcal{P}_{nj} have been defined as

$$\mathcal{L}_{nj} = \int_{-1}^h \sin(\beta_n(y+1)) \sin(\beta_j(y+1)) dy \quad (4.4.42)$$

$$\mathcal{M}_{nj} = \int_{-1}^h y \sin(\beta_n(y+1)) \sin(\beta_j(y+1)) dy \quad (4.4.43)$$

$$\mathcal{N}_{nj} = \int_{-1}^h \log(\cosh Sy) \sin(\beta_n(y+1)) \sin(\beta_j(y+1)) dy \quad (4.4.44)$$

$$\mathcal{P}_{nj} = \int_{-1}^h \operatorname{sech}^2 Sy \sin(\beta_n(y+1)) \sin(\beta_j(y+1)) dy \quad (4.4.45)$$

for $j, n = 1, \dots, N$. The advantage to using the integrals in the form (4.4.39)–(4.4.41) rather than that of (4.4.31), (4.4.32) and (4.4.38) is that the calculation of the intermediate integrals (4.4.42)–(4.4.45) need be only done once for a choice of steepness parameter S and the number of coefficients in each Fourier series N . This means that the integrals (4.4.39)–(4.4.41) may be computed for a whole suite of values of the other flow parameters (namely γ_1 , γ_2 , F_0 and D) at a comparatively light computational cost. In the results section 4.5.1, for instance, the values of the

background shear are varied while the other parameters, including S and N , are held constant. There are typically a large number of coefficients used in each series and as such accurate evaluation of the series is made practical by only calculating the integrals once; that is, repeatedly computing the four sets of N^2 integrals would be prohibitive.

The system of $4N$ ordinary differential equations (4.4.29), (4.4.30), (4.4.36) and (4.4.37) is solved using an adaptive Runge-Kutta method of orders 4 and 5, namely the ODE45 routine in MATLAB. This is both accurate and will select appropriate sized time-steps so that the error will be controlled adaptively. Up to 401 coefficients will be used in evaluating the Fourier series. With such a large choice of N it is necessary to use quite a fine grid when calculating the integrals (4.4.42)–(4.4.45). A highly accurate Gaussian quadrature scheme is used to evaluate all integrals, with the nodal points computed using a routine made available by von Winckel [63]. For this unevenly spaced grid it is necessary to use up to 4001 integration points to evaluate accurately the large number of integrals required here.

4.4.1. Choice of initial conditions. A careful choice of the initial values of the Fourier series coefficients is required so that the method outlined above will mimic the inviscid version of the two-layer shear problem. Recall that in the inviscid version the density interface is given a small sinusoidal perturbation. This is achieved for the viscous flow by perturbing the background density profile (4.2.6) so that the point of inflection in the hyperbolic tangent is about the small amplitude sinusoid $y = \varepsilon \sin kx$ rather than $y = 0$. The perturbed form of density is

$$\rho_{pert}(x, y) = \frac{D+1}{2} + \frac{D-1}{2} \tanh(S(y - \varepsilon \sin kx)) \quad (4.4.46)$$

and the background vorticity (4.2.7) may be perturbed in a similar way to give

$$\zeta_{pert}(x, y) = \frac{\gamma_1 + \gamma_2}{2} + \frac{\gamma_1 - \gamma_2}{2} \tanh(S(y - \varepsilon \sin kx)). \quad (4.4.47)$$

The initial values for the first-order Fourier series coefficients $A_{10n}(0)$, $A_{1n}(0)$, $B_{1n}(0)$, $C_{10n}(0)$, $C_{1n}(0)$ and $D_{1n}(0)$, for $n = 1, \dots, N$, are then chosen so that

the perturbed series solutions (4.4.1) and (4.4.2) match the perturbations to the base flow (4.4.46) and (4.4.47) at $t = 0$. To obtain these values the two expressions for density (4.4.2) and (4.4.46) are equated and it follows by simple rearrangement that $R_1(x, y, 0)$ the initial first-order part of density is

$$R_1(x, y, 0) = \frac{D-1}{2\varepsilon} \{ \tanh(S(y - \varepsilon \sin kx)) - \tanh Sy \} \quad (4.4.48)$$

and similarly, by equating the expressions of vorticity (4.4.1) and (4.4.47), the perturbed part of vorticity $\Omega_1(x, y, 0)$ is found to be

$$\Omega_1(x, y, 0) = \frac{\gamma_1 - \gamma_2}{2\varepsilon} \{ \tanh(S(y - \varepsilon \sin kx)) - \tanh Sy \}. \quad (4.4.49)$$

It is now possible to equate these choices for $R_1(x, y, 0)$ and $\Omega_1(x, y, 0)$ to their Fourier series equivalents (4.4.23) and (4.4.22) so that for the density we have

$$\begin{aligned} & \sum_{n=1}^N [C_{10n}(0) + C_{1n}(0) \cos kx + D_{1n}(0) \sin kx] \sin(\beta_n(y+1)) \\ &= \frac{D-1}{2\varepsilon} \{ \tanh(S(y - \varepsilon \sin kx)) - \tanh Sy \} \end{aligned} \quad (4.4.50)$$

and the equivalent expression for the initial perturbation to the background vorticity is

$$\begin{aligned} & \sum_{n=1}^N [A_{10n}(0) + A_{1n}(0) \cos kx + B_{1n}(0) \sin kx] \sin(\beta_n(y+1)) \\ &= \frac{\gamma_1 - \gamma_2}{2\varepsilon} \{ \tanh(S(y - \varepsilon \sin kx)) - \tanh Sy \}. \end{aligned} \quad (4.4.51)$$

The expressions (4.4.50) and (4.4.51) are then integrated to obtain the appropriate initial values for the Fourier series coefficients. Both sides of each of (4.4.50) and (4.4.51) are multiplied by the Fourier basis function $\sin(\beta_j(y+1))$, with $j = 1, \dots, N$, and integrated in the x -direction from $x = 0$ to $x = 2\pi/k$ and then integrated again in the y -direction from $y = -1$ to $y = h$. The results of these

integrations are then rearranged to obtain

$$A_{10j}(0) = \frac{(\gamma_1 - \gamma_2)k}{2\pi\varepsilon(h+1)} \mathcal{A}_{0j} \quad (4.4.52)$$

$$C_{10j}(0) = \frac{(D-1)k}{2\pi\varepsilon(h+1)} \mathcal{A}_{0j} \quad (4.4.53)$$

for $j = 1, \dots, N$. Further expressions for the initial values of the other coefficients may be obtained in a similar way. To obtain expressions for the even coefficients $A_{1j}(0)$ and $C_{1j}(0)$, (4.4.50) and (4.4.51) are multiplied by $\cos kx \sin(\beta_j(y+1))$, with $j = 1, \dots, N$, before being integrated and the resulting initial values are

$$A_{1j}(0) = \frac{(\gamma_1 - \gamma_2)k}{\pi\varepsilon(h+1)} \mathcal{A}_j \quad (4.4.54)$$

$$C_{1j}(0) = \frac{(D-1)k}{\pi\varepsilon(h+1)} \mathcal{A}_j \quad (4.4.55)$$

for $j = 1, \dots, N$. Finally (4.4.50) and (4.4.51) are multiplied by $\sin kx \sin(\beta_j(y+1))$ and then integrated to give

$$B_{1j}(0) = \frac{(\gamma_1 - \gamma_2)k}{\pi\varepsilon(h+1)} \mathcal{B}_j \quad (4.4.56)$$

$$D_{1j}(0) = \frac{(D-1)k}{\pi\varepsilon(h+1)} \mathcal{B}_j \quad (4.4.57)$$

for $j = 1, \dots, N$, and in (4.4.52)–(4.4.57) the additional integrals \mathcal{A}_{0j} , \mathcal{A}_j and \mathcal{B}_j have been introduced and are defined as

$$\mathcal{A}_{0j} = \int_0^{2\pi/k} \int_{-1}^h \{\tanh(S(y - \varepsilon \sin kx)) - \tanh Sy\} \sin(\beta_j(y+1)) dy dx \quad (4.4.58)$$

$$\mathcal{A}_j = \int_0^{2\pi/k} \int_{-1}^h \{\tanh(S(y - \varepsilon \sin kx)) - \tanh Sy\} \cos kx \sin(\beta_j(y+1)) dy dx \quad (4.4.59)$$

$$\mathcal{B}_j = \int_0^{2\pi/k} \int_{-1}^h \{\tanh(S(y - \varepsilon \sin kx)) - \tanh Sy\} \sin kx \sin(\beta_j(y+1)) dy dx \quad (4.4.60)$$

for $j = 1, \dots, N$. As with the integrals in the previous section, the quantities \mathcal{A}_{0j} , \mathcal{A}_j and \mathcal{B}_j are computed with a highly accurate Gaussian quadrature scheme,

with the number of grid points used adjusted with the choice of N , the number of coefficients in each series. These double integrals similarly need only be calculated once for a choice of steepness S , initial perturbation amplitude ε and number of Fourier series coefficients N with initial conditions for various values of the shear parameters, γ_1 and γ_2 , and the density ratio D available at no extra computational cost from the expressions (4.4.52)–(4.4.57), once the double integrals (4.4.58) and (4.4.60) have been evaluated. It should be emphasised that obtaining the initial condition in this fashion relies on choosing a small value for the initial perturbation amplitude ε . As a consequence of the Fourier series being chosen as monochromatic in x the possible initial conditions are restricted to functions that may be represented in that form. Although the ideal perturbed initial conditions (4.4.46) and (4.4.47) cannot be exactly captured by the reduced series, the resulting initial values for the series coefficients (4.4.52)–(4.4.57) will be accurate enough as long as ε is small.

4.5. Results

The focus of this study is on the viscous first-order perturbation series method outlined in section 4.4. This technique makes use of Fourier series solutions that only contain the zeroth and first modes in x . As such the solution is not fully general and is therefore restricted to linearized systems in which wave amplitude remains small. Clearly such a linearization would not be appropriate in unstable flows where amplitude increases rapidly, since eventually non-linear terms would dominate. An example of such a situation is where the amplitude of an interfacial wave grows to be much larger than its initial value; that is, where the solution deviates substantially from the base flow. This scheme is not suitable to compute Kelvin-Helmholtz (as modelled in chapter 3) or Rayleigh-Taylor instabilities, for instance. However, the computational efficiency of the scheme combined with the indications from the linearized inviscid analysis that standing wave type solutions exist (where the maximum wave height of the time dependent solution does not

get larger than that of the initial condition) suggest that these techniques are well suited to handling this type of 2-layer shear flow.

There are a large number of parameters that define the base flow and the initial condition and it is not the intention of this study to examine exhaustively the effect of each of these. The approach is to assume that most are held constant, varying only a few key parameters to emphasise various solutions of interest. As such, throughout the following work the density ratio is set as constant at $D = 0.99$, as would be appropriate for a seawater-freshwater boundary, see for instance Phillips [45]. Similarly, the size of the initial interfacial perturbation is chosen to be $\varepsilon = 0.01$ and the steepness parameter used is $S = 20$. In an attempt to mimic the inviscid situation the inverse Reynolds' number ν and the inverse Prandtl number σ are both chosen as small; that is, the fluid is assumed to be nearly inviscid and the layers of different densities will not mix too rapidly. This is achieved by choosing $\nu = 10^{-5}$ and $\sigma = 10^{-5}$. The linearized inviscid analysis of section 4.3 indicated that the Froude number F_0 only affects the group velocity of the wave and, under the assumption that this will continue to be the case in the viscous version of the flow, it will be set to zero with a view to focussing on the standing wave behaviour, rather than a hybrid of standing and travelling wave behaviours. The parameters left to be varied are the two shear parameters, γ_1 and γ_2 .

Several cases of interest will be examined in detail. The first of these, discussed in section 4.5.1, is a layer of constant shear where $\gamma_1 = \gamma_2$. By examining how the evolution of the flow changes for different shear layer strengths it is possible to make further comparisons when, in subsequent cases, the shear layer strength in each layer is allowed to differ. In section 4.5.2 it is assumed that there is zero vorticity in the top layer, with $\gamma_1 = 0$, and weak shear in the lower layer, so that $\gamma_2 \neq 0$. One of the difficulties in using the series representation (4.4.22) is that choosing values for the shear layer strengths that differ by too large an amount will introduce erroneous peaks and troughs in the initial conditions. This effectively places a restriction on the sorts of cases that may be studied and the choices that

are used in section 4.5.2 take this restriction into account. This is something of a moot point as it is unlikely that a situation where two fluid layers are able to maintain a very large sharp difference in vorticity could physically arise.

Throughout this discussion of results several summary variables will be used. As a large number of cases will be run it is inconvenient to examine the raw vorticity and density profiles at each time step. To avoid doing this, two new variables are created to summarise the vorticity and density profiles at each time step. The main interest in the evolution of density lies in how the diffuse interface evolves. In order to follow this, in a way that is straightforward to interpret and consistent with the genuine interface of the inviscid scheme, we will consider the shape of the contour for $\rho = (D + 1)/2$. This is effectively the mean contour of density and for the choice of initial conditions described in section 4.4.1 would initially be a sinusoid centred at $y = 0$. The maximum and minimum values in y for the contour are recorded and the difference between them is taken to be a measure of wave amplitude, denoted throughout this results section as \mathcal{A}_ρ .

Similarly for vorticity, interest lies in how strong the vorticity field is at any given point in time. To account for the possibility that vorticity may either be strongly negative or strongly positive both the maximum and minimum values, ζ_{max} and ζ_{min} , are recorded at each computed time step. In addition to these summary variables it is instructive to look at contour plots of the variables in question to get information about the detailed structure of the solution. For instance looking only at the amplitude \mathcal{A}_ρ does not give any indication as to whether the wave is travelling, nor does looking at the maximum and minimum of vorticity indicate where these points occur. Typically the solution will evolve in a similar fashion for the groups of cases outlined below so contour plots will be used sparingly as an example of how a suite of solutions behaves.

4.5.1. Layer of constant shear ($\gamma_1 = \gamma_2$). Solutions from the viscous scheme for a layer of constant shear are now presented. Seven values for strength of the shear layer are considered, namely the values $\gamma_1 = \gamma_2 = 0, \dots, 0.6$ in increments of

0.1. Additionally the extreme case of $\gamma_1 = \gamma_2 = 20$ is examined to give an example that varies greatly from the inviscid predictions.

The first case to be considered in detail is that of $\gamma_1 = \gamma_2 = 0$. Whilst it might seem counterintuitive to expect standing waves in what is essentially a stationary fluid, the inviscid analysis predicts such behaviour will occur. This case should be a useful test of the extent of the comparison that is possible between the two schemes. The angular frequency of the wave in the inviscid case may be calculated from equation (4.3.11) and in this case $\omega = \pm 0.0619$, so that a complete cycle of the oscillation will take $t_{cycle} = 1/2\pi|\omega| = 101.6$. It is sufficient, therefore, to run this and all subsequent cases from $t = 0$ to at least $t = 500$. This will ensure that at a minimum four complete cycles of the oscillatory behaviour are computed for each choice of shear layer strength. It is expected from equation (4.3.11) that as the values of γ_1 and γ_2 are increased the period of oscillation will become shorter.

Some contours of density and vorticity for early times are shown in figure 4.2. At each of the selected times a single contour of density is shown, that of $\rho = 0.995$, with contours of vorticity for the central part of the computational domain. The corresponding plots of \mathcal{A}_ρ , ζ_{min} and ζ_{max} for this case are shown in figure 4.3, up to the time $t = 2000$. Initially the density contour is sinusoidal and the vorticity is uniform, and as such no vorticity contours are shown in figure 4.2(a). For the next earliest time $t = 15.8$, shown in figure 4.2(b), the density contour has decreased in amplitude whilst two spikes have been induced in the vorticity profile. These spikes approximately coincide with the zeros of the sinusoid, with the spikes at $(x, y) = (0, 0)$ and $(\pi, 0)$ taking negative and positive values of vorticity, respectively. As the amplitude of the interfacial wave in density decreases further, these spikes increase in amplitude so that by the time $t = 23.2$, shown in figure 4.2(c), the vorticity has reached a relative maximum and minimum when the wave has decreased to zero amplitude. Following this, at the times $t = 34.4$ and 40.5 as shown in figure 4.2(d) and 4.2(e), the amplitude of the wave begins to grow again, now with the position of the maximum and minimum switched, and the

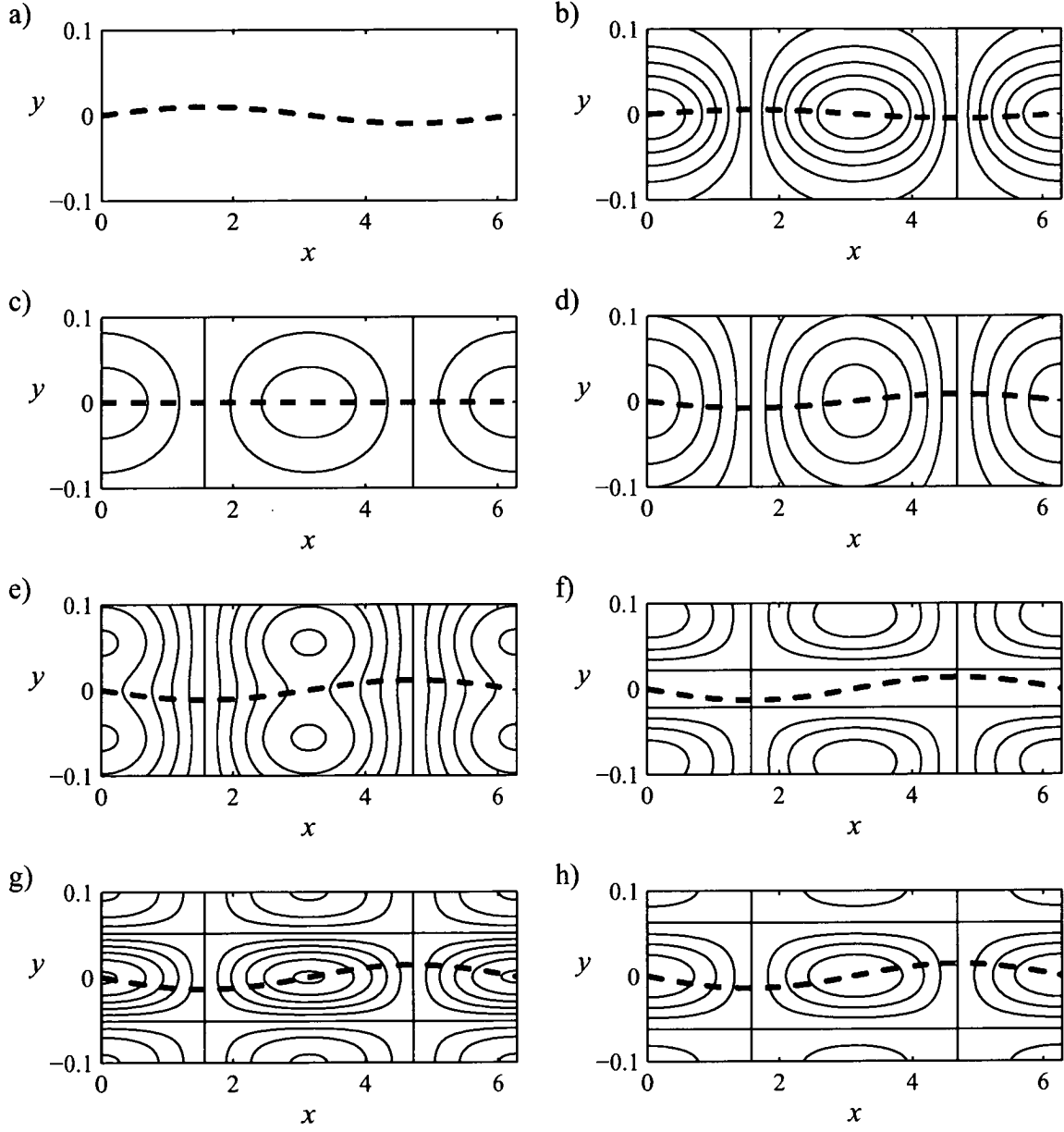


FIGURE 4.2. Contours of vorticity against a single contour of density (with the value $\rho = 0.995$ and shown as a dashed line) at the times $t = 0, 15.8, 23.2, 34.4, 40.5, 45.8, 49.9$ and 52.56 for the case of $\gamma_1 = \gamma_2 = 0$.

vorticity spikes around $y = 0$ begin to decrease in amplitude and start to become elongated in the y direction, eventually pinching in at the centre to form two pairs of vortices as in figure 4.2(f). Each of these vortices then starts to move away from the central region, and as they do a patch of vorticity of opposite polarity appears at the zeros of the wave. The outer vortices then diminish in amplitude so that by $t = 52.6$, shown in figure 4.2(h), the two new patches of positive and negative vorticity (note that these are at the opposite position to the spikes at the earlier times) have become the dominant feature of the vorticity profile. At around this point the amplitude of the wave, which had been growing, begins to decrease again. This pattern of behaviour is not dissimilar to that presented by Finn [22] for the situation of a hybrid between a Rayleigh-Taylor instability and a shear instability at moderate viscosity.

This mechanism then repeats itself, essentially giving a self-perpetuating cycle that sees the amplitude of the wave oscillate as counter rotating vortices are induced, which in turn cause the wave to continue oscillating. For instance at the time shown in figure 4.2(b), the spike of negative vorticity at $(x, y) = (0, 0)$ induces clockwise rotation in the flow, whilst the positive spike at $(x, y) = (\pi, 0)$ is associated with anti-clockwise rotation. The effect of this on the wave is that the height at the point $x = \pi/2$ decreases, effectively being pushed down from either side by the vortices. Likewise, at the point $x = 3\pi/2$ the wave is pushed up by the net effect of the rotational flow. This situation is reversed at later times, for instance at the time shown in figure 4.2(h) when the direction of rotation of the two central vortices is opposite to those shown in figure 4.2(b).

Changes in the density profile may similarly have an effect on the vorticity field. The main driver of this effect is the presence of the density derivative in the first-order vorticity equation (4.4.10). This is demonstrated clearly by examining the behaviour for early times. When the initial condition, namely a uniform field of $\zeta = 0$, is substituted into equation (4.4.10) it is possible to reduce the equation

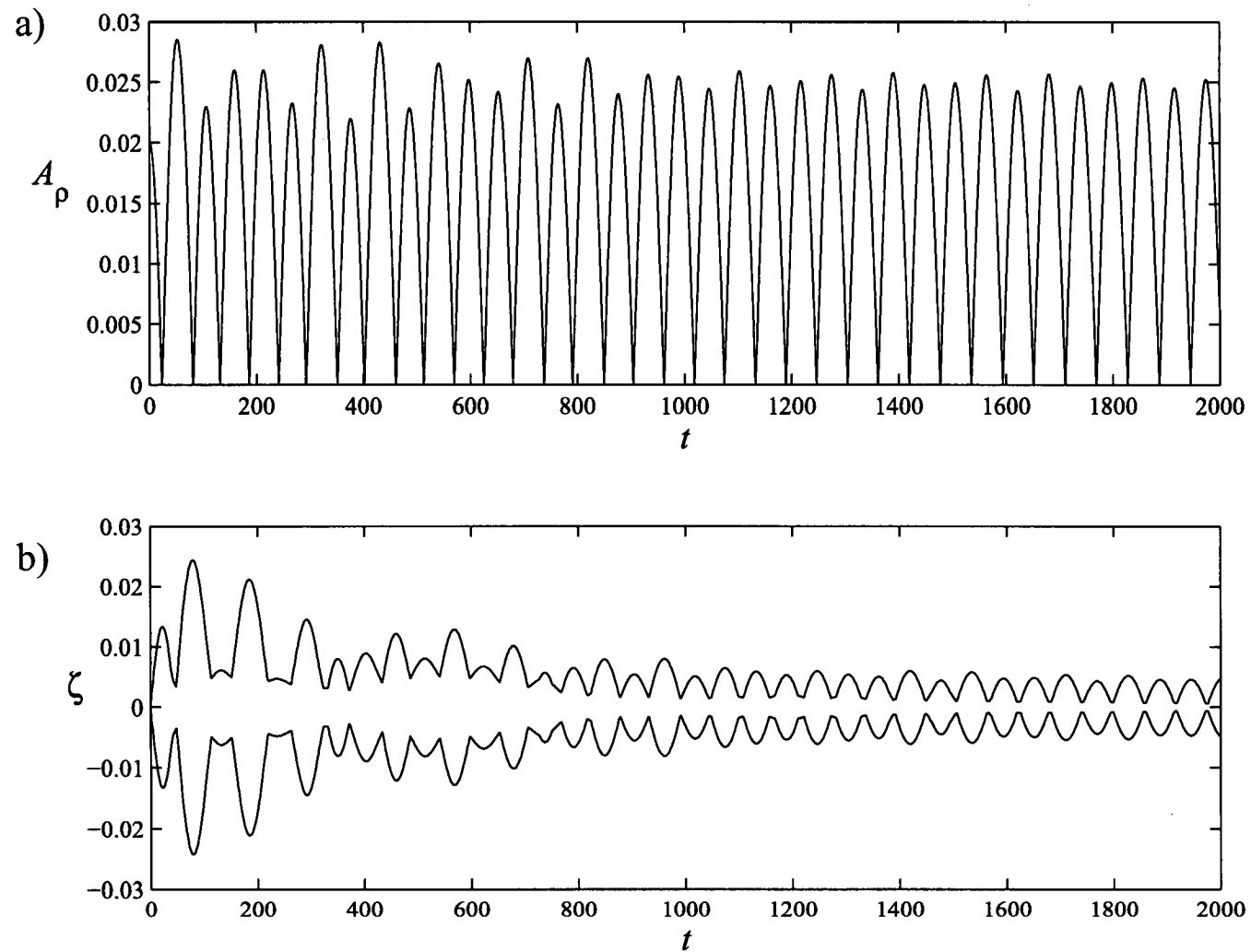


FIGURE 4.3. a) The amplitude of the interfacial wave A_p and b) the minimum and maximum of vorticity are shown for the case of $\gamma_1 = \gamma_2 = 0$ between $t = 0$ and 2000.

down to

$$\frac{\partial \Omega_1}{\partial t} = -\frac{\partial R_1}{\partial x} \quad (4.5.1)$$

for $t = 0$. Since the initial first-order part of the density profile R_1 is the difference between a perturbed and unperturbed hyperbolic tangent, as outlined in equation (4.4.46), it follows from (4.5.1) that at $t = 0$

$$\frac{\partial \Omega_1}{\partial t} = \frac{D-1}{2} \text{sech}^2(S(y - \varepsilon \sin kx)) S \cos kx.$$

This suggests that for early times vorticity is a spike in y about a sine profile, modulated by a cosine in the x direction; such a profile is seen in the vorticity contours of figure 4.2(b)-(d). For later times the development of the solution becomes more complicated as the effects of the advection terms in equations (4.4.10) and (4.4.11) begin to play a more prominent role, compounded by the diffusion of the background flow.

As a result of these effects, as well as some slight differences between the starting points of the inviscid and viscous schemes, the inviscid standing wave behaviour is not perfectly replicated in the viscous flow. The frequency of oscillation is slightly longer than in the inviscid case with $t_{cycle} \approx 110$ for the first few oscillations of the viscous solution. While the linear standing waves of the inviscid solution never grow larger than their initial amplitude, here the maximum height the wave attains over each oscillation varies markedly for early times. This maximum height eventually settles down at a value of approximately $\mathcal{A}_p \approx 0.25$, slightly larger than the amplitude of the initial wave.

The broad pattern established by this first case, where a relative maximum in the wave amplitude coincides with a drop in the magnitude of the minimum and maximum values of vorticity, is also seen in the subsequent cases. It is instructive, at least for this case where the wave does not travel, to consider the values of vorticity at the points $(x, y) = (0, 0)$ and $(\pi, 0)$. These are shown in figure 4.4, with the corresponding wave amplitude in figure 4.3(a). Here the relationship between

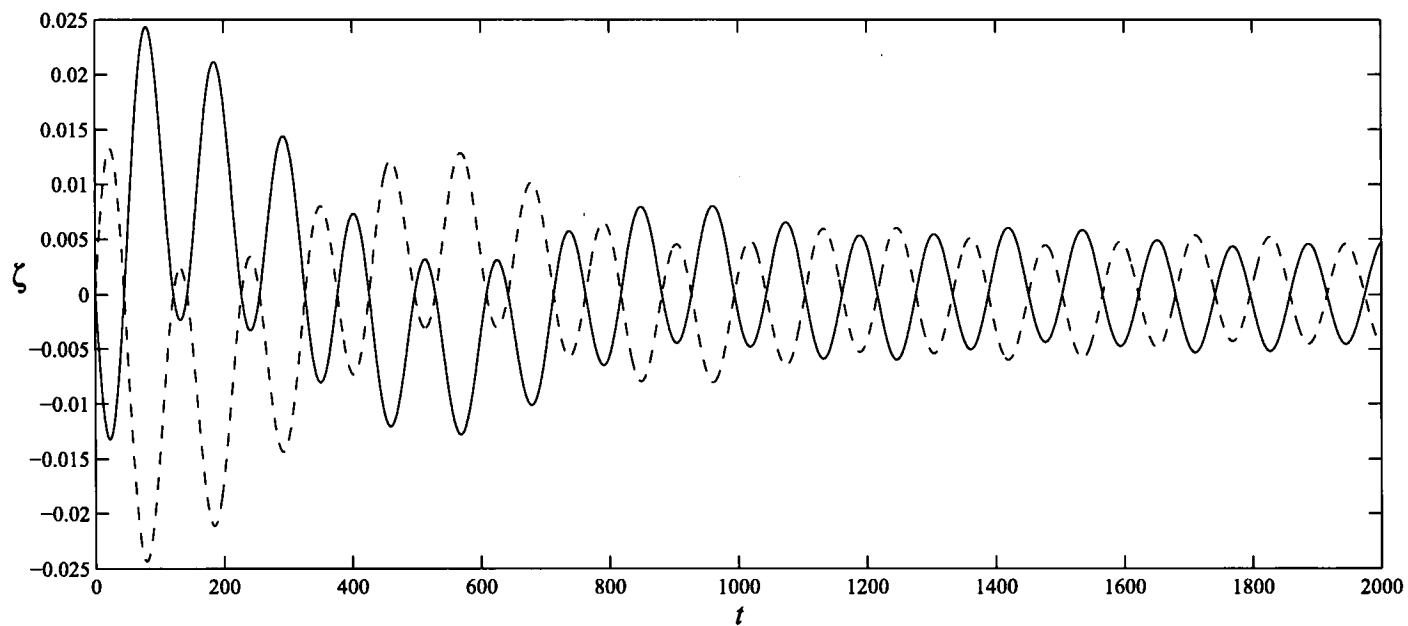


FIGURE 4.4. The values of vorticity for the case of $\gamma_1 = \gamma_2 = 0$ at the points $(x, y) = (0, 0)$ (solid line) and $(x, y) = (0, \pi)$ (dashed line).

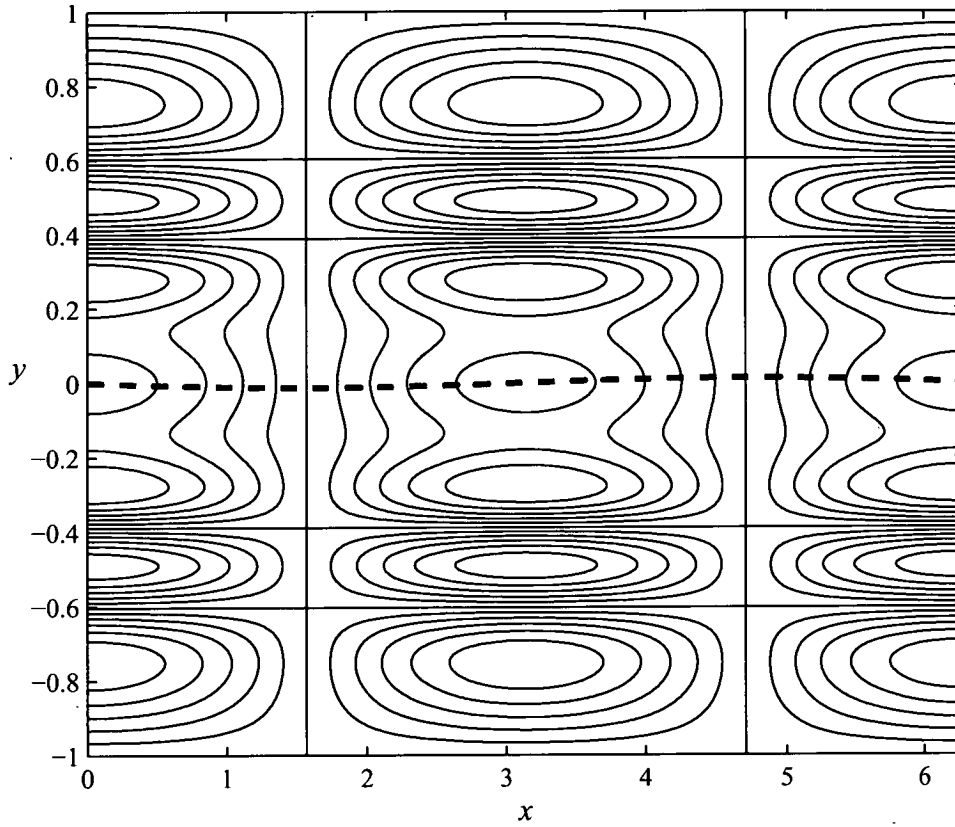


FIGURE 4.5. Contours of vorticity against a single contour of density at $t = 1972.3$ for the case of $\gamma_1 = \gamma_2 = 0$.

the wave amplitude and the value of vorticity at the fixed zero points of the wave is demonstrated more clearly than in figure 4.3(b). An interesting feature that this reveals is that the vorticity at $(x, y) = (0, 0)$ attains a larger (absolute) value when it takes a positive value, even though it is initially negative, and vice versa for the point at $(x, y) = (\pi, 0)$. A comparison of this type is more problematic for later cases where these points of minimum and maximum vorticity are not fixed in space.

The effect of diffusion on the solution for vorticity means that at later times the vorticity differs from the background flow not only in the interfacial region, but further out as well. At later times the computed solutions for this case, for instance, show a series of alternating small amplitude vortices. An example for

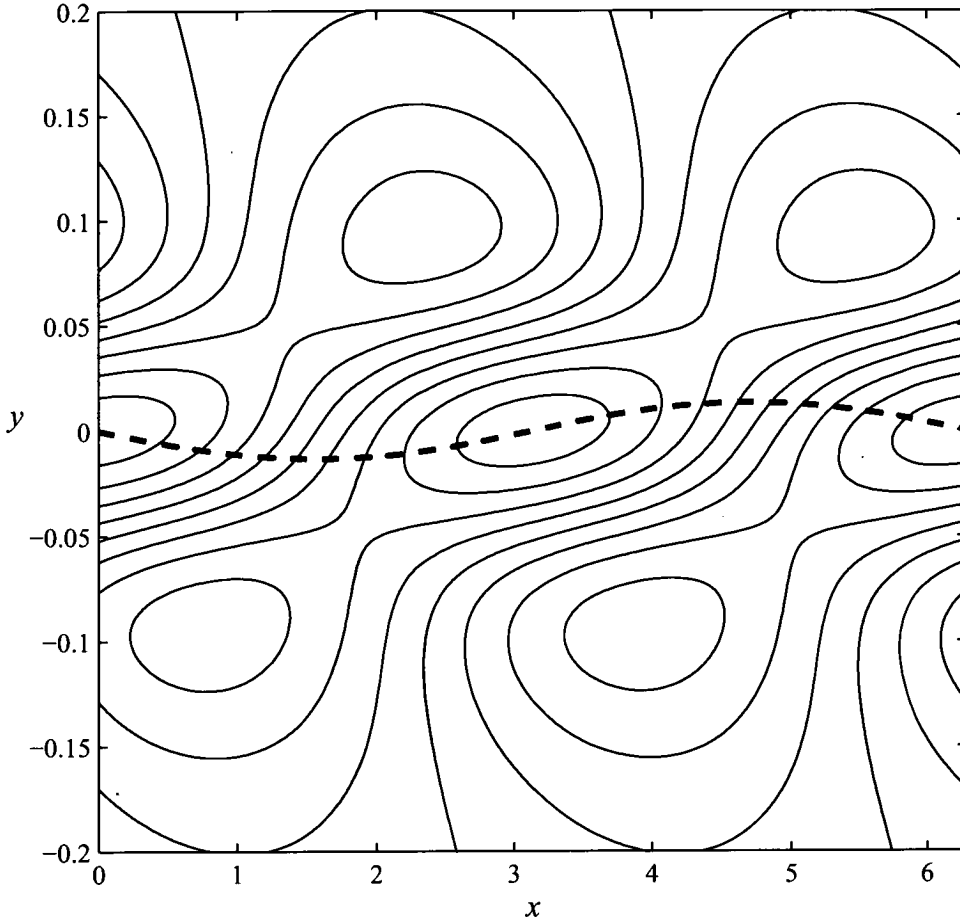


FIGURE 4.6. Contours of vorticity against a single contour of density at $t = 50.2$ for the case of $\gamma_1 = \gamma_2 = 0.1$.

$t = 1972.3$ is shown in figure 4.5. These extra outer vortices are residual remnants from earlier times that are in the process of diffusing away and their effect on the interfacial region is negligible since their amplitude is small. Note that shortly after the time shown in figure 4.5, the vorticity profile is again dominated by a pair of larger amplitude central vortices.

In discussing the remaining cases it may be taken as read that the basic mechanism that maintains the oscillatory behavior in the case of $\gamma_1 = \gamma_2 = 0$ also does so

in these subsequent cases. A key difference between the case detailed above and the cases of non-zero shear is that the wave may travel slightly as the solution evolves. The secondary vortices may similarly travel and will typically do so in accordance with the background velocity field (that is the shear profile). An example of these travelling secondary vortices may be seen in figure 4.6, where the contours of vorticity and the single contour of density are shown for the case of $\gamma_1 = \gamma_2 = 0.1$ at the moderate time of $t = 50.2$.

Figures 4.7 and 4.8 show the values for \mathcal{A}_ρ , ζ_{min} and ζ_{max} for the six cases of $\gamma_1 = \gamma_2 = 0.1, \dots, 0.6$ for times between $t = 0$ and 500. Note that for each of these cases the values for ζ_{min} and ζ_{max} emerge from the same initial value, as would be expected and, as in the previous case, there is degree of symmetry to these values although here they are reflected about the choice of background shear value, rather than zero. The behaviour at moderate times is of interest here. In particular for the first two cases, namely $\gamma_1 = \gamma_2 = 0.1$ and 0.2 we see a similar situation to the case of a stationary fluid. The behaviour of the flow is such that the initial interfacial wave oscillates and, as before, the points of inflection in the wave height coincide with relative minima in the strength of the vorticity. The frequency of oscillation becomes shorter as the strength of the shear layer is increased. Note that for $\gamma_1 = \gamma_2 = 0.1$ we see four and half cycles between $t = 0$ and 500, but for $\gamma_1 = \gamma_2 = 0.2$ there are five and a quarter oscillations in the same time span. For the case of $\gamma_1 = \gamma_2 = 0.2$ the maximum height the interfacial wave attains for successive oscillations decreases slowly through time.

The damped behaviour seen in the case of $\gamma_1 = \gamma_2 = 0.2$ becomes more pronounced as the shear layer strength is increased. In the remaining cases of $\gamma_1 = \gamma_2 = 0.3, 0.4, 0.5$ and 0.6, the wave is still oscillatory, but is increasingly heavily damped. For the case of $\gamma_1 = \gamma_2 = 0.3$ the damping is quite gradual and at $t = 500$ there is still a wave of a distinct size. In contrast, for the case of $\gamma_1 = \gamma_2 = 0.6$ the wave amplitude becomes negligible after about two oscillations.

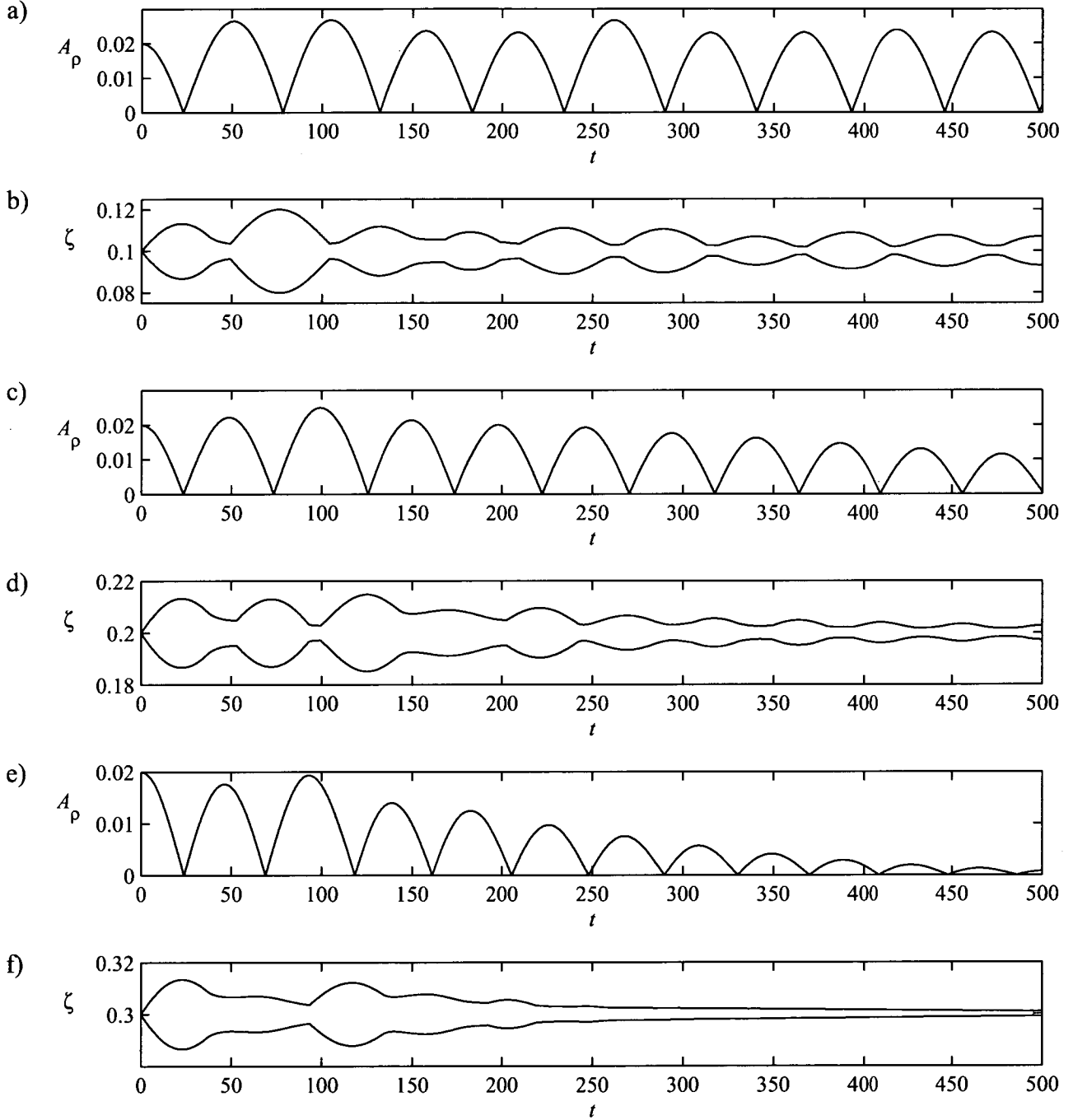


FIGURE 4.7. Figures 7(a) and (b) show the wave amplitude and the minimum/maximum of vorticity for $\gamma_1 = \gamma_2 = 0.1$. Similarly, figures 7(c) and (d) show these variables for the case of $\gamma_1 = \gamma_2 = 0.2$ and figures 7(e) and (f) are for $\gamma_1 = \gamma_2 = 0.3$.

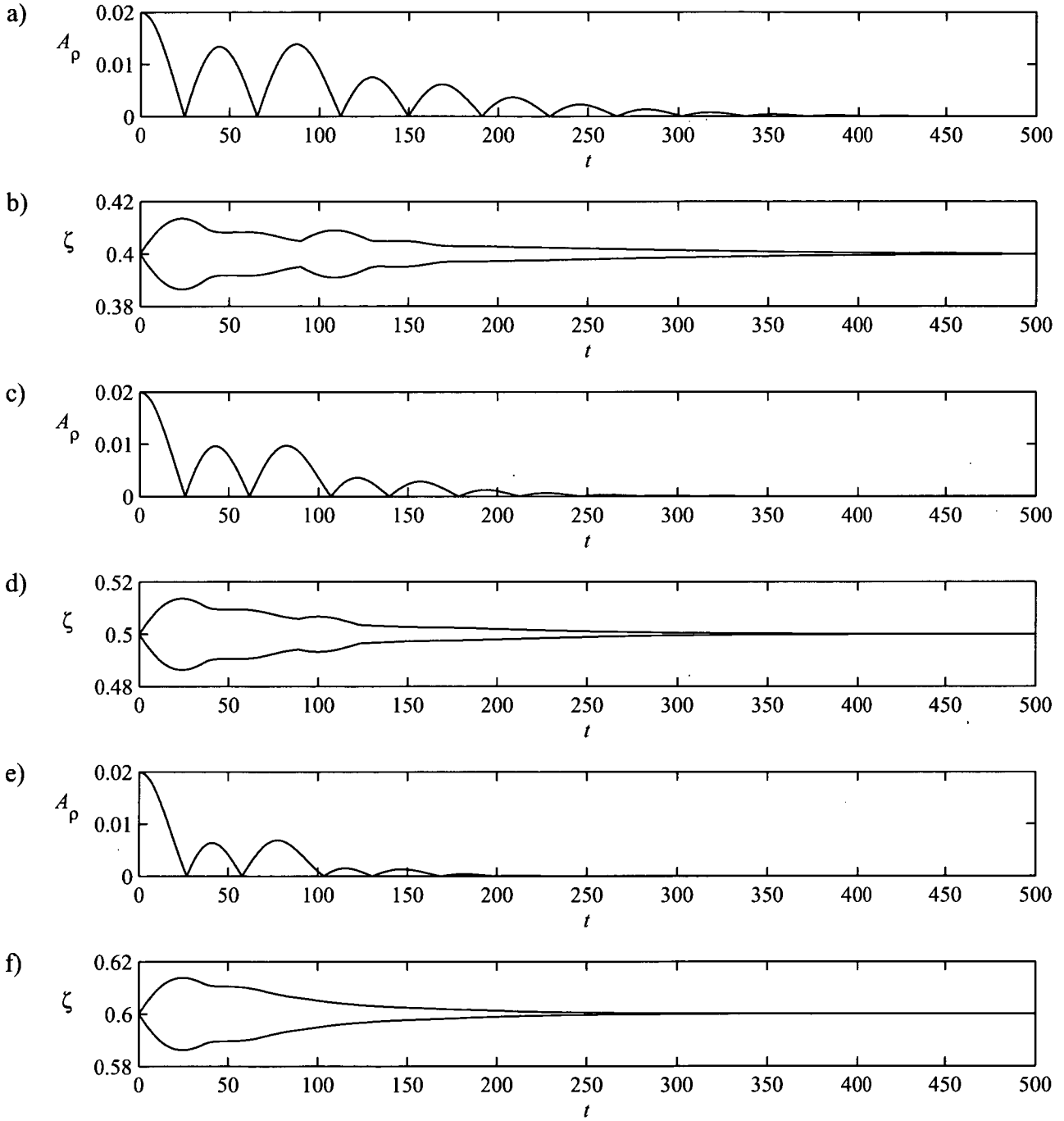


FIGURE 4.8. Figures 8(a) and (b) show the wave amplitude and the minimum/maximum of vorticity for $\gamma_1 = \gamma_2 = 0.4$. Similarly, figures 8(c) and (d) show these variables for the case of $\gamma_1 = \gamma_2 = 0.5$ and figures 8(e) and (f) are for $\gamma_1 = \gamma_2 = 0.6$.

The key difference between the damped and undamped cases is in the role of the advection terms in the governing equations (4.4.10) and (4.4.11). In particular, as the shear layer strength is increased the horizontal base speed $U_{01}(y)$ becomes quite large in the neighbourhood of the interfacial region, meaning that the terms $U_0 \frac{\partial \Omega_1}{\partial x}$ in equation (4.4.10) and $U_0 \frac{\partial R_1}{\partial x}$ in equation (4.4.11) play a more dominant role. So strong does this effect become for the larger values of shear layer strength that the oscillatory pattern is barely able to become established before being overwhelmed by the presence of the strong shear. The net result is that for a strong shear flow such as the case $\gamma_1 = \gamma_2 = 0.6$ an initial disturbance in the density will quickly be subsumed into the background flow profile.

As the strength of the shear layer is increased far beyond this point the oscillatory behaviour no longer occurs at all. The values of \mathcal{A}_ρ , ζ_{min} and ζ_{max} for the extreme case of $\gamma_1 = \gamma_2 = 20$ are shown in figure 4.9. Here the amplitude of the wave decreases to zero rapidly without any oscillation and by the last time shown the amplitude has decreased to less than 10^{-9} . The maximum and minimum of vorticity behave in a similar fashion to the previous damped cases; the minimum and maximum values are symmetrical about $\zeta = 20$ and increase for a short time before decreasing sharply.

4.5.2. Zero shear in one layer ($\gamma_1 = 0$, $\gamma_2 \neq 0$). The case where no background shear is present in the top layer is now considered. Keeping the value of γ_1 fixed at zero, the lower layer shear parameter γ_2 is varied over a range of small values. As mentioned earlier, the permitted difference between the two shear parameters is limited to being small so that unwanted spikes in the initial vorticity profile are not introduced. Throughout this section the density ratio, steepness parameter and perturbation size will remain the same as in section 4.5.1.

The wave amplitude and the minimum and maximum values of vorticity for the first two choices of γ_2 , that is $\gamma_2 = 0.01$ and $\gamma_2 = 0.02$, are shown in figure 4.10. Both these solutions display a different of kind oscillatory behaviour than the standing wave-like solutions seen so far. There is an overall slow decrease in

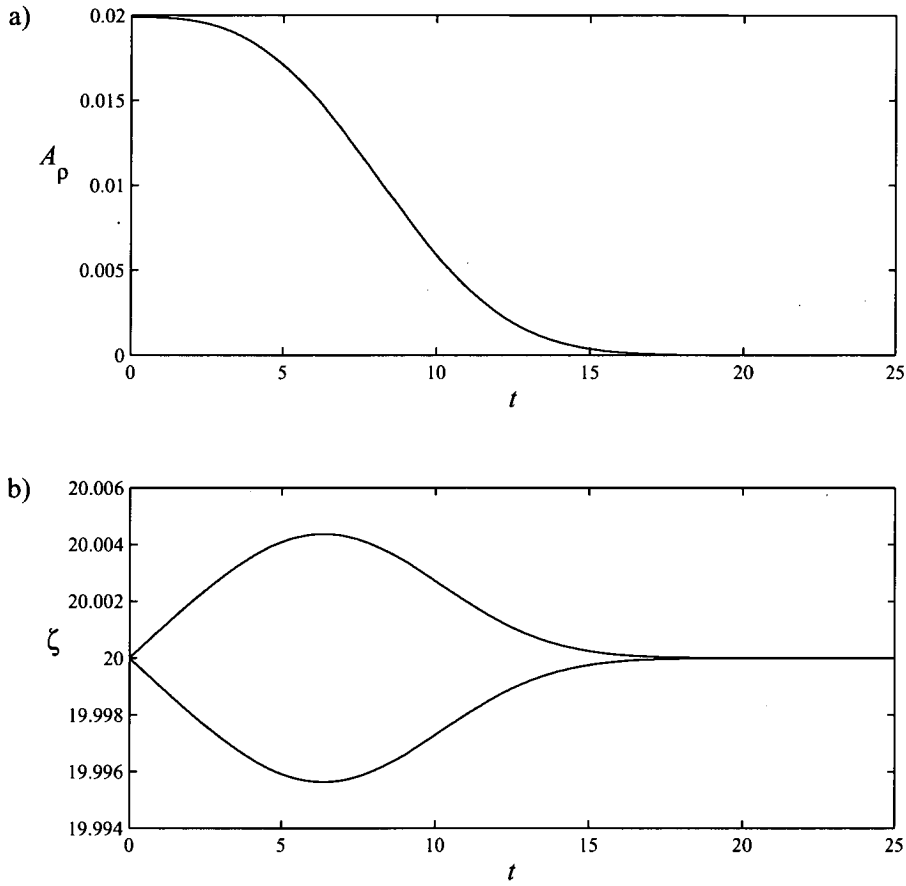


FIGURE 4.9. For the case of $\gamma_1 = \gamma_2 = 20$ between $t = 0$ and 25 a) the amplitude of the interfacial wave A_p and b) the minimum and maximum of vorticity.

the amplitude of the wave and the damped oscillations occur on top of this. The mechanism by which the oscillations are maintained is similar to that outlined in section 4.5.1. For early times the oscillations are in the order of the wave's amplitude but become heavily damped as the solution progresses. For example in the case of $\gamma_2 = 0.02$, by the last computed times the wave is decreasing in amplitude free of any oscillations. Similarly, both the minimum and maximum in vorticity exhibit oscillatory behaviour for early times, but by $t = 1000$ for the cases shown here the

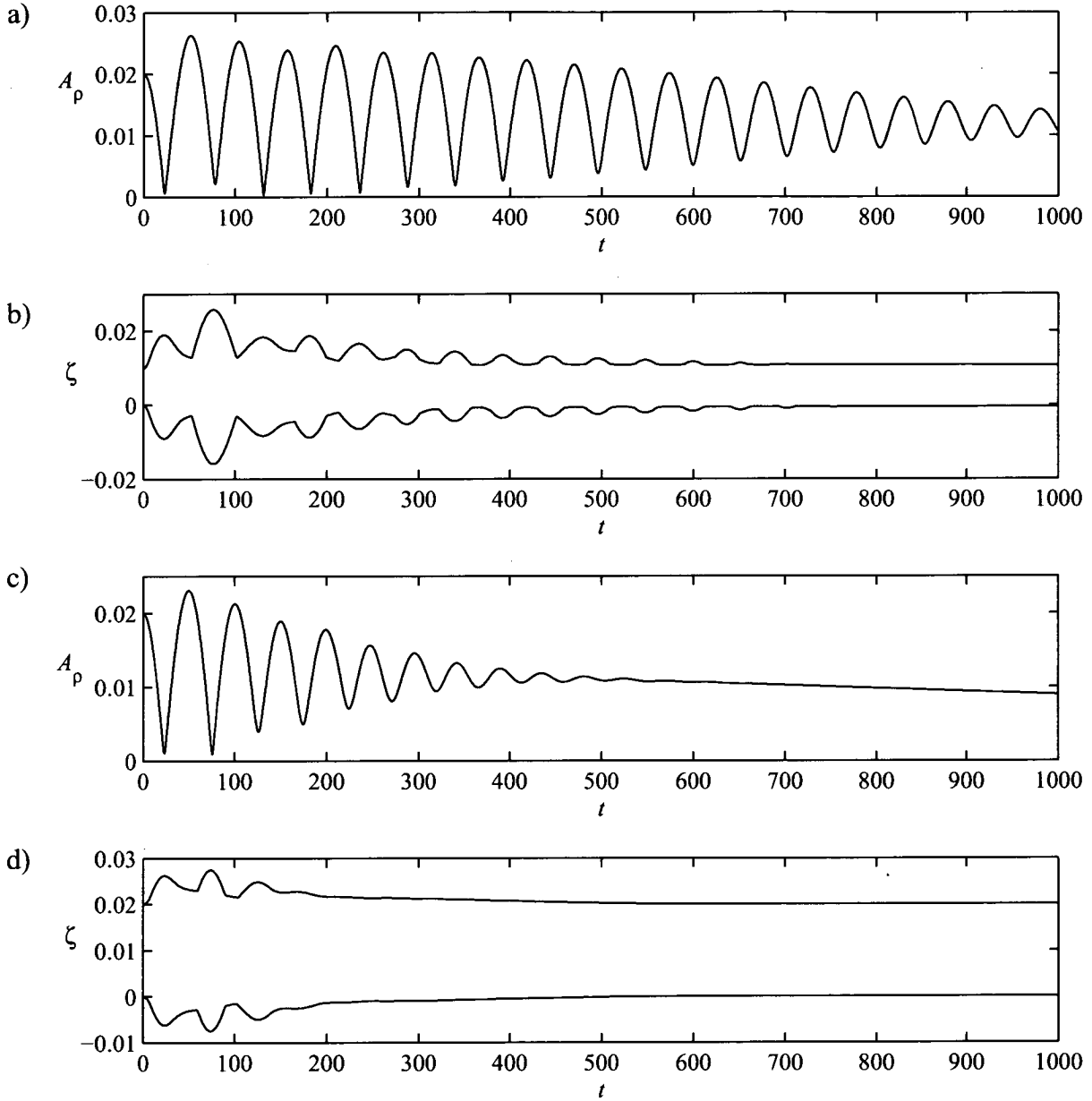


FIGURE 4.10. Figures 10(a) and (b) show the wave amplitude and the minimum/maximum of vorticity for $\gamma_1 = 0$ and $\gamma_2 = 0.01$. Similarly, figures 10(c) and (d) show these variables for the case of $\gamma_1 = 0$ and $\gamma_2 = 0.02$.

values for the maximum and minimum of vorticity have settled down to $\zeta_{max} \approx \gamma_2$ and $\zeta_{min} \approx 0$, respectively. It is likely that some oscillatory behaviour in vorticity is masked in these plots, where this variation involves values between these minimum and maximum values. An example of this may be seen for the case of $\gamma_2 = 0.01$ where at later times the wave amplitude is clearly oscillating, but the minimum and maximum of vorticity are constant.

As predicted by the linearized inviscid solution, these waves travel as they evolve. The solution for $\gamma_2 = 0.02$, for instance, is a travelling wave of decreasing amplitude for times after $t \approx 600$. Since steady solutions have been computed for similar flow configurations, see for instance Pullin and Grimshaw [48], it is possible that the decrease in amplitude seen here is due, at least in part, to the gradual diffusion of the sharp interfacial region. If this diffusion were not present it is possible that the wave would converge to a steady solution after the oscillatory behaviour had damped away.

Similar to the case of constant shear, if the value of γ_2 is increased much beyond this point the behaviour of the solutions becomes more heavily damped. Three further values of γ_2 are chosen, $\gamma_2 = 0.03, 0.04$ and 0.05 , and the wave amplitude and vorticity values for these cases are summarised in figure 4.11. All three cases feature an oscillatory component that quickly damps away leaving a wave that gradually decreases in height. This is similar to the behaviour of the first two cases in this section, although here the oscillatory behaviour is barely established before it damps away. The amplitude of the oscillations for these cases is small compared to size of the wave and the minimum and maximum values of vorticity do not vary much. As with the solution for $\gamma_2 = 0.01$ and 0.02 , the maximum and minimum values of vorticity are rather uninformative as the oscillatory component in the vorticity is greater than zero but less than the choice for γ_2 .

4.5.3. Comparison with finite difference methods. To compare the accuracy of the linearized perturbation approach against a fully non-linear finite difference approach a test case will be examined. The case of $\gamma_1 = \gamma_2 = 0$ will be run

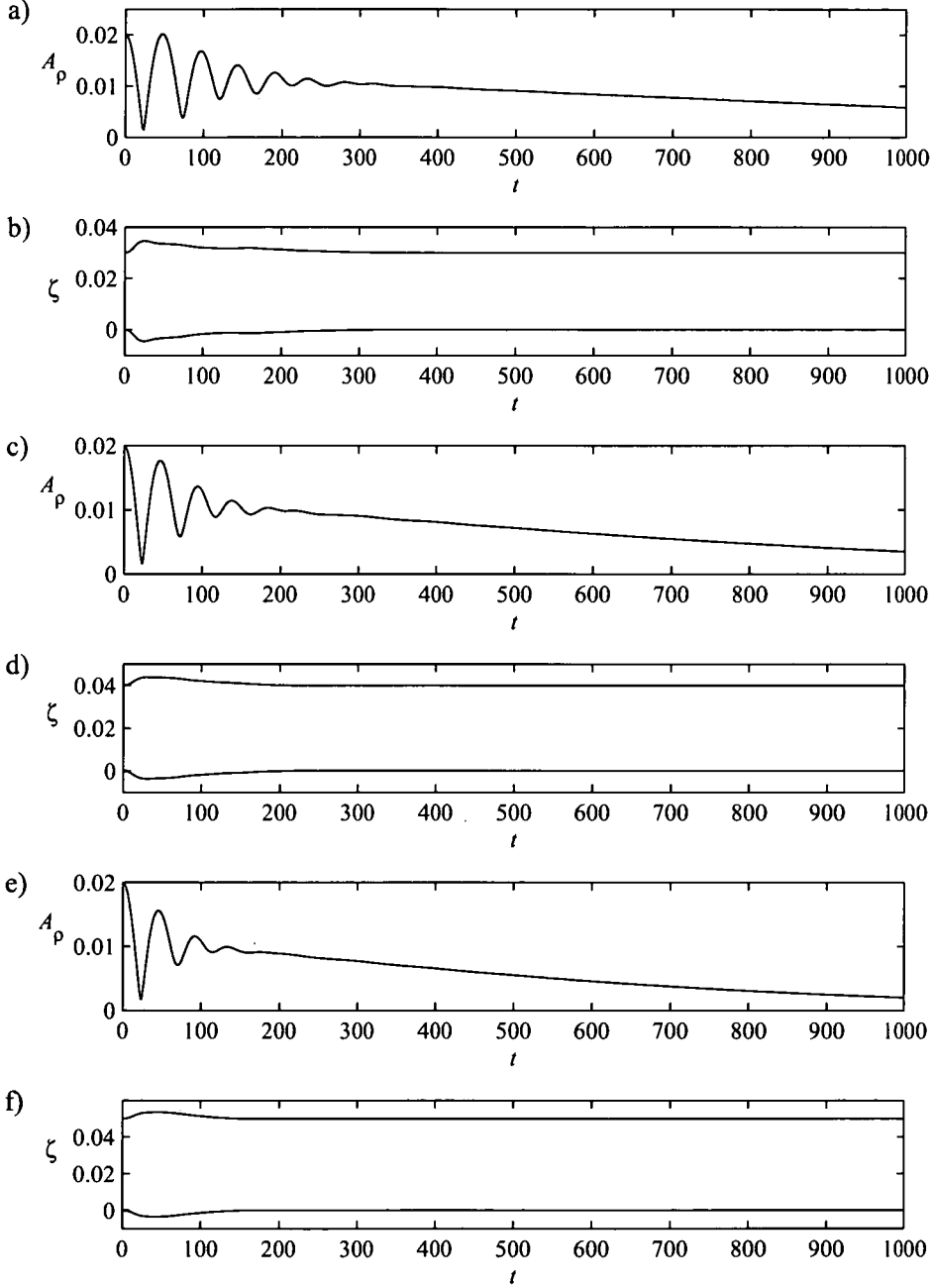


FIGURE 4.11. Figures 11(a) and (b) show the wave amplitude and the minimum/maximum of vorticity for $\gamma_1 = 0$ and $\gamma_2 = 0.03$. Similarly, figures 11(c) and (d) show these variables for the case of $\gamma_1 = 0$ and $\gamma_2 = 0.04$. and figures 11(e) and (f) are for $\gamma_1 = 0$ and $\gamma_2 = 0.05$.

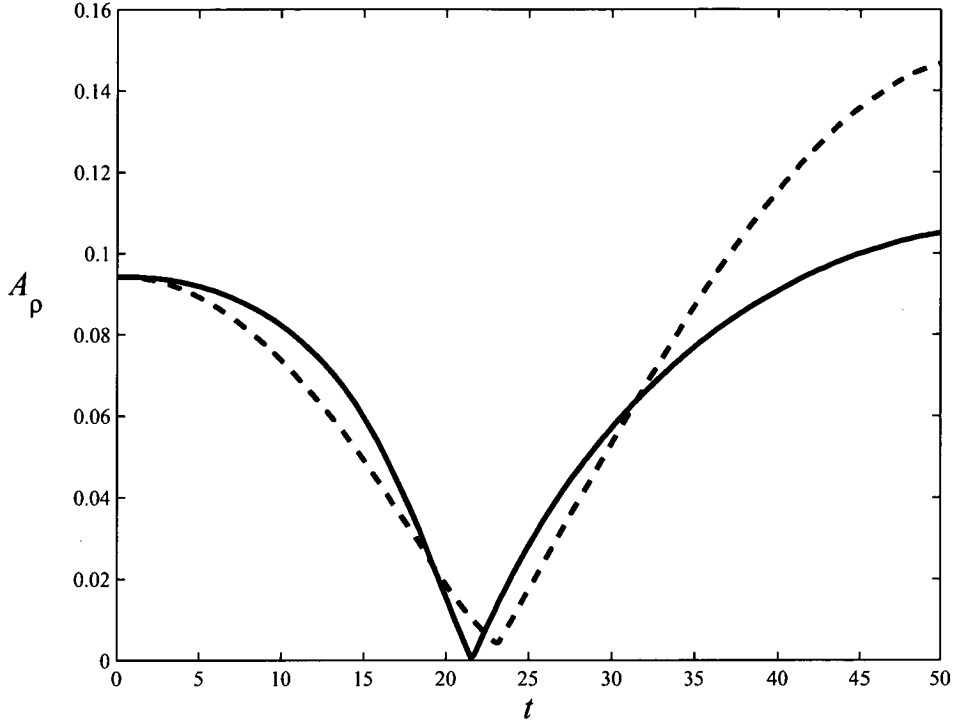


FIGURE 4.12. Comparison of wave amplitude for the case of $\gamma_1 = \gamma_2 = 0$ computed with the perturbation series technique (solid line) and a finite difference method (dashed line).

using two different methods, namely the first-order perturbation series method and an efficient finite difference scheme. A larger perturbation of $\varepsilon = 0.05$ is used here so that the grid scale of the finite difference method need not be too fine. The finite difference scheme is an alternating direction implicit (ADI) technique that solves the full version of the governing equations (4.2.3)–(4.2.5) using Peaceman-Rachford methods. Full details of this scheme will not be included here for reasons of space, but it is fully outlined in chapter 3 where it was used to model the Kelvin-Helmholtz instability. This method is implemented over an evenly spaced grid with 200 points in the x -direction and 400 points in the y -direction.

The wave amplitude from $t = 0$ to $t = 50$ as computed by both methods is shown in figure 4.12. Within this time period both solutions pass through about

half an oscillation, although the period of the ADI solution is slightly longer. Even for early times the two amplitudes do not match precisely and by the end of the time interval have diverged significantly. It is notable that while the amplitude of the perturbation series solution approaches zero at its minimum, the corresponding point in the finite difference scheme is much further from zero as a consequence of the choice of grid size. The differences between the solutions for moderate times may be due to the extra non-linearity that is included in the ADI scheme, particularly the fully non-linear advection terms of the governing equations (4.2.4) and (4.2.5). Additionally, since the size of the initial wave is larger than is ideal under the assumptions of the perturbation series scheme small inaccuracies may have been introduced. The resulting differences between the two schemes are indicative of the limitations of this method and the ADI solution is expected to be more representative of the true solution where a initial wave of this size is used.

4.6. Conclusion

A two-layer shear flow has been studied for both viscous and inviscid fluids. The predictions from the inviscid version of the problem in section 4.3, that standing waves are permitted and that these may travel, were found to hold true when compared with solutions computed by the perturbation series approximation to the viscous problem of section 4.4. In the main, the inviscid version tended to underestimate the frequency of oscillation seen in the viscous solutions. Additionally, the effect of the inclusion of viscosity, a diffuse interface and the extra non-linearity in the viscous scheme meant that the behaviour of those solutions, although still containing an oscillatory component, was more complicated than the standing waves predicted for the inviscid flow.

Several different types of oscillatory behaviours were obtained from the viscous perturbation series scheme. For a layer of constant shear the solutions were essentially standing waves. As the shear layer strength was increased these became more and more heavily damped. The interaction between vorticity and density,

in particular the way that this perpetuates the oscillatory behaviour, was outlined in detail in section 4.5.1 and this mechanism also features in the more complex solutions of section 4.5.2 where no shear is present in the upper layer. Although there is an oscillatory component to those solutions it is typically damped and for later times the behaviour is dominated by a wave whose amplitude decreases. As with the case of a layer of constant shear, the damping of the oscillatory part of these solutions becomes heavier as the shear layer strength is increased.

The main advantage to using the perturbation series technique is in speed of computation. It is undoubtedly more efficient than using a method based on full double Fourier series or a finite difference technique, but also has certain restrictions that those methods do not. In particular, the choice of keeping the Fourier series monochromatic in x limits the possible initial conditions and the scope for the flow to evolve in certain ways. As such, this technique is only suitable for certain linearized problems where the flow in question is able to be captured accurately by the chosen representation. Nevertheless, a comparison of the linearized viscous solutions of this chapter with the fully non-linear results obtained with an ADI finite-difference scheme give some confidence that the overall features reported here are broadly representative of the true situation.

CHAPTER 5

Conclusion

Three interfacial wave problems were considered in this thesis. Appropriate solution techniques have been selected and implemented for each of these fluid flows. These techniques were all developed with a view to maximising the efficiency and accuracy with which the respective interfacial waves could be computed. Where an inviscid flow was considered this involved following the evolution of an infinitely thin interface between incompressible fluids, and for viscous fluids these genuine interfaces were replaced in compressible flow with interfacial regions of finite width.

The inviscid 3-layer intrusion flow investigated in chapter 2 exhibited a wide variety of steady non-linear interfacial waves. These steady waves were calculated to a high degree of accuracy using a spectral method based on Fourier series. The computed solutions included waves that showed superharmonic resonances and limiting waves. A particularly interesting feature of the resonant waves was the existence of multiple resonances where, as in the case shown in figure 2.6, a wave would display successive resonances as its amplitude was increased.

In chapter 3 the steady spectral method used for the intrusion flow was extended to treat the time-dependent inviscid Kelvin-Helmholtz instability. This chapter also introduced a vorticity-streamfunction formulation to investigate the viscous version of this problem and both approaches successfully reproduced some well-known features of the Kelvin-Helmholtz instability. For both inviscid and viscous flow a small perturbation to the interface grew exponentially from a small sinusoid to become a moderate amplitude non-linear wave. In the inviscid case a curvature singularity formed at around this point preventing the wave from evolving further. The viscous flow was not impeded by a curvature singularity and the interface

continues in its evolution to the point that it turns over and eventually forms a 'cat's eye'-type spiral.

A different approach to modelling a viscous flow was adopted in chapter 4 where a two-layer shear flow was investigated using perturbation series techniques. A linearized analysis of the associated inviscid problem indicated that a small disturbance would result in standing waves at the interface. This allowed the assumption to be made that the corresponding interfacial wave in viscous flow would not grow much larger than its initial size, which suggests that a perturbation series analysis of the viscous governing equations is appropriate. Care was taken to specify a representation of the solution and an initial condition for the viscous problem that would closely match the inviscid version of the problem. Standing waves were found to exist in viscous flow and a number of other oscillatory behaviours were also seen at the interface.

There is much scope for future work on these types of fluid flow problems. The methods presented here are quite adaptable and may potentially be applied to a wide array of flows. A logical next step would be to study the Holmboe instability, a situation quite similar to the 3-layer flow of chapter 2 as well as the Kelvin-Helmholtz instability. Such a study might involve adapting the techniques of chapter 3 to the Holmboe problem. A straightforward extension of the material in chapter 4 may involve further comparisons between the perturbation series technique and the fully non-linear ADI method where a smaller perturbation amplitude than that used in section 4.5.3 might see better agreement between the two techniques. Additionally, the techniques used to model shear flows in this thesis are applicable to flows that do not contain shear. Some possible situations where they may be applied are in the Rayleigh-Benard problem (where a stratified fluid is heated from below) and on viscous shaking in a tank (where resonance effects are possible).

Bibliography

- [1] M. Abramowitz and I. A. Stegun. *Handbook of Mathematical Functions*. National Bureau of Standards, 1970.
- [2] T.R. Akylas and R.H.J. Grimshaw. Solitary internal waves with oscillatory tails. *Journal of Fluid Mechanics*, 242:279–298, 1992.
- [3] J.D. Anderson. *Computational Fluid Dynamics*. McGraw-Hill, 1995.
- [4] L. Armi and D.M. Farmer. Maximal two-layer exchange through a contraction with barotropic flow. *Journal of Fluid Mechanics*, 164:27–51, 1986.
- [5] K.E. Atkinson. *An introduction to numerical analysis*. J. Wiley & Sons, 1978.
- [6] G.R. Baker and M.J. Shelley. On the connection between thin vortex layers and vortex sheets. *Journal of Fluid Mechanics*, 215:161–194, 1990.
- [7] C.M. Bender and S.A. Orszag. *Advanced Mathematical Methods for Scientists and Engineers: Asymptotic Methods and Perturbation Theory*. Springer, 1999.
- [8] G. Birkhoff. Helmholtz and Taylor instability. *Proceedings of the Symposium on Applied Mathematics*, 13:55–76, 1962.
- [9] J. Candela. Mediterranean Water and Global Circulation. In G. Siedler, J. Church, and J. Gould, editors, *Ocean Circulation and Climate*, pages 419–429. Academic Press, 2001.
- [10] K.M. Case. Stability of inviscid plane Couette flow. *Physics of Fluids*, 3(2):143–148, 1960.
- [11] S. Chandrasekhar. *Hydrodynamic and Hydromagnetic Stability*. Dover, 1961.
- [12] B. Chen and P.G. Saffman. Steady Gravity-Capillary Waves on Deep Water - II. Numerical Results for Finite Amplitude. *Studies in Appl. Maths*, 62:95–111, 1980.

- [13] M.J. Chen and L.K. Forbes. A study of nonlinear waves and resonance in intrusion flows. *Proceedings of the 8th Biennial Engineering Mathematics and Applications Conference, EMAC*, 49:C51–C68, 2007.
- [14] M.J. Chen and L.K. Forbes. Steady periodic waves in a three-layer fluid with shear in the middle layer. *Journal of Fluid Mechanics*, 594:157–181, 2008.
- [15] M.J. Chen and L.K. Forbes. Accurate methods for computing inviscid and viscous Kelvin-Helmholtz instability. *Journal of Computational Physics*, submitted, 2010.
- [16] M.J. Chen and L.K. Forbes. Waves in two-layer shear flow for viscous and inviscid fluids. *European Journal of Mechanics - B/Fluids*, submitted, 2010.
- [17] S.J. Cowley, G.R. Baker, and S. Tanveer. On the formation of Moore curvature singularities in vortex sheets. *Journal of Fluid Mechanics*, 378:233–267, 1999.
- [18] W.O. Criminale and P.G. Drazin. The evolution of linearized perturbations of parallel flows. *Studies in Applied Mathematics*, 157:123–157, 1990.
- [19] P.G. Drazin and W.H. Reid. *Hydrodynamic Stability*. Cambridge University Press, 1981.
- [20] M. Ehrnstrom and E. Wahlen. On the fluid motion in standing waves. *Journal of Nonlinear Mathematical Physics*, 15:74–86, 2008.
- [21] D.E. Farrow and G.C. Hocking. A numerical model for withdrawal from a two-layer fluid. *Journal of Fluid Mechanics*, 549:141–157, 2006.
- [22] J.M. Finn. Nonlinear interaction of Rayleigh-Taylor and shear instabilities. *Physics of Fluids*, 5 (2):415–432, 1990.
- [23] M.R. Flynn and B.R. Sutherland. Intrusive gravity currents and internal gravity wave generation in stratified fluid. *Journal of Fluid Mechanics*, 514:355–383, 2004.
- [24] L.K. Forbes. The Rayleigh-Taylor instability for inviscid and viscous fluids. *Journal of Engineering Mathematics*, 65:273–290, 2009.
- [25] L.K. Forbes, M.J. Chen, and C.E. Trenham. Computing unstable periodic waves at the interface of two inviscid fluids in uniform vertical flow. *Journal*

- of Computational Physics*, 221:269–287, 2007.
- [26] L.K. Forbes and G.C. Hocking. An intrusion layer in stationary incompressible fluids: Part 2: Solitary waves. *European Journal of Applied Mathematics*, 17:577–595, 2006.
 - [27] L.K. Forbes, G.C. Hocking, and D.E. Farrow. An intrusion layer in stationary incompressible fluids: Part 1: Periodic waves. *European Journal of Applied Mathematics*, 17:557–575, 2006.
 - [28] D. Fructus and J. Grue. Fully nonlinear solitary waves in a layered stratified fluid. *Journal of Fluid Mechanics*, 505:323–347, 2004.
 - [29] T. Funada and D.D. Joseph. Viscous potential flow analysis of Kelvin-Helmholtz instability in a channel. *Journal of Fluid Mechanics*, 445:263–283, 2001.
 - [30] H. Helmholtz. Ueber discontinuirliche fluissigkeitsbewegungen. *Philosophical Magazine*, 36:337–346, 1868.
 - [31] T.Y. Hou, J.S. Lowengrub, and M.J. Shelley. The long-time motion of vortex sheets with surface tension. *Physics of Fluids*, 9(7):1933–1954, July 1997.
 - [32] Lord Kelvin. *Mathematical and Physical Papers*. Cambridge University Press, 1910.
 - [33] R. Krasny. Desingularization of periodic vortex sheet roll-up. *Journal of Computational Physics*, 65:292–313, 1986.
 - [34] E. Kreyszig. *Advanced Engineering Mathematics*. John Wiley & Sons, 1999.
 - [35] H. Lamb. *Hydrodynamics*. Dover, 1932.
 - [36] J.E. Lewis, B.M. Lake, and D.R.S. Ko. On the interaction of internal waves and surface gravity waves. *Journal of Fluid Mechanics*, 63:773–800, 1974.
 - [37] M.S. Longuet-Higgins and E.D. Cokelet. The Deformation of Steep Surface Waves on Water. I. A Numerical Method of Computation. *Proceedings of the Royal Society of London. Series A, Mathematical and Physical Sciences*, 350(1660):1–26, 1976.

- [38] A. Mastrano and A. Melatos. Kelvin-Helmholtz instability and circulation transfer at an isotropic-anisotropic superfluid interface in a neutron star. *Monthly Notices of the Royal Astronomical Society*, 361(3):927–941, 2005.
- [39] A.P. Mehta, B.R. Sutherland, and P.J. Kyba. Interfacial gravity currents. II. Wave excitation. *Physics of Fluids*, 14:3558–3569, 2002.
- [40] D.I. Meiron and P.G. Saffman. Overhanging interfacial gravity waves of large amplitude. *Journal of Fluid Mechanics*, 120:213–218, 1983.
- [41] H. Michallet and F. Dias. Non-linear resonance between short and long waves. *Proceedings of the 9th International Offshore and Polar Engineering Conference*, pages 193–198, 1999.
- [42] D. W. Moore. The spontaneous appearance of a singularity in the shape of an evolving vortex sheet. *Proceedings of the Royal Society of London. Series A, Mathematical and Physical Sciences*, 365:105–119, 1979.
- [43] E. Părău and F. Dias. Interfacial periodic waves of permanent form with free-surface boundary conditions. *Journal of Fluid Mechanics*, 437:325–336, 2001.
- [44] D.W. Peaceman and H.H. Rachford. The numerical solution of parabolic and elliptic differential equations. *Journal of the Society for Industrial and Applied Mathematics*, 3(1):28–41, 1955.
- [45] O.M. Phillips. *The dynamics of the upper ocean*. Cambridge University Press, 1969.
- [46] O.M. Phillips. Non-linear dispersive waves. *Annual Review of Fluid Mechanics*, 6:93–108, 1974.
- [47] W.H. Press, S.A. Teukolsky, W.T. Vetterling, and B.P. Flannery. *Numerical Recipes in Fortran 77, Second Edition*. Cambridge University Press, 1992.
- [48] D.I. Pullin and R.H.J. Grimshaw. Interfacial progressive gravity waves in a two-layer shear flow. *Physics of Fluids*, 26:1731–1739, 1983.
- [49] P.-O. Rusås and J. Grue. Solitary waves and conjugate flows in a three-layer fluid. *European Journal of Mechanics, B/Fluids*, 21:185–206, 2002.

- [50] P.G. Saffman. *Vortex Dynamics*. Cambridge University Press, 1992.
- [51] P.G. Saffman and H.C. Yuen. Finite-amplitude interfacial waves in the presence of a current. *Journal of Fluid Mechanics*, 123:459–476, 1982.
- [52] M. Siegel. A study of singularity formation in the Kelvin-Helmholtz instability with surface tension. *SIAM Journal of Applied Mathematics*, 55(4):865–891, August 1995.
- [53] W.D. Smyth. Kelvin-Helmholtz billow evolution from a localized source. *Quarterly Journal of the Royal Meteorological Society B*, 130(603):2753–2788, 2004.
- [54] B.R. Sutherland, P.J. Kyba, and M.R. Flynn. Intrusive gravity currents in two-layer fluids. *Journal of Fluid Mechanics*, 514:327–353, 2004.
- [55] J.C. Tannehill, D.A. Anderson, and R.H. Pletcher. *Computational Fluid Mechanics and Heat Transfer*. Taylor & Francis, 1997.
- [56] G.I. Taylor. Effect of variation in density on the stability of superposed streams of fluid. *Proceedings of the Royal Society, A*, 82:499–523, 1931.
- [57] M.-L. E. Timmermans and L.J. Pratt. Two-layer rotating exchange flow between two deep basins: Theory and application to the Strait of Gibraltar. *Journal of Physical Oceanography*, 35:1568–1592, 2005.
- [58] G. Tryggvason, W.J.A. Dahm, and K. Sbeih. Fine structure of vortex sheet rollup by viscous and inviscid simulation. *Journal of Fluids Engineering*, 113:31–36, 1991.
- [59] J.S. Turner. *Buoyancy effects in fluids*. Cambridge University Press, 1973.
- [60] R.E.L. Turner and J.-M. Vanden-Broeck. The limiting configuration of interfacial gravity waves. *Physics of Fluids*, 29:372–375, 1986.
- [61] O.M. Umurhan and E. Heifetz. Holmboe modes revisited. *Physics of Fluids*, 19(6)(064102), 2007.
- [62] J.-M. Vanden-Broeck and R.E.L. Turner. Long periodic internal waves. *Physics of Fluids A*, 4:1929–1935, 1992.
- [63] G. von Winckel. lgwt.m, at: Matlab file exchange website, 2004.
- [64] E.L. Wachspress. *Iterative Solution of Elliptic Systems*. Prentice-Hall, 1966.

- [65] M.J.M. Williams, A. Jenkins, and J. Determann. Physical controls on ocean circulation beneath ice shelves revealed by numerical models. In S.S. Jacobs and R.F. Weiss, editors, *Ocean, ice, and atmosphere: Interactions at the Antarctic continental margin*, pages 285–299. American Geophysical Union, 1998.
- [66] J.R. Wilton. On ripples. *Philosophical Magazine*, 29:688–700, 1915.